Summer 8-17-2017

Structural Behavior of Inflatable, Reinforced, Braided, Tubular Members

Joshua Clapp
University of Maine, joshua.clapp@maine.edu

Follow this and additional works at: http://digitalcommons.library.umaine.edu/etd

Part of the Space Vehicles Commons, Structural Engineering Commons, and the Structures and Materials Commons

STRUCTURAL BEHAVIOR OF INFLATABLE, REINFORCED, BRAIDED, TUBULAR MEMBERS

By

Joshua David Clapp

B.S. University of Maine, 2005

M.S. University of Maine, 2007

A DISSERTATION

Submitted in Partial Fulfillment of the

Requirements for the Degree of

Doctor of Philosophy

(in Civil Engineering)

The Graduate School

The University of Maine

August, 2017

Advisory Committee:

William G. Davids, Professor of Civil and Environmental Engineering and Department Chair, Advisor

Andrew J. Goupee, Assistant Professor of Mechanical Engineering

Roberto Lopez-Anido, Professor of Civil and Environmental Engineering

Eric N. Landis, Professor of Civil and Environmental Engineering

Senthil S. Vel, Professor of Mechanical Engineering

STRUCTRAL BEHAVIOR OF INFLATABLE, REINFORCED, BRAIDED, TUBULAR MEMBERS

By Joshua David Clapp, P.E.

Dissertation Advisor: Dr. William G. Davids, P.E.

An Abstract of the Dissertation Presented
in Partial Fulfillment of the Requirements for the
Degree of Doctor of Philosophy
(in Civil Engineering)

August, 2017

The Hypersonic Inflatable Aerodynamic Decelerator (HIAD) system being developed by the National Aeronautics and Space Administration (NASA) is an inflatable structure composed of multiple, concentric, pressurized tori, load straps, and a thermal protection system. The HIAD overcomes limitations inherent with the use of rigid decelerators since the deployed diameter is much larger than the packed size, which makes it an enabling technology for new opportunities in space exploration. The HIAD is designed to decelerate and protect spacecraft during atmospheric re-entry. The objective of this research was to improve understanding of structural behavior of HIAD components through material testing, structural testing of components, and numerical models.

The mechanics of inflatable, reinforced braided tubes have been reviewed from a geometric standpoint. Exploratory experimental efforts were performed to quantify the stiffness of the reinforcing cords, which drive axial and bending stiffness of the inflatable tubes. Benchtop inflation tests were performed to quantify longitudinal stiffness and examine instrumentation methods.

The constitutive properties of the braided fabric shell of tori were determined as a function of braid angle and inflation pressure. The shear modulus is highly dependent on braid angle and pressure. Independent testing of extracted fiber tow bundles allowed the effect of de-crimping to be examined with straight tow thickness measured as an upper limit.

Beam bending tests of straight beams with highly controlled loading and boundary conditions were performed for tubes with five different braid angles over a range of inflation pressures. These data sets are ideal for finite element validation due to the highly controlled conditions.

Structural testing of individual tori was performed via radial compression loading. Many improvements were made to the single torus test setup using fixtures provided by NASA. Methods were developed to quantify the 3D shape of the tori and displacements using non-contact photogrammetry methods. The effect of load-control versus displacement-control experiments was investigated and found to result in different response. Finite-element models using three-dimensional shell-elements were developed and compared to the torus experiments. These modeling efforts proved to be challenging and no firm conclusions could be drawn.

ACKNOWLEDGMENTS

TABLE OF CONTENTS

iv

LIST OF TABLES

LIST OF FIGURES

1   INTRODUCTION

1.1   Problem Description

Due to their light weight, ability to be packed into a small volume, and rapid deployment, inflatable structure members are being used increasingly more in civilian, military, and space applications (Turner et al. 2008). The United States National Aeronautics and Space Administration (NASA) has recently investigated Hypersonic Inflatable Aerodynamic Decelerator (HIAD) applications for use in missions such as the Mars Science Laboratory (Litton et al. 2011; O'Keefe & Bose, 2010; Hughes et al. 2005; Cassell et al. 2013). HIADs show great promise as enabling technology for use in space missions because they permit the landing of large payloads due to their substantial frontal area relative to their stowed volume and total weight, and they are also ideal for landings in thin atmospheres (Braun & Manning, 2007; Clark et al. 2009; Wright et al. 2012).

A HIAD is a nose-cone-mounted inflatable structure consisting of multiple, concentric, gas-filled tori (Figure 1-1) that is designed to decelerate and, together with a thermal protection system (see Figure 1-2), protect spacecraft from heat during re-entry as shown in Figure 1-2. The tori are identified with a number signifying their position relative to the center body as T1, T2, T3, etc. as shown in Figure 1-1. Each torus consists of a non-structural impermeable membrane, a braided fabric shell, and axial cords that are integrated within the braided shell of the tori and pre-tensioned during inflation as shown in Figure 1-3.
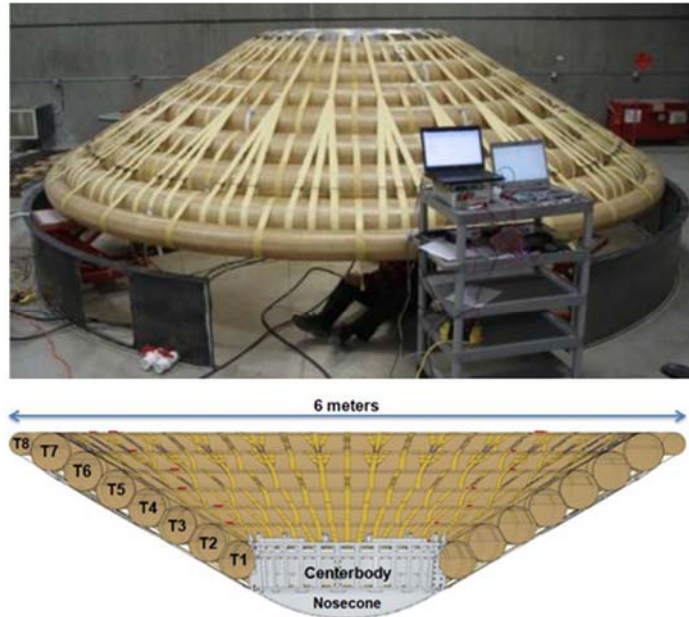
Figure 1-1. Photo and cross-sectional sketch of 6 meter HIAD (Swanson et al. 2012).
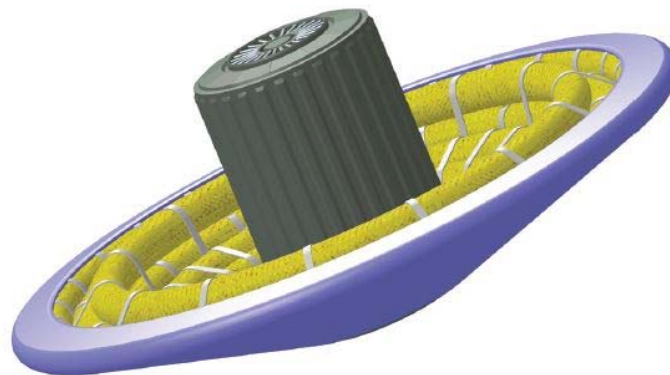
Figure 1-2. Conceptual rendering of HIAD with payload (gray) and flexible thermal protection system (purple) (Young, 2017).
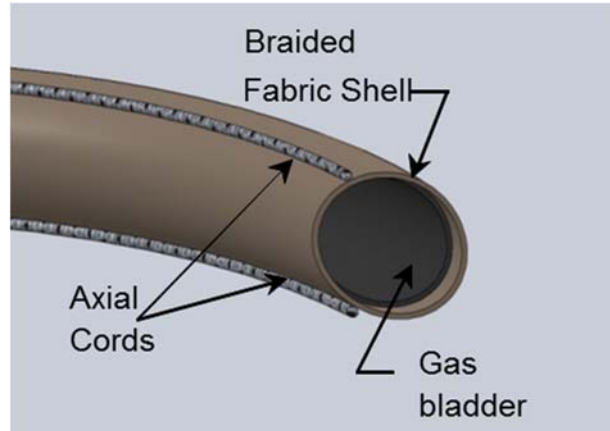
Figure 1-3. Sketch of components of an inflatable, reinforced, braided torus member.

Inflated members are generally constructed of braided fabrics that are comprised of synthetic fibers that are braided into a circular cross-section that can be shaped into straight or curved elements. Pressurized gas, which is contained by an internal, impermeable membrane, provides the braided, tubular members with structural capacity by pre-tensioning the fabric and behaving as a confined gas (Davids, 2007). Braided, tubular fabric members usually have longitudinal reinforcement in the form of integral cords (Jurewicz et al. 2011) or secondarily bonded longitudinal reinforcing elements (Davids, 2009; Brayley et al. 2012). The longitudinal reinforcement provides axial and bending stiffness to the member cross-section, limits longitudinal expansion of the braided shell, and determines the braid angle at the inflated state.

Extensive ground based experimental efforts led by NASA have been conducted to characterize the structural behavior of the 6 meter diameter HIAD, which is the primary focus here. These experiments have included a wide range of structural configurations and loading scenarios including full-scale complete HIAD quasi-static testing using vacuum pressure (Swanson et al. 2014 and Swanson et al. 2015), full-scale complete HIAD wind tunnel dynamic testing (Cassell et al. 2013, Li et al. 2014, Kazemba et al. 2013, and Swanson et al. 2013), full-

3

scale complete HIAD modal testing (Abraham et al. 2014), and HIAD individual torus compression and compression/torsion testing (Chen and Moholt 2014). All test articles for these efforts were constructed by Airborne Systems of Santa Ana, CA, USA with the same braided Technora sleeving/reinforcing cords and impermeable gas bladder architecture described in this document. Technora is a synthetic para-aramid fiber made from co-polymers (Teijin, 2016).

Understanding the structural behavior of inflatable, reinforced, braided fabric, tubular members is critical because full-scale HIAD experiments with realistic loading conditions are highly cost-prohibitive. Instead, reliable, predictive tools such as sophisticated finite-element models are needed that can be validated with a limited set of experimental data. The tests previously conducted by NASA on full HIAD devices and individual tori provided significant useful information, but were relatively complex in terms of loading and boundary conditions and were therefore not ideal to serve as simple model validation cases. Basic constitutive property data is also lacking on the constitutive properties of the braided fabric and reinforcing cords. Finally, there is a need to develop novel experimental techniques for testing braided fabric and measuring fabric response.

1.2   Research Goal and Objectives

The goal of this study is to improve understanding of structural behavior of HIAD components through material testing, structural testing of components, and analysis. Specific objectives designed to achieve this goal are:

1. Conduct exploratory tests to examine the properties of the reinforcing cords that drive bending and axial response of the inflatable members and assess methods for measuring cord strain in-situ.

2. Advance state-of-the-art in the mechanical testing braided fabrics, including the use of digital image correlation (DIC) to assess full-field strain response. Consider braid mechanics from a geometric perspective to account for the effects of deformation and pressure-volume work.

3. Quantify the constitutive properties of all individual components of inflatable, reinforced, braided, tubular members over a range of different braid angles: 55°, 60°, 65°, and 71°. The individual components of these test articles studied here are: reinforcing cords, braided fabric shell, and impermeable gas bladder. The resulting constitutive properties will be essential inputs to simulations of HIAD devices.

4. Perform straight beam bending tests with highly controlled loading and boundary conditions on test articles constructed with a range of different braid angles to provide vital baseline data on the behavior of these composite structural members.

5. Explore methods for structural testing of full-scale tori via radial compression loading. Assess both load- and displacement-control and compare response.

6. Predict the response of a set of tori structural tests using a 3D finite-element model employing shell elements to determine limitations and advantages of such modeling.

1.3   Organization of Thesis

This thesis is organized into six chapters. Chapter 2 covers the basics of netting theory, which was applied to consider the effects of stress and tension. Cord testing is covered in this chapter, as is a discussion of the straight beam test articles, some of which were subjected to

benchtop inflation testing in order to compare stiffness of the tube assembly with the independently tested reinforcing cords and assess methods of cord strain measurement.

Chapter 3 includes tension-torsion testing of the braided fabric. The goal of the tension-torsion testing performed here is to quantify the mechanical properties of the torus shell consisting of Technora (Teijin 2016) braided fabric and a urethane bladder. These tests resulted in measured values for the longitudinal and shear moduli of the shell as a function of braid angle and inflation pressure. The mechanism for increased fabric stiffness with inflation pressure, fabric de-crimping and inter-tow friction is investigated via independent testing of extracted fiber tow bundles as well as an investigation into shell surface flattening with increasing pressure.

Chapter 4 discusses the beam testing. These were highly controlled tests in terms of loading and boundary conditions that provide an ideal set of data for model validation. Improved understanding of the bending behavior of reinforced, inflatable, braided structures is also achieved.

Chapter 5 describes the earlier tests NASA conducted prior to the torus testing done at the University of Maine. A description of the experimental setup is then provided, along with a description and overview of the modeling methodology. Novel methods for quantifying the shape of the torus test articles, a potential key driver of load-carrying capacity if buckling comes into play, are described in detail. Three-dimensional shell-element finite element models are described and comparisons with experimental data are shown.

Finally, Chapter 6 presents a summary, conclusion, and recommendations for future research efforts.

2   BACKGROUND, CORD TESTING, AND EXPLORATORY TESTING

This Chapter focuses on the background and theory related to the mechanics of inflatable, braided tubes and discusses some early exploratory experimental work that was performed. Initially, an in-depth discussion on the mechanics of inflated, braided tubes is presented. Following this, tension testing of individual reinforcing cords is presented, as well as benchtop inflation testing of the straight tube test articles discussed later in Chapter 4. Methods for measuring strains in reinforcing cords integrated within inflatable test articles are investigated.

2.1   *Braid Mechanics and Netting Theory*

Inflatable structures rely on pressurized gas to pretension fabric materials providing them with the ability to carry limited compression and bending loads. The mechanics of braided, inflatable tubes have been described using netting theory (Evans and Gibson, 2002). The geometry parameters of a braided tube are defined, as shown in Figure 2-1, where β is braid angle, r is tube (minor) radius, and x is longitudinal distance between tracer intersections. Netting theory, which relies on simple stress transformations, assumes that all hoop stresses in inflatable braided cylindrical pressure vessels are carried by the braid fibers in tension (Evans and Gibson, 2002). Therefore, if there is no longitudinal restraint, a pressurized cylinder of any initial braid angle will expand or contract longitudinally until the braid angle β is $tan^{-1}\sqrt{2}$ or approximately 54.7° in order to satisfy equilibrium in both the longitudinal and hoop directions. Netting theory treats the braid as a mechanism and does not consider elasticity.
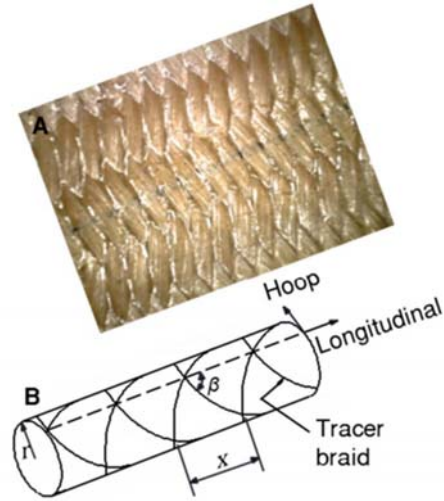
Figure 2-1. A) Close-up photo of 71° braid and B) braided tube features and geometric parameter definitions (Clapp et al. 2016a).

Equation 2-1 gives the longitudinal restraining force, R_{net}, predicted by netting theory that is required to prevent expansion or contraction of an inflated, braided tube as a function of inflation pressure, p, tube radius, r, and braid angle, (Evans and Gibson 2002). In a braided tube with integral reinforcing cords, the cords provide R_{net} for braid angles exceeding 54.7°; as the braid angle grows, the cord pretension due to inflation increases. The approximate angle of 54.7° corresponds to $R_{net} = 0$.

$$R_{net} = p\pi r^2(1 - 2cot^2\beta)$$ Equation 2-1

However, the same braided cylinder can also be considered from the point of view of geometry instead of stress equilibrium. If we consider one helical rotation of a single fiber in the braid and the length of the fiber L_o to be constant, we can define both an original configuration (with subscript "o" to indicate original) as well as a deformed configuration as shown in Figure

2-2.
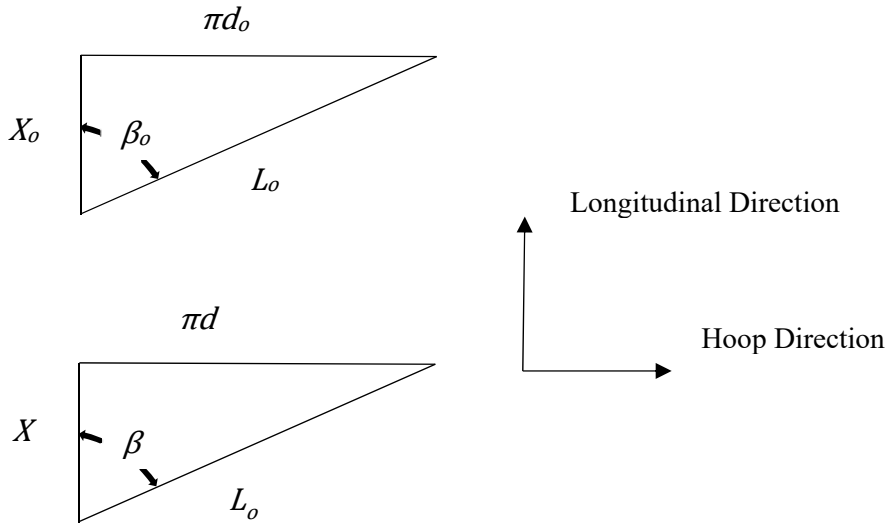
Figure 2-2. Configuration of a braided fiber in one helical rotation (top: original, bottom: deformed).

The original longitudinal length corresponding to one helical rotation X_0, fiber length L_0, original diameter d_0, diameter d, longitudinal distance for any braid angle X, and volume *vol* are defined in Equation 2-2 through Equation 2-6, respectively.

$$X_0(d_0, \beta_o) = \pi \cdot d_0 \cdot cot(\beta_0) \qquad\qquad \text{Equation 2-2}$$

$$L_0(d_0, \beta_0) = \sqrt{X_0(d_0, \beta_0)^2 + (\pi \cdot d_0)^2} = \pi \cdot d_0\sqrt{1 + cot(\beta_0)^2} \qquad\qquad \text{Equation 2-3}$$

$$d(\beta, d_0, \beta_0) = L_0(d_0, \beta_0) \cdot \frac{sin(\beta)}{\pi} = sin(\beta)\, d_0 \cdot \sqrt{1 + cot(\beta_0)^2} \qquad\qquad \text{Equation 2-4}$$

$$X(\beta, d_0, \beta_0) = L_0(d_0, \beta_0) \cdot cos(\beta) = \pi \cdot d_0 \cdot cos(\beta) \cdot \sqrt{1 + cot(\beta_0)^2} \qquad\qquad \text{Equation 2-5}$$

$$vol(\beta, d_0, \beta_0) = X(\beta, d_0, \beta_0) \cdot \pi \cdot \frac{d(\beta, d_0, \beta_0)^2}{4} = \frac{d_0 \cdot cos(\beta) \cdot sin(\beta)^2 \cdot (1 + cot(\beta_0)^2)^{\frac{3}{2}}}{4} \qquad\qquad \text{Equation 2-6}$$

The braid angle that maximizes the volume can easily be obtained by differentiating Equation 2-6 and finding the positive root, which of course yields the same $tan^{-1}\sqrt{2}$ angle that results from netting theory. The volume of a braided cylinder with maximum normalized volume of unity is shown in Figure 2-3 with a clear peak at about 54.7°.
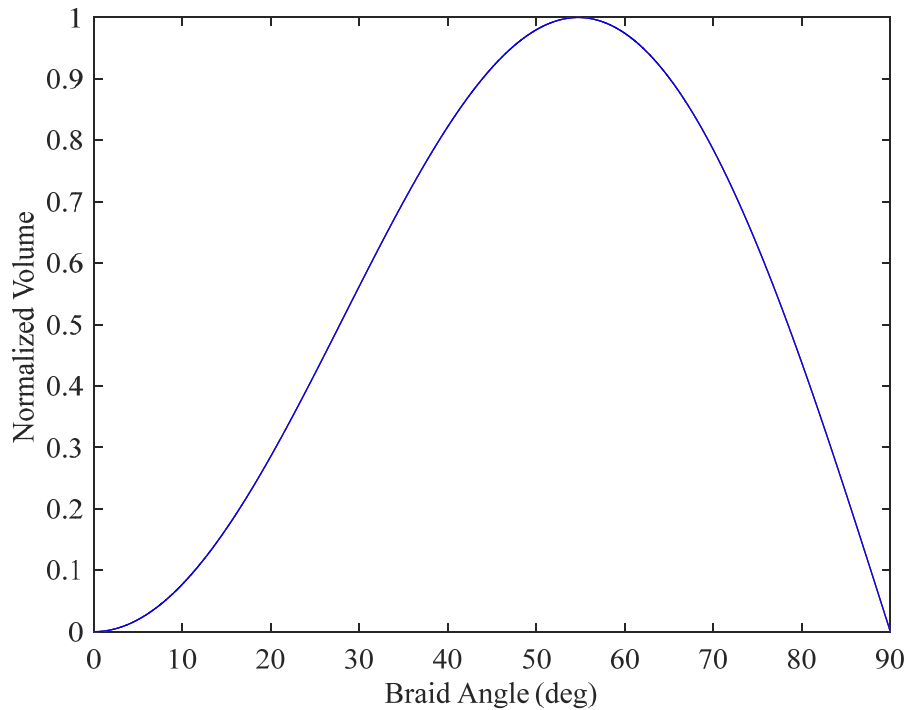
Figure 2-3. Normalized volume of a braided cylinder.

Young (2017) developed an expression for the effective in-plane Poisson ratio ν_{LH} of an orthotropic material by relating netting theory and Hooke's law as shown in Equation 2-7. The exact expression for an infinitely stiff fiber can also be determined using the previously presented geometric Equations and the definition of Poisson's ratio (Equation 2-8) as shown in Equation 2-9. The exact expression, however, is not ideal for input to finite element or other elasticity-based models to define an orthotropic material because it varies with braid angle.

10

$$v_{LH} = \cot^2(\beta)$$

Equation 2-7

$$v_{LH} = -\frac{\varepsilon_H}{\varepsilon_L}$$

Equation 2-8

$$v_{LH} = -\frac{1 - \sin(\beta) \cdot \sqrt{1 + \cot(\beta_0)^2}}{1 - \cos(\beta) \cdot \tan(\beta_0) \cdot \sqrt{1 + \cot(\beta_0)^2}} \approx \cot^2\beta$$

Equation 2-9

To examine the effect of the simplification inherent in Equation 2-7, the simplified expression and the more exact expression of Equation 2-9 were used to estimate the volume change of a braided cylinder since this is proportional to the pressure-volume work if pressure is constant. As an example, consider a braided tube with nominal initial braid angle of 71° with 345 mm diameter and assume that the fibers are infinitely stiff in the fiber direction, but otherwise free to rotate. Figure 2-4 shows the error between the exact volume change and the volume change predicted using Equation 2-7 and Equation 2-8 over the range of braid angles from 70° to 72°. The error is less than 1% for a 1° change in braid angle in either tension or compression. Thus, if v_{LH} is taken as approximately $\cot^2(\beta)$ in a finite element model that includes nonlinear geometric effects (large deformations) along with inflation pressure modeled with follower forces, the work done by pressure will be accurately captured for reasonably small changes in braid angle. Note that v_{LH} cannot be exactly $\cot^2(\beta)$ or ε_L will be zero and the reinforcing elements will not be pretensioned by inflation.
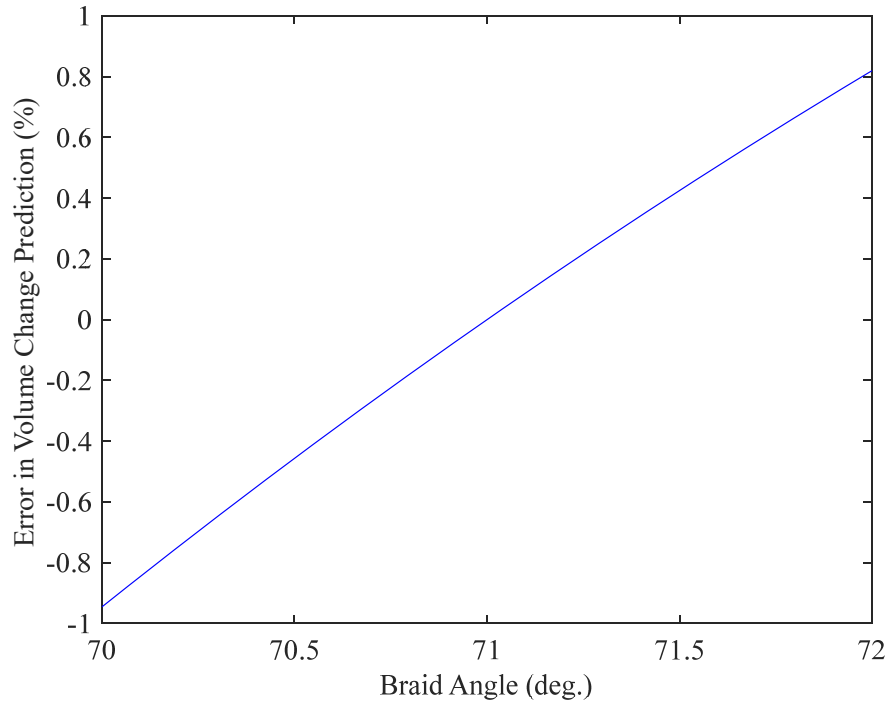
Figure 2-4. Error in volume change calculation using simplified equation for ν_{LH}.

The geometric stiffness of the braided cylinder subjected to axial deformation can also be calculated using the previously presented equations. As an example, consider the beam modeled in Clapp et al. (2016b) with as-nuilt diameter of 340 mm as-built braid angle of 70.56° inflated to 138kPA. The predicted longitudinal geometric stiffness of this beam is shown in Figure 2-5. The longitudinal stiffness at the as-built braid angle is 8.77 N/mm.
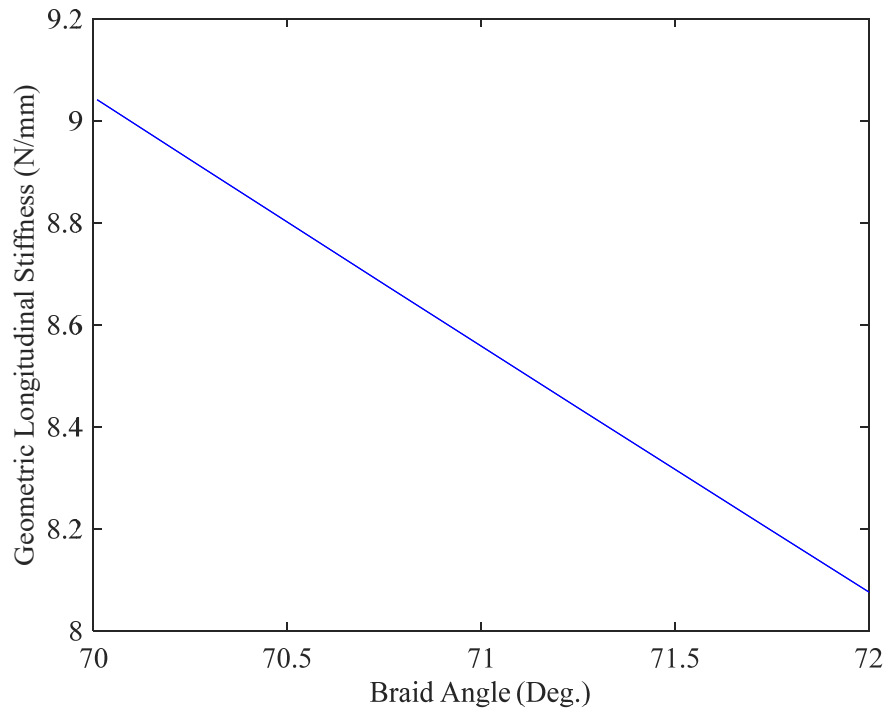
Figure 2-5. Predicted longitudinal geometric stiffness of braided tube with 340 mm diameter, 70.56° braid angle, inflated to 138 kPa.

The beam model developed in Abaqus (2014) and described in Clapp et al. (2016b) was modified slightly to permit a comparison with the theoretical geometric stiffness described here. The model was simplified to only include the inflatable tube, which was lengthened to 2.54 m to minimize the effect of boundary conditions at the plane of symmetry. Fixed boundary conditions were applied to the circle of nodes located away from the plane of symmetry as shown in Figure 2-6. The model consisted of two steps:

1. Apply internal pressure as a follower force.

2. Apply a displacement to the nodes with fixed boundary conditions to cause 0.01% longitudinal strain.
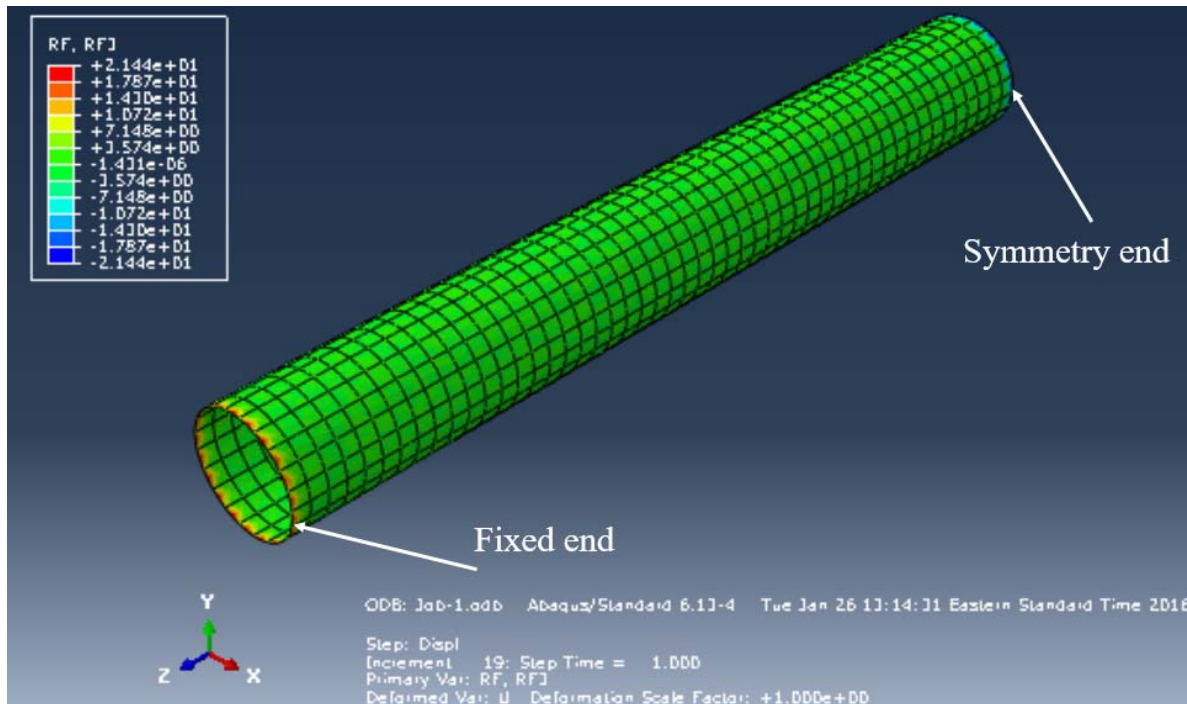
Figure 2-6. Finite element model to investigate geometric stiffness due to work done by pressure.

The total longitudinal stiffness was calculated as the difference of the sum of longitudinal reactions in Step 2 vs. Step 1 divided by the original diameter. The total longitudinal stiffness from the model was determined to be 21.8 N/mm. This value minus the total longitudinal elastic stiffness of the braided tube and bladder of 12.8 N/mm resulted in a geometric stiffness of 8.92 N/mm, which is 1.7% greater than predicted by theory, thus confirming that it is capturing the pressure-volume work with reasonable accuracy.

An important implementation detail is that nonlinear geometric effects must be activated in the Abaqus (2014) FE model in order to obtain the predicted total longitudinal stiffness. Another observation is that using the 4-noded S4 element instead of the 8-noded S8R also resulted in a significant under-prediction of geometric stiffness with only about 27% of the geometric stiffness captured as compared to the value using S8R elements.

The geometric stiffness reported here has a significant effect on the longitudinal stiffness of a braided tube subjected to only axial deformations. However, it has minimal effect on the bending stiffness of the shell if the neutral axis is near the middle of the cross-section since the volume change and therefore pressure-volume work will be minimal. It is important to ensure that the pressure-volume work is accurately captured directly in the finite element model (e.g. Clapp et al. 2016b; Young 2017) or indirectly accounted for (e.g. Young et al. 2017a; Young et al. 2017b).

2.2 Reinforcing Cord Properties

While they remain pre-tensioned, the reinforcing cords provide the vast majority of longitudinal stiffness for the braided, inflatable structures investigated as part of this work since the braided fabric shell and gas bladder have minimal longitudinal stiffness. Thus, some of the first experiments that were performed were tension tests of the reinforcing cords to assess their load-deformation response. The data from these tests is also key input to any computational or analytical model of a reinforced, braided structural member.

Independent quasi-static uniaxial tension testing of the braided Technora (Teijin, 2016) cords was performed on a servo-hydraulic test machine by both Young and Clapp. Test Resources G76-20-9 Capstan grips were used to grip the ends of the cord as shown in Figure 2-7. The ends of the cords were coated with epoxy to facilitate load transfer among the fiber tow bundles in the braid. The cords were wrapped around the capstan grips and the ends were clamped to prevent slipping. A 50 mm gage length extensometer was used to monitor the strain in the cord as loads were applied (Figure 2-7).
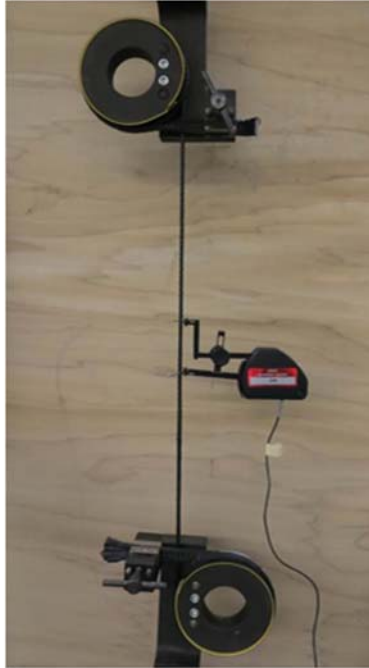
Figure 2-7. Photo of instrumented cord in tension test fixtures.

Three of the cords (#1-3) were in pristine condition, whereas three others were extracted from a straight tube after the completion of the bending tests described in Chapter 4. Figure 2-8 shows a photo of a cord prior to extraction.

Figure 2-8. Photo of cord in straight tube prior to extraction.

Three cycles of loading were applied to each cord. The peak load applied for the first two cycles was about 11 kN, which was chosen to exceed the maximum expected cord force in the tube bending tests based on preliminary models. The peak load for the third load cycle was about 12 kN in order to capture the behavior greater than expected peak load in case this situation is for nonlinear FE models simulations, which may require cord load-strain data beyond the expected range to achieve a solution. Between loading cycles, the load was decreased to 0.2 kN.

The cord load-deflection test results are presented in Figure 2-9. The responses of the three extracted cords were very similar, so only one (#4) is shown for clarity. The initial strain at low loads during the first loading was highly variable among the cords because the zero strain state is not well defined for braided rope-like structures. In other words, there was an apparent shift in the strain data for each cord due to the strain value that was taken as zero. Therefore, for comparing response all strain data were shifted to be coincident at a load of 3.2 kN on the second load cycle (see square symbol in Figure 2-9). The data for Cord 1 was not shifted, thus the strain

values shown here are somewhat arbitrary. This load value was chosen because it is the expected

load in the cords for the 71° tube inflated to 138 kPa per Equation 2-1. All curves were in

agreement after this adjustment was applied, which indicates that the load-strain response is

repeatable after the cords have been subjected to significant tension and load cycling.

Identical tests were also performed on cords extracted from the tube bending test

specimen after bending tests had been performed as described in Chapter 4. These extracted

cords exhibited load-strain response that was very similar to that of the pristine cords, indicating

that there was no significant stiffness degradation due to load cycling.
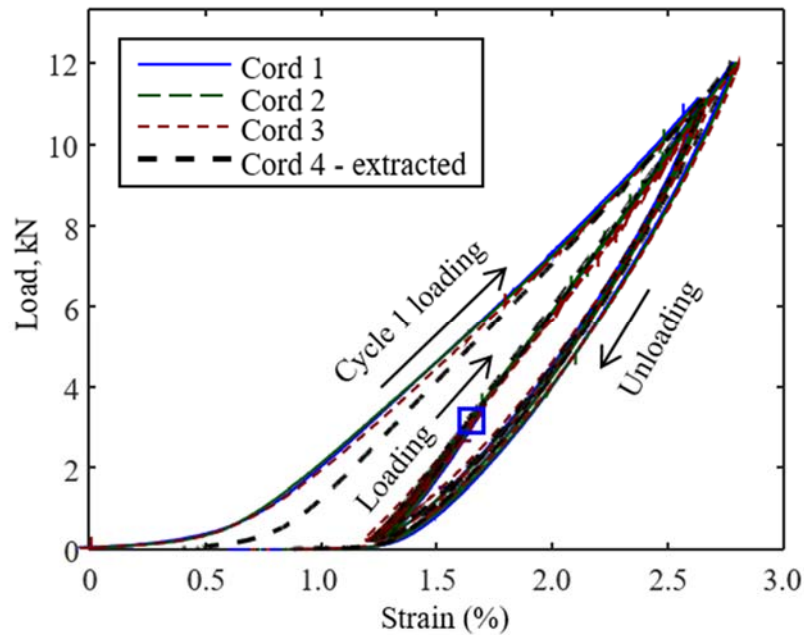
Figure 2-9: Reinforcing cord cyclic load response.

2.3   *Benchtop Inflation and Strain Gage Study*

Benchtop inflation tests were also performed early in the experimental efforts to enable

comparisons between the independent cord tests and the response of the whole tube assembly

with three cords, a braided fabric shell, and internal gas bladder. An additional objective of these tests was to assess the usefulness of different methods of strain measurement for braided, inflated tubes and tori. These tests involved the straight tubes that were subjected to bending tests as described in Chapter 4. The benchtop inflation tests required placing the tubes onto a smooth table with minimal friction and cord strains were monitored as the tubes were inflated.

2.3.1. Strain Measurements

One of the primary drivers of the structural behavior of inflatable, braided tubes is the stiffness of the reinforcing cords, since they are the primary elements affecting axial and bending response. As shown in Section 2.2, the cord force-strain relationship is highly nonlinear. Therefore, the most logical method for tracking the cord stiffness or load is to measure strains during loading of the structural elements. Three methods for measuring strains are described in this Chapter.

2.3.1.1 Digital Image Correlation

Measurements made with digital image correlation (DIC) rely on many techniques including photogrammetry. Principles of photogrammetry were first developed as a means to create maps from aerial photographs (Mikhail et al. 2001). Digitized light intensity values across a rectangular array of pixels is measured by the cameras. The correlation process is well documented for three-dimensional DIC (Kahn-Jetter et al. 1990; Luo et al. 1993; and Sutton et al. 2009). The cameras are calibrated using a series of photos of a calibration object with precisely measured distances between reference points input to the software. The software uses photogrammetry principles of triangulation and bundle adjustment (Mikhail et al. 2001) to

determine the position of the cameras relative to each other and the internal distortion parameters of each lens (Avitabile et al. 2010).

ARAMIS (2011) software uses photos of specimens that are painted with a stochastic black and white pattern. The software creates a grid of facets and precisely locates the 3D coordinates of the center of each facet by locating the facets in each image and using the calibration information. PONTOS (2011) software uses the same photogrammetry algorithms, but instead of tracking a random pattern, it precisely finds ellipses (a perspective view of reference circles) and assigns 3D coordinates to the image pixels, compares the digital images, and computes the displacement of the reference points in all stages of the project. ARAMIS (2011) is used in this Chapter to measure strains, whereas PONTOS (2011) is used in Chapter 5 to track reference points.

2.3.1.2 *Liquid Metal Strain Gages*

The DIC systems are an excellent tool for measuring strains in many situations. However, they can only monitor one region of limited size, and they cannot be used if the region of interest is not visible to the cameras. Therefore, NASA expressed interest in alternative options that would help overcome some of these limitations. At the start of this project, the most promising sensor for measuring the strain in the cord was a liquid metal strain gage (LMSG). These gages are very flexible, so they would easily be able to deform with the cord. Traditional metal foil gages were suspected to potentially be too stiff, therefore the reading would be less than the true strain in the cord. For reference, a close-up photo of a LMSG with 32 mm gage length adjacent to a reinforcing cord on the surface of an inflated, braided tube is shown in Figure 2-10.
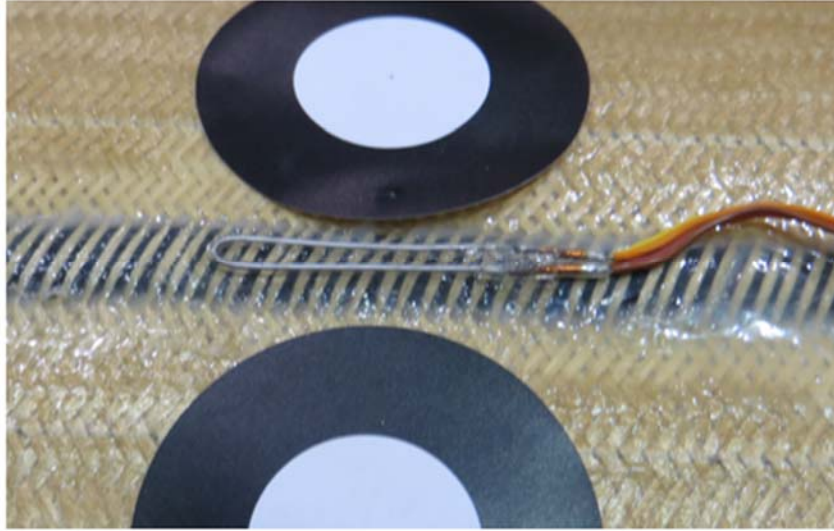
Figure 2-10. Photo of liquid metal strain gage courtesy of Nino Piazza, NASA Armstrong.

LMSGs were used successfully by NASA Armstrong to measure strains during testing of single tori in 2013-2014 (Chen and Moholt 2014). However, they are several times more expensive than traditional foil gages and monitoring LMSG output required a customized data acquisition system that was very sensitive to environmental conditions including temperature changes. The building cooling system had to be turned off while data was being collected, which caused major temperature spikes since the NASA-Armstrong facility is in the Mojave Desert.

The University of Maine attempted to use the LMSGs, but efforts were abandoned because of the inability to get consistent data readings without relying on the expensive data acquisition system supplied by the manufacturer.

2.3.1.3   *Traditional Metal Foil Resistance Strain Gages*

Traditional metal foil resistance strain gages are relatively inexpensive compared to LMSGs and are very widely used and accepted. They are easily monitored with data acquisition

equipment that is readily on hand at many testing facilities. The concern, however, is that they may be stiffer than the coating that is applied to the cords, and therefore would indicate strain readings that were less than those in the cord. A photo of two foil gages with 25 mm gage length is shown in Figure 2-11 mounted on a straight tube during preliminary testing.
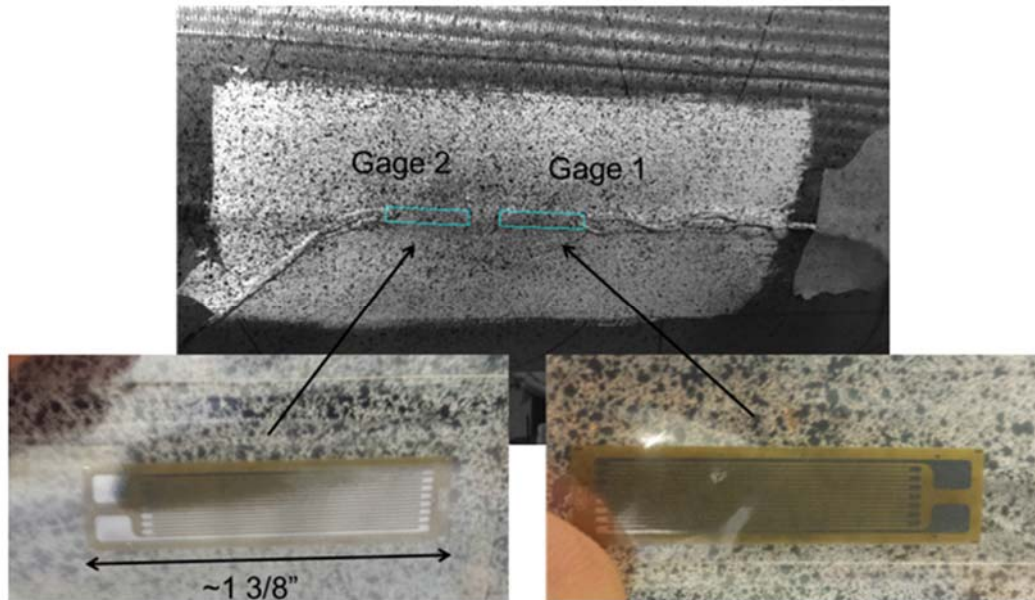
Figure 2-11. Photo of metal foil resistance gages with 25 mm gage length on straight tube.

2.3.2 Inflation Strains Compared to Cord Tension Tests

Strains were monitored during inflation tests. The ARAMIS DIC system was the primary method used to collect general information the specimen was monitored as air pressure was slowly added up to nominally 138 kPa of pressure. The load in the each of the three cords was estimated as 1/3 of the total reaction force predicted using Equation 2-1 along with measured values for pressure, diameter, and braid angle. The data from both a tension test of an

independent cord as well as two of the benchtop inflation tubes with 71° and 65° braid angles are

shown in Figure 2-12.
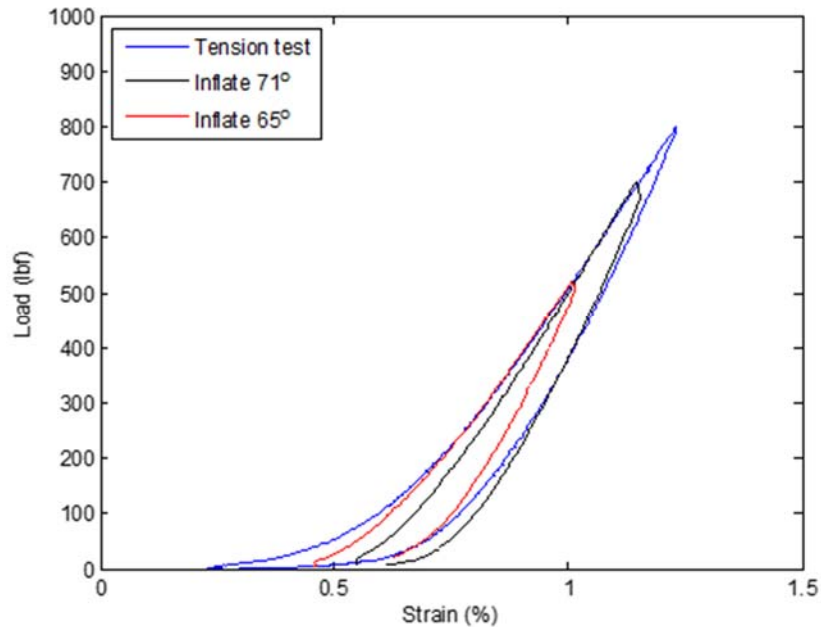
Figure 2-12. Load strain relationships for independent cord and 2 straight tubes.

The curves obtained through the inflation tests match well with that of the tension test

including both loading and unloading for the tube with 71° braid angle. This indicates that the

cord stiffness does in fact dominate the longitudinal stiffness of the tubes as expected.

2.3.3 Foil Gages Compared to Digital Image Correlation

The feasibility of using metal foil resistance strain gages was investigated by performing

a series of inflate-deflate tests. A foil gage with 51 mm gage length was bonded to the cord using

the same procedures as those recommend for bonding to composites. The gage was bonded with

the tube inflated to 34 kPa. A 51 mm gage length was selected to provide a representative

average since significant local variations in strains were apparent based on visual inspection of

the DIC surface data. The gage and tube were then painted with the stochastic black and white pattern to a tube with 71° braid angle. The pressure was decreased to 1.7 kPa, which was the lowest pressure that would still result in a low risk of damage due to the foil gage due to wrinkling. Five inflate-deflate tests were then performed with peak pressure of 138 kPa and minimum or 1.7 kPa. Five tests were performed because the response generally was repeatable after five cycles or less. The longitudinal strain field for cycle 5 overlaid on a photo of the painted region is shown in Figure 2-13. The outline of the foil gage is indicated by the black lines. It is apparent in Figure 2-13 that there are no drastic discontinuities in the strain field at the edges of the strain gage meaning that the value of strain does not undergo a large change in value from the top of the gage to the fabric next to the gage.
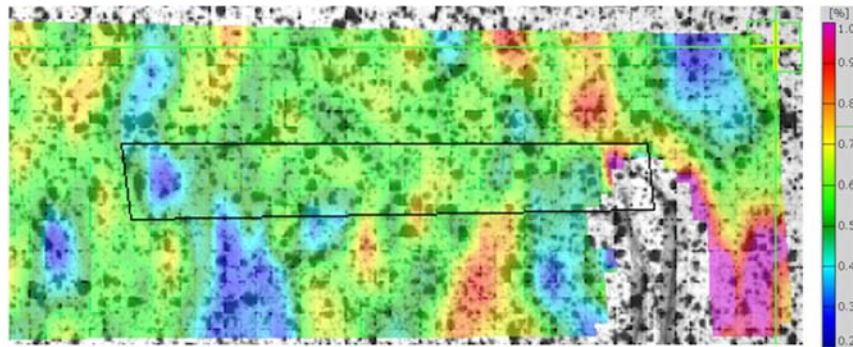
Figure 2-13. Longitudinal strain overlay with outline of foil gage indicated by black lines.

Next, the strain gage was removed from the specimen and the area where the gage was located was immediately painted for the DIC system. The inflation test was repeated again as soon as the paint was dry enough. The strains on the 5th cycle recorded by the foil gage as well as the strains recorded by ARAMIS both with and without the gage attached are shown in Figure 2-14. The strains recorded by ARAMIS are in excellent agreement with the foil strain gage for the first series of inflation tests as expected. The strains recorded by ARAMIS for the second series

of inflation tests are also in good agreement with the foil gage. In fact, the response is slightly

stiffer at higher pressures, which may simply be due to additional stiffening due to hysteresis

since it is really a comparison of cycle 10 to cycle 5.
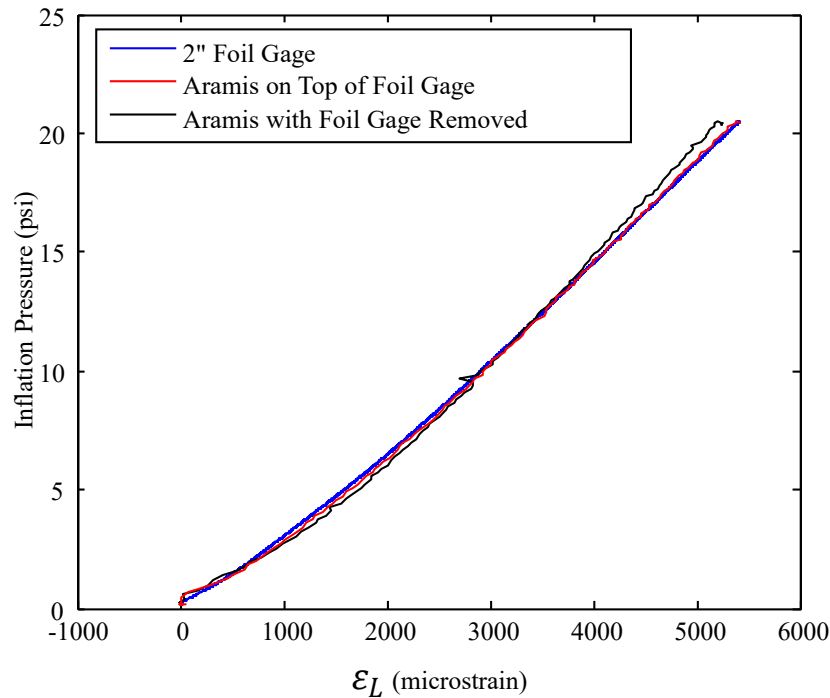
Figure 2-14. Longitudinal strains with and without foil gage attached.

The results of this testing led to NASA electing to use the same foil strain gages in their

2014 tests of a full-scale 6-meter diameter HIAD (Swanson et al. 2015) in lieu of the more

expensive and more difficult-to-use LMSGs. The foil strain gages were successfully used to

estimate forces in the torus reinforcing cords.

2.4 Summary

The mechanics of braided, inflatable cylinders were reviewed both in terms of the

traditional stress transformation method (netting theory) as well as a geometric approach. It is

shown that there is a geometric stiffening due to pressure-volume work if the inflation pressure is constant. It is shown that it is reasonable to use an approximate value for Poisson's ratio and accurately capture the work done by pressure. A simple finite-element model using this approximate value of Poisson's ratio was shown to be in good agreement with the predicted geometric stiffening term using exact solutions for a fiber that is infinitely stiff in the fiber direction, but otherwise free to rotate.

Simple tension tests were performed to quantify the load-strain relationship of the integral, tube reinforcing cords. The response on the first cycle of loading is highly variable because the previous state of the cords is unknown and not controlled. However, after a complete load-unload cycle the behavior is very similar for all cords testing including both pristine independent cords as well as cords extracted from straight tubes after the bending tests were performed as described in Chapter 4. Cord load-strain response is generally nonlinear, and the load-strain data gathered from these cord tests is vitally important for predicting the load-deformation and load-strain response of inflated, braided tubular structural members.

Benchtop inflation tests were performed to assess the stiffness of straight tubes relative to the stiffness of individual reinforcing cords. The load in the cords was estimated based on netting theory. It was found that the stiffness of the straight tubes is very similar to the stiffness of independent cords, which confirms that the cord stiffness dominates the overall response.

Methods for measuring cord strains other than DIC were investigated. Relatively long foil strain gages were found to work very well and it was confirmed via comparison to DIC that they are not too stiff to accurately measure cord response. Based on the benchtop testing

26

documented here, NASA has adopted foil strain gages as their method for measuring cord strains in their large-scale full HIAD tests where it is impossible or impractical to use DIC systems.

3   TENSION-TORSION TESTING

This Chapter addresses the tension-torsion testing of inflated, braided tubes to determine effective constitutive properties. A description of the test articles is given. The experimental methods of this testing are described. Further analyses and observations are presented.

Extensive ground based experimental efforts led by NASA have been conducted to characterize the structural behavior of the 6 meter diameter HIAD, which is the primary focus here. These experiments have included a wide range of structural configurations and loading scenarios including full-scale complete HIAD quasi-static testing using vacuum pressure (Swanson et al. 2014 and Swanson et al. 2015), full-scale complete HIAD wind tunnel dynamic testing (Cassell et al. 2013, Li et al. 2014, Kazemba et al. 2013, and Swanson et al. 2013), full-scale complete HIAD modal testing (Abraham et al. 2014), and HIAD individual torus compression and compression/torsion testing (Chen and Moholt 2014). All test articles for these efforts were constructed by Airborne Systems of Santa Ana, CA, USA with the same braided Technora sleeving/reinforcing cords and impermeable gas bladder architecture described in this Chapter.

The tests previously conducted by NASA on full HIAD devices and individual tori provided significant useful information, but were relatively complex in terms of loading and boundary conditions and were therefore not ideal to serve as model validation cases. Basic constitutive property data was also lacking on the constitutive properties of the braided fabric.

While many methods exist for determining the constitutive properties of fabrics (Turner et al. 2008; Hutchings and Braun, 2009; Kabche et al. 2011), tension-torsion testing of inflated

tubes (Turner et al. 2008; Brayley et al. 2012; Hutchings and Braun, 2009; Kabche et al. 2011) is most applicable in this instance because it allows the effect of inflation pressure and the internal gas barrier to be directly captured. In this research non-contact DIC measurements are used extensively to capture the geometric information required to consider the braided tube as a mechanism via netting theory (Evans and Gibson 2002).

Prior to this study, NASA's finite element models used back-calculated mechanical properties (E1, E2, G12, and ν12) as inputs to define the elastic properties the braided shell plus bladder as a single material. While this is valid and is often the only option, a more justifiable approach is to independently quantify the mechanical properties of components and use the measured values as inputs in the finite element model. In order to achieve this objective, a new servo-hydraulic tension-torsion machine was purchased from Shore Western Manufacturing with 100 kN axial capacity and 1130 Nm torque capacity. The new machine has over four times more axial load capacity and 11 times more torque capacity compared to the Instron tension-torsion machine used in prior studies at the University of Maine. A photo of the testing machine is shown in Figure 3-1. End fixtures have been fabricated to allow the specimen to be inflated during testing. A method for gripping the specimens has been developed to prevent slippage as tension or torsion loads are applied to the specimens. Specimens with four different braid angles were fabricated for tension-torsion testing by the University of Maine using braid and liner materials provided by NASA.
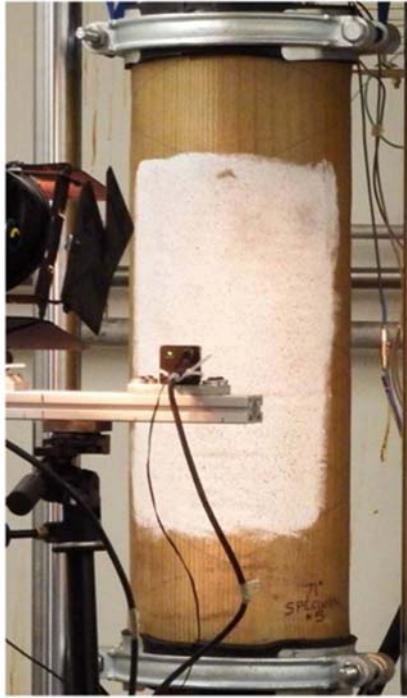
Figure 3-1. Tension-torsion setup.

3.1 Test Article Description

All materials used for testing were provided by NASA Langley Research Center.

Materials consisted of an impermeable urethane gas bladder with thickness of about 0.3 mm,

triaxial braided sleeving with thickness of about 0.2 mm, and a low-modulus two-part

polyurethane coating that is added to improve durability and help hold the bias braid fiber tows

in place at the desired braid angle during article fabrication, packing, handling, and inflation. The

polyurethane coating was also used in the full-scale HIAD test articles that have been tested and

analyzed by NASA. It should be noted that although thicknesses are provided here for reference,

all stresses and moduli are presented as membrane resultants with units of force per

circumferential length.

The triaxial sleeving consisted of axial nylon hot melts as well as Technora bias fiber tows at four different nominal angles, β, (55°, 60°, 65°, and 71°). The axial nylon hot melts are intended to help lock the bias braid at the target angle, have a very low stiffness, and do not add to the structural capacity. All braid material was sized by the manufacturer to have a nominal use diameter, d, of 345 mm. However, since the objective of the experiments described here was to quantify the properties of the braid used in the construction of the full-scale HIAD test articles (Cassell et al. 2013; Swanson et al. 2014; Clapp et al. 2015; Clapp et al. 2016b), the as-built diameter was adopted as the target for specimen construction. The actual diameter of several corresponding straight tube and tori articles was found to be less than nominal and ranged from 338 mm to 342 mm.

Ideally, the articles used for the testing described in this paper would have been fabricated by Airborne Systems, the manufacturer of beams, tori and HIAD devices. However, this was not possible due to project constraints, and the articles were fabricated by the University of Maine. A custom-sized mandrel with 340 mm diameter was constructed to assist in the fabrication of three specimens at each of the four braid angles. The urethane bladder and braided sleeving were placed on the mandrel and the sleeving was carefully aligned so that the bias braid was set to the target angle. This was achieved by satisfying Equation 3-1:

$$x = n_{rev} \, \pi \, d \, cot(\beta),$$
<div align="right">Equation 3-1</div>

In Equation 3-1, x is the distance between tracer intersections, n_{rev} is the number of revolutions between intersections, and the other parameters are previously defined. Equation 3-1 defines the basic geometry of a braided tube and contains a close-up photo of a coated 71° braid.

The polyurethane coating was added to the fabric to be consistent with the fabrication of all the other test articles previously mentioned. The amount of polyurethane coating applied was the minimum required to achieve 100% surface coverage. The look and texture of the exterior coating was very similar to that of the articles procured from Airborne Systems. However, the areal weight of the coated braid described here was about 58% higher than the areal weight of coated braid extracted from other test articles, which implies that significantly more coating was applied. This may have stemmed from the fact that the coating was applied in this study to unpressurized fabric, whereas the test articles may have been coated in an inflated state resulting in less penetration. In order to estimate the effect of the additional coating on the longitudinal modulus of the braid, the additional areal weight of the coating was used with the manufacturer's specified density and modulus to estimate a 0.06 N/mm, which is much less than longitudinal values measured in this study. The as-tested diameter and braid angle of each of the twelve specimens is shown in Table 3-1 as a function of inflation pressure for 34-138 kPa.

Table 3-1. Summary of actual tension-torsion specimen geometric values.

Nominal Braid Angle	Inflation Pressure (kPa)							
	34	69	103	138	34	69	103	138
	Actual Diameter (mm)				Actual Braid Angle			
55°	340	341	342	343	53.6°	53.6°	53.7°	53.8°
	335	336	337	338	54.0°	54.1°	54.2°	54.3°
	339	341	342	343	55.0°	55.3°	55.5°	55.6°
60°	335	336	337	337	59.5°	59.6°	59.7°	59.8°
	338	338	339	340	60.0°	60.0°	60.1°	60.2°
	338	339	340	341	59.8°	59.9°	60.0°	60.2°
65°	336	336	337	337	64.2°	64.2°	64.2°	64.2°
	341	341	341	342	64.7°	64.7°	64.7°	64.7°
	337	337	338	338	64.8°	64.9°	64.9°	65.0°
71°	342	342	342	343	71.3°	71.3°	71.3°	71.4°
	342	342	342	343	70.9°	70.9°	70.9°	70.9°
	343	343	343	343	70.6°	70.6°	70.6°	70.5°

3.2 Tension-Torsion Experimental Methods

A Shore Western Model 306.2 servo-hydraulic tension-torsion machine was used to conduct the tension-torsion tests described in this paper. The load and torque capacities of the machine are 100 kN and 1130 N-m, respectively. End fixtures for mounting the tension-torsion specimens to the machine were fabricated from circular steel plates with a diameter of 338 mm and thickness of about 51 mm. A layer of 3 mm thick rubber was placed around the circumference of the steel plates. Compressed air was supplied through the lower fitting and the

pressure was monitored through the top fitting using a Setra Model 206 pressure transducer with operating range of 0-345 kPa.

Specimen installation, alignment, and gripping proved to be a major challenge. Several methods were explored and ultimately the best results were achieved by coating the end fixtures with soap and water to allow the specimens to easily slide over the rubber. Compressed air was then added prior to clamping the specimens, which allowed the specimens to self-align as the air escaped at the ends. Once the soap and water dried, a layer of 13 mm rubber was wrapped around the outside of the tube at each end and heavy-duty double-bolt clamps were used to secure the specimen to the fixtures. It was not possible to achieve a perfect air seal, so the pressure was regulated to ±1 kPa during testing. For all specimens, the clear distance between end fixtures was at least three times greater than the tube diameter to minimize end effects. A specimen installed in the machine is shown in Figure 3-2.

Figure 3-2. Photo of a specimen installed in the tension-torsion test machine.

The actuator was positioned such that the braid angle corresponded to as-built braid angle

of other test articles (Cassell et al. 2013; Swanson et al. 2014; Clapp et al. 2015). The

displacement rate was set to 25 mm/min and actuator was raised 25 mm (compression), lowered

50 mm (tension), and then returned to the starting point. Nearly zero torque was maintained

throughout this process. These displacements result in strains that are greater than tolerable

levels for typical structural applications.

The machine was switched to torque-control and a target torque/minute was applied in the

positive and negative directions to achieve the following positive and negative torques for 3.4,

34, 69, 103, and 138 kPa: 11, 56, 113, 169, and 226 N-m, respectively. A constant axial reaction

was maintained throughout this process. These torque values were large enough to result in shear strains that were well beyond the strain resolution of the DIC system. Preliminary testing at higher torque levels produced very similar results, but some specimens experienced fabric buckling at high torque values rendering the specimens unsuitable for further testing. The cause of the buckling was misalignment of the specimens. Larger torque values can be applied with better alignment, but for sake of collecting complete data sets, the peak torque values were less than initial testing to reduce the likelihood of buckling. The tension and torsion loading regimes were each applied twice more for a total of three tension/torsion loading cycles.

3.3 Gas Bladder Experimental Methods

Since the magnitude of E_L was expected to be small, the gas bladder material was independently tested to examine its contribution to stiffness. It was tested both using uniaxial tension testing of five 25 mm wide coupons and tension and torsion testing of an inflated gas bladder, as shown in Figure 3-3. Only one full gas bladder was tested due to the availability of materials. Digital image correlation was used to measure strains with both methods. The tension and torsion tests were conducted with the air bladder inflated to only 1.4 kPa because this is the pressure that resulted in a diameter consistent with the braided test articles described above.
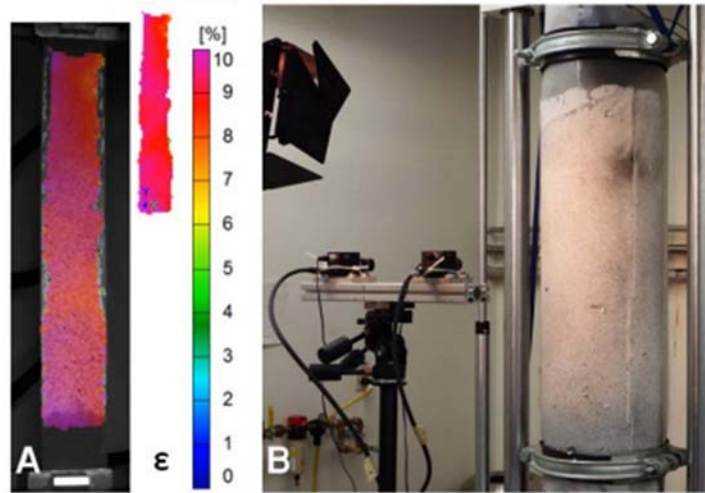
Figure 3-3. A) ARAMIS view of bladder coupon and B) bladder tension-torsion test.

3.4 Data Collection and Analysis

Axial force, torque, actuator axial position, actuator angular position, and air pressure were recorded at a rate of 10 Hz during testing. Digital images of the specimen surface were captured using one pair of 5M cameras with 12 mm focal length lenses at a rate of 1Hz. ARAMIS DIC software version 6.3 (2011) was used to process the images. All strain calculations used DIC data information rather than actuator axial or angular position. The DIC cameras were mounted to a horizontal camera bar and were positioned to view the mid-height region of the tube. The width and height of the resulting computed region were approximately 260 by 300 mm, respectively.

The initial position of the actuator was set such that x satisfied Equation 3-1 for the target braid angle, where x was taken as the average distance between tracer fiber intersections at four locations around each tube at an inflation pressure of 34 kPa. The value of d in Equation 3-1 was determined with the ARAMIS software by using the "Best-Fit-Cylinder" feature. Two unique

points within the paint pattern that remained within the camera's view throughout testing were chosen and used to monitor the distance between the points during testing. It was assumed that the tracer intersection distance x changed proportionally to the distance between the unique points, which allowed estimation of the current braid angle for all stages per Equation 3-1.

Some post-processing was necessary within the DIC software package. The stage at which the tube reached the target inflation pressure was determined and this stage was set as the strain reference stage. A best-fit cylinder and two points on the z-axis (as opposed to the radial or tangential axes) of the cylinder were created. The raw coordinates were transformed to align the cylinder local z-axis with the ARAMIS global Y-axis. The distance between unique points was measured (each stage has a unique measurement) and exported. Three-dimensional point cloud sections were created near the top and bottom of the field of view with constant ARAMIS global Y-values for all points in the strain reference stage and then exported.

A MATLAB (2012) script was written to post-process the exported DIC data. For each section and stage, the best-fit diameter of the tube was determined using least-squares. Note that the diameters described here only use section point cloud points, whereas the best-fit cylinder described earlier used all 3D coordinates. The purpose of the cylinder was to facilitate an accurate global coordinate transformation. The section coordinates are used for determining rotations, so the local diameter was used in conjunction to yield the most accurate rotation values. The section diameter values were not meaningful at very low inflation pressures because the tube cross-section was not circular. The longitudinal strain, ε, and in-plane engineering shear strain, γ, respectively, were calculated as shown in Equations 3-2 and 3-3, respectively.

$$\varepsilon = (L - L_0)/L_0, \qquad\qquad\qquad\qquad\qquad \text{Equation 3-2}$$

$$\gamma = (0.5 \, d \, \theta)/L, \qquad\qquad\qquad\qquad\qquad \text{Equation 3-3}$$

Here, L is the current distance between top and bottom sections, L_0 is the initial distance between top and bottom sections, γ is the engineering shear strain, and θ is the relative rotation between top and bottom sections.

One of the advantages of having the additional data from DIC is that all of the information necessary to consider netting theory (detailed in the following section) in terms of an orthotropic laminate is available for every stage in the project: inflation pressure, tube diameter, longitudinal strain, in-plane shear strain, longitudinal stress, hoop stress, and longitudinal reaction. All of this information is necessary in order to determine how much longitudinal stress is due to material behavior versus netting theory effects and pressure variation. The data presented later in this paper takes into account netting theory as well as pressure fluctuations.

3.4.1   Assessment of Results in Light of Netting Theory

Netting theory, which relies on simple stress transformations, assumes that all hoop stresses in inflatable braided cylindrical pressure vessels are carried by the braid fibers in tension (Evans and Gibson 2002). Therefore, if there is no longitudinal reinforcement, a pressurized cylinder of any braid angle will expand or contract longitudinally until the braid angle is approximately 54.7° in order to satisfy equilibrium in both the longitudinal and hoop directions. Equation 3-4 gives the longitudinal restraining force, R_{net}, predicted by netting theory that is required to prevent expansion or contraction of an inflated, braided tube as a function of inflation pressure, p, tube radius, r, and braid angle (Evans and Gibson 2002). The approximate angle of

54.7° corresponds to $R_{net} = 0$. In the testing described here, the tension-torsion machine itself provides the restraining force; in an inflated structural member, integral axial restraining cords or secondary longitudinal reinforcement provide the restraining force.

$$R_{net} = p\pi r^2(1 - 2cot^2\beta) \hspace{4cm} \text{Equation 3-4}$$

To assess the efficacy of netting theory, the load measured by the load cell is compared to the load predicted by netting theory as a function of inflation pressure in Figure 3-4. The reaction predicted by netting theory is based on the measured tube radius and braid angle derived from the test data, so this predicted reaction does not vary linearly with inflation pressure. However, the agreement between theory (Equation 3-4) and experiment is very good, especially at the higher braid angles that are of primary interest. In particular, we note that netting theory predicts that the reaction will be close to zero for the 55° nominal braid angle test articles and measurements agree. These results clearly show that any longitudinal reinforcement in a braided tubular member will not be pre-tensioned by inflation if the braid angle is close to 54.7°, and that increasing braid angles will significantly increase longitudinal reinforcement effectiveness.
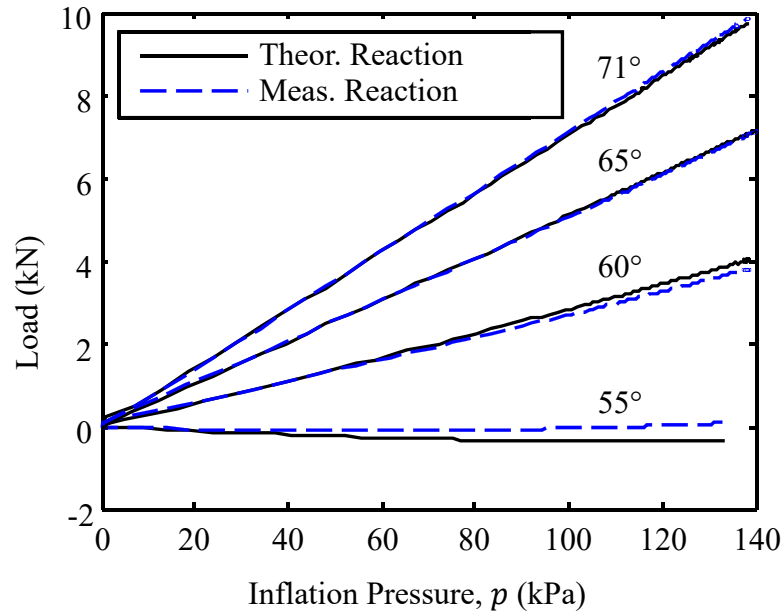
Figure 3-4. Comparison of measured reaction forces and predictions per netting theory.

3.4.2 Tension-Torsion Results

Similar to previous studies (Brayley et al. 2012; Hutchings and Braun, 2009; Colman et al. 2014), it was found that the effective stress-strain relationships for both the axial load case and the torsional load case were generally linear as shown in Figure 3-5 and Figure 3-6, respectively, for representative tests at the 138 kPa pressure level. Although not shown, this was also true at the lower inflation pressures considered in this study. It is noted that the magnitude of longitudinal strain is at least an order of magnitude greater than the shear strain. There is some hysteresis as evidenced by the slightly open loop. The moduli were taken as the slope of a linear fit through all of the data in a given loop. Both the loading and unloading data were used because the objective was to determine a single modulus value for a given braid angle and inflation pressure. The tests were initiated at the target braid angle, but the braid angle changed slightly during the test, so it was necessary to go in both directions to bound the angle of interest. Further, the slope of the loading-only data is very similar to the slope of all the data. A value was

computed for each of the three runs. The values were very repeatable for a single specimen (< 1-2% coefficient of variation (CoV) for longitudinal modulus and < 2-3% CoV for shear modulus).
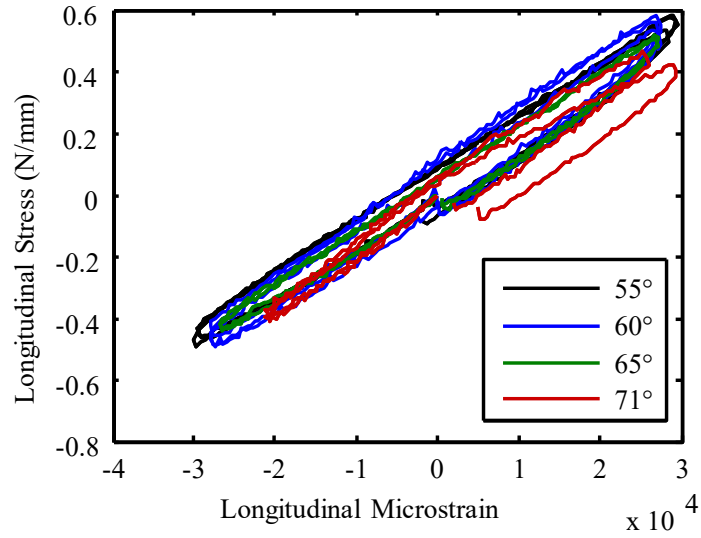
Figure 3-4. Representative total longitudinal stress-strain results.
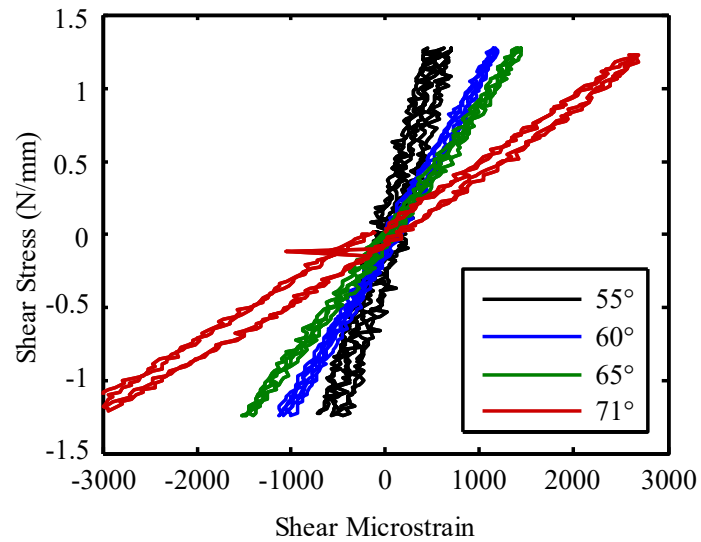
Figure 3-5. Representative shear stress-strain results.

The primary results of interest derived from the tension-torsion tests described here are the braided tube in-plane shear modulus G_{LH} and longitudinal modulus E_L values that vary as a function of braid angle and inflation pressure. The E_L and G_{LH} results are given in Figure 3-7 and Figure 3-8 (individual specimens with solid lines connecting mean values for each braid angle and pressure) and Table 3-2 and Table 3-3 (average values and coefficients of variation), respectively.
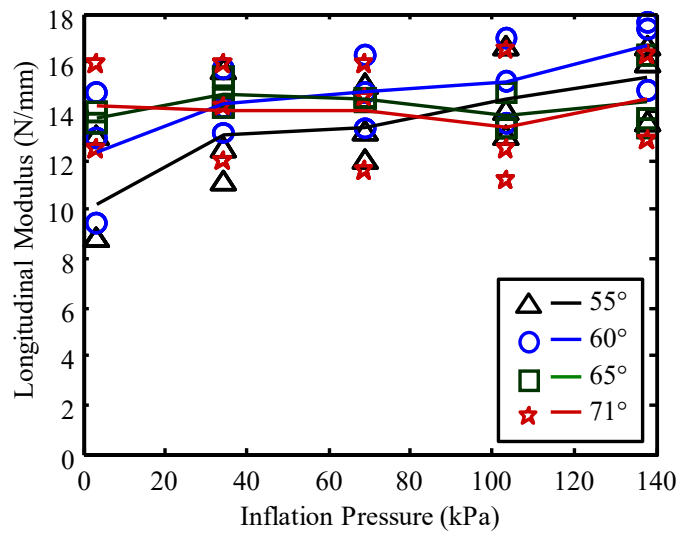
Figure 3-6. Longitudinal modulus E_L as a function of inflation pressure and braid angle (symbols are individual specimens and lines are averages).
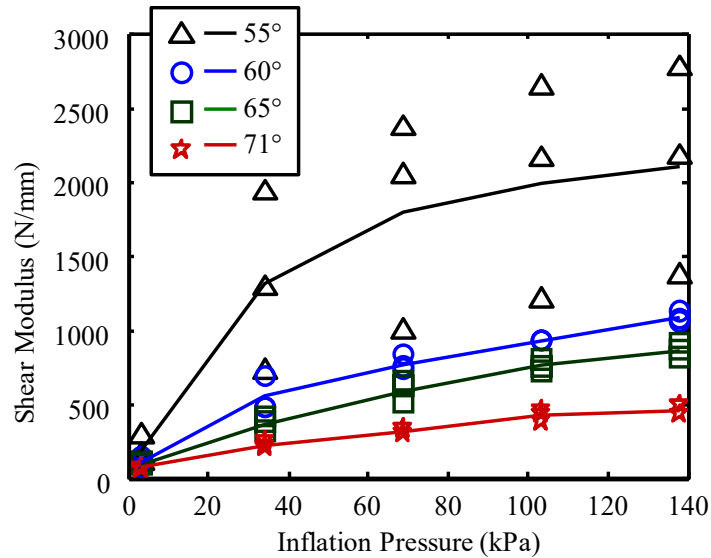
Figure 3-7. Shear modulus G_{LH} as a function of inflation pressure and braid angle (symbols are individual specimens and lines are averages).

The G_{LH} results show a clear effect of both inflation pressure and braid angle. Higher inflation pressure results in higher shear stiffness. Smaller braid angles over the range investigated here result in stiffer response, since the fiber tows are better oriented for directly resisting shear as the braid angle decreases. The G_{LH} results for the 55° braid were highly variable. This is believed to be due to misalignments or non-uniform clamping of the specimens during installation. The effective longitudinal braid stress is highest for 55° braid angle tubes (reaction force is approximately zero), which likely exacerbated issues with misalignment and/or non-uniform clamping at the ends of the specimens. Additional testing would be needed in order to generate more reliable results for this braid angle, though it is noted that braided, reinforced tubes with a braid angle close to 54.7° have little value for structural applications since the longitudinal reinforcing elements would not be appreciably tensioned during inflation. For larger braid angles, the variability is less, and decreases with inflation pressure. It is important to note that with respect to HIAD structures in which the braided tubes are used, the primary results of

44

interest are for nominal braid angles of 65° and 71° and pressures of 69kPa and higher, for which

the coefficient of variation (CoV) in G_{LH} was 13% or less.

The E_L results are somewhat mixed, although this is not surprising since the stiffness is

small and the braid angle is only one of many factors affecting the stiffness. Several factors

could be contributing to this such as nylon hot melt stiffness, polyurethane coating stiffness, and

inter-tow friction. There does appear to be a slight increase in E_L with inflation pressure as would

be expected.

Table 3-2. Average measured longitudinal modulus (N/mm) as a function of nominal braid angle and pressure.

Nominal Braid Angle	Inflation Pressure (kPa)				
	3	34	69	103	138
55°	10 (24%)	13 (18%)	13 (12%)	15 (13%)	15 (11%)
60°	12 (22%)	14 (9%)	15 (10%)	15 (11%)	17 (9%)
65°	14 (2%)	15 (5%)	14 (1%)	14 (6%)	14 (12%)
71°	14 (18%)	14 (15%)	14 (16%)	13 (20%)	14 (17%)

Table 3-3. Average measured shear modulus (N/mm) as a function of nominal braid angle and pressure.

Nominal	Inflation Pressure (kPa)				
Braid Angle	3	34	69	103	138
55°	180 (53%)	1310 (46%)	1800 (40%)	2000 (37%)	2100 (33%)
60°	104 (31%)	549 (22%)	773 (6%)	931 (0.3%)	1090 (3%)
65°	96 (19%)	363 (14%)	594 (13%)	759 (6%)	865 (6%)
71°	68 (27%)	224 (13%)	320 (5%)	420 (11%)	468 (9%)

The longitudinal stiffness of the gas bladder was found to be 9.6 N/mm and 8.8 N/mm based on the bladder uni-axial tension testing of 25 mm wide strips of the bladder and full inflated bladder tension testing (same protocol as the braided tubes, but without the braid), respectively. The CoV for the five coupons was only 2%. Poisson's ratio was calculated as approximately 0.44 based on the relative strain ratio determined from DIC data, assuming the bladder to be an isotropic, elastic material. The CoV in modulus for the inflated gas bladder could not be determined because only one inflated bladder specimen was tested. The shear modulus of the bladder was found to be only about 3.3 N/mm using data from both tests, which is much less than the values measured for the braid. It was found that the gas bladder contributes more to the total longitudinal stiffness than the bias braid, whereas the bladder has a very small effect on G_{LH} values.

Because the longitudinal stiffness of the gas bladder was found to be significant, its stiffness should be removed from the E_L results determined from the tension-torsion tests if the two materials are considered separately in a mechanics-based model of an inflated, braided structure.

3.4.3   Discussion of DIC Observations

One notable observation from DIC data was that the shear stiffness calculated using Equation 3-3 was sometimes in poor agreement with the shear stiffness calculated using DIC shear strains averaged over the surface of the tube. This discrepancy was the motivation for the following mathematical discussion compiled by Dr. Andrew Goupee.

Figure 3-10 shows the significant spatial variability of shear strain for a typical test. From left to right in Figure 3-10, it appears that there are distinct regions that alternate between relatively high and relatively low strain values. These regions correspond to the geometric positions of the longitudinal nylon hot melts, which are not intended to be structural, but do seem to affect the spatial distribution of shear strain. Based on this observation, the following analysis was performed to assess whether the stiffness discrepancy noted above could be explained and ultimately justify the calculations of shear strain according to Equation 3-3.
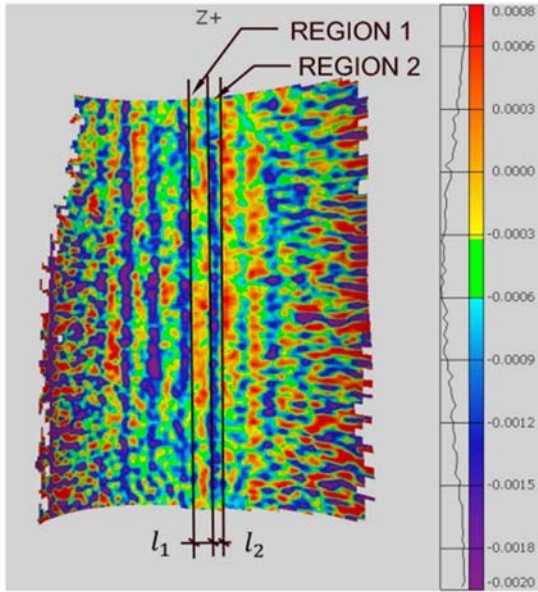
Figure 3-8. Spatial variability of shear strain, γ, during torsion test.

It is difficult to accurately estimate surface averages based only on visual inspection of the DIC data given in Figure 3-9. Volumetric averaging was not possible due to the lack of thickness information. For the sake of discussion, the following rough approximations in Equation 3-5 and Equation 3-6 were adopted:

$$2\gamma_1 \cong \gamma_2 \qquad\qquad\qquad \text{Equation 3-5}$$

and

$$l_1 \cong 2l_2. \qquad\qquad\qquad \text{Equation 3-6}$$

In Equation 3-5 and Equation 3-6, γ is the in-plane shear strain, l is the width of a region in the circumferential direction and the subscript denotes the region number as shown in Figure 3-10. The difference in shear strain due to a given shear load implies that the shear moduli of the bands are related as

$$G_1 \cong 2G_2.$$

<div align="right">Equation 3-7</div>

If each band is treated as a spring, the effective shear spring constant of a band K is proportional to the ratio of G to l, i.e.

$$K \propto \frac{G}{l}.$$

<div align="right">Equation 3-8</div>

Using Equation 3-6 through Equation 3-8, and ignoring the approximate nature of these relationships, the surface-averaged spring stiffness value K^V for the system can be expressed in terms of G_1 and l_1 as follows:

$$K^V = \frac{K_1 l_1 + K_2 l_2}{l_1 + l_2} = \frac{\left(\frac{G_1}{l_1}\right)l_1 + \left(\frac{G_2}{l_2}\right)l_2}{l_1 + l_2} = \frac{G_1 + \frac{G_1}{2}}{l_1 + \frac{l_1}{2}} = \frac{G_1}{l_1}.$$

<div align="right">Equation 3-9</div>

K^V can also expressed in terms of an equivalent total shear stiffness G_{eq}^V,

$$K^V = \frac{G_{eq}^V}{l_1 + l_2} = \frac{G_{eq}^V}{l_1 + \frac{l_1}{2}} = \frac{2G_{eq}^V}{3l_1}.$$

<div align="right">Equation 3-10</div>

Equating Equation 3-9 and Equation 3-10 permits an expression of G_{eq}^V in terms of G_1 of the form

$$G_{eq}^V = \frac{3G_1}{2}.$$

<div align="right">Equation 3-11</div>

However, the observed regionalized deformation pattern of Figure 3-9 indicates that the equivalent shear modulus may more closely agree with a calculation following a springs-in-series format. As was performed for K^V, the equivalent springs-in-series stiffness K^s can be expressed as a function of G_1 and l_1. Performing the mathematical manipulations yields

$$\frac{1}{K^s} = \frac{1}{K_1} + \frac{1}{K_2} = \frac{l_1}{G_1} + \frac{l_2}{G_2} = \frac{l_1}{G_1} + \frac{2l_1}{2G_2} = \frac{2l_1}{G_1}.$$

<div align="right">Equation 3-12</div>

Expressing K^s as a function of an effective shear modulus G^s_{eq} gives

$$\frac{1}{K^s} = \frac{l_1+l_2}{G^s_{eq}} = \frac{l_1+\frac{l_1}{2}}{G^s_{eq}} = \frac{3l_1}{2G^s_{eq}}.$$

<div align="right">Equation 3-13</div>

Combining Equation 3-12 and Equation 3-13, the relationship between G^s_{eq} and G_1 is shown to be

$$G^s_{eq} = \frac{3G_1}{4}.$$

<div align="right">Equation 3-14</div>

Through comparison of Equation 3-10 and Equation 3-14, this simple analysis estimates that the effective shear modulus G^s_{eq} derived from the springs-in-series approach is one half of the surface-averaged effective shear modulus value G^V_{eq}. This implies that the strain computed from Equation 3-3 could be roughly twice the value computed based on surface-averaging using DIC data for the specimen of Figure 3-10.

Using the specimen strains shown in Figure 3-10, the ratio of the shear strain computed from surface averaging to the shear strain calculated via Equation 3-3 was 1.75, which is similar to the above analysis using rough visual estimates for G and L ratios. However, mixed results were observed for this ratio. The surface averaging method sometimes resulted in a larger shear strain and other times resulted in a smaller shear strain than one computed using Equation 3-3. This illustrates the importance of using appropriate methods for measuring strains and calculating effective mechanical properties from experimental data if that is what is of interest. It also shows that the reading from a mechanical measuring device may be highly dependent on the location where it is installed on the test article.

This discrepancy in average strain and that computed using Eq. 3-3 may appear to be at odds with the accepted approach of volumetric averaging commonly used in homogenization techniques (Ghosh et al. 1996; Terada et al. 20002; and Gonzalez et al. 2004). However, such homogenization techniques are applied to known volumes of continua. In contrast, the braid volume is not precisely known due to significant local thickness variations. Further, the braid is not a continuum, and behaves as a mechanism.

Conversely, visual inspection of the longitudinal strain field shows a very uniform distribution. The longitudinal strain calculated using surface-averaging methods was always in very good agreement (i.e. < 1% difference) with the strain calculated via Equation 3-2.

3.5 *Lamina Properties from Test Data*

The key lamina properties for input to finite-element models of both straight beams and torus structural elements were successfully derived from the experimental results presented here (Clapp et al. 2016a; Young 2017). The models were shown to be in good agreement with experiments for both straight beams (Clapp et al. 2016b) and torus structures (Young et al. 2017; Young 2017).

3.6 *Fiber Tow Testing*

As was shown in Clapp et al. (2016a) and Young (2017), the effective stiffness of the braid in the direction of the fibers E_1 can be back-calculated from the tension-torsion test data. It was found, not surprisingly, that this effective stiffness in the braid fiber direction increases with

inflation pressure. Further, it appears that E_1 may be converging towards a constant value that may have an upper bound equal to the stiffness of straight fibers. Thus, uniaxial tension testing of individual uncoated fiber tows was performed in order to quantify the stiffness of straight fiber tows without a confining normal stress due to internal inflation pressure. This stiffness was then compared to the effective stiffness back-calculated from the tension-torsion test data. The straight fiber stiffness should be an upper bound for E_1, since the braid tows are expected to exhibit progressively greater de-crimping with increasing inflation pressure, reducing second-order geometric effects and increasing their effective axial stiffness.

Fiber tow bundles approximately 250 mm long were carefully extracted from the raw braided sleeving. Figure 3-10 shows a close-up photo of dry fiber tow bundles from a 71° braid (not necessarily at 71° in the photo). Each fiber tow was weighed and the length was measured. About 15 mm of length on each end of the fiber tow was coated with high-strength epoxy to lock the individual fibers together and allow the tension test machine grips to transfer load to all fibers as uniformly as possible. An Instron Model 5966 Universal Testing Machine with 10 kN capacity was used to load the fiber tows at a displacement rate of 10 mm/min. An extensometer with 50 mm gage length was used to monitor tensile extension in the mid-height region of each fiber tow (Figure 3-11). The gage was held in place with wire so its weight would not be applied to the fibers. Ten fiber tows at each braid angle were tested. Due to unequal load sharing among individual fibers within the tow, there was generally a soft region in the load-strain data at low loads, then a nearly linear region as all fibers engaged which typically ranged from 40% to 80% of peak load, and finally another soft region closer to peak load as individual fibers in the group started to fail.
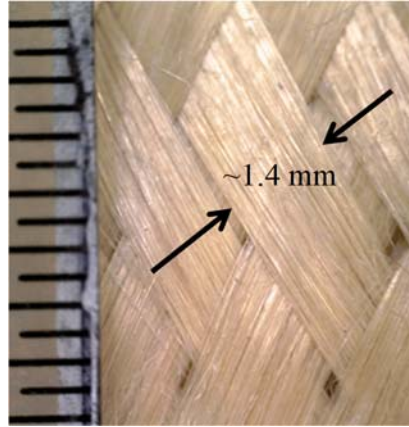
Figure 3-9. Close-up photo of 71° fiber tow bundles (image credit Andrew Young).

Figure 3-10. Photo of fiber tow uniaxial tension test specimen with extensometer attached.

If the response was linear between 40-80% of peak load, all data within this range was used to calculate a best-fit slope which was used to compute the tow modulus. For some specimens, the limits of the range were manually adjusted to omit nonlinear regions. Several of the load-strain data sets (two to four per set of 10 at each braid angle) had no clear linear region; it was not possible to accurately estimate the stiffness from these data sets, and the tow modulus was not calculated for these tows. Representative valid and invalid tests are shown in Figure 3-12

along with the limits of the 40-80% range for the valid test.
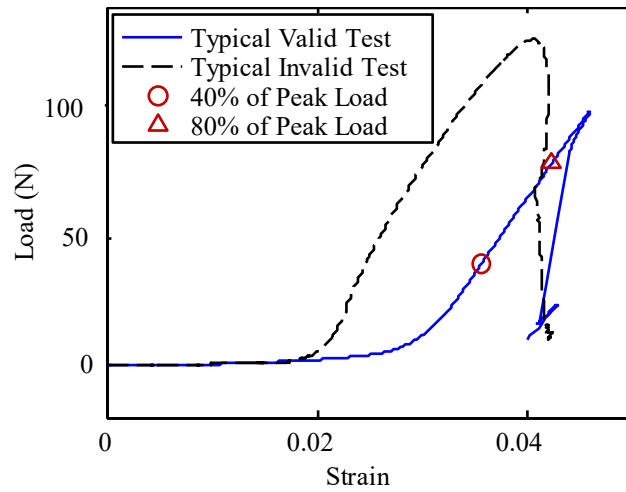
Figure 3-11. Typical valid and invalid (i.e. non-linear) fiber tow load-strain curves.

The key results of the fiber tow testing are summarized in Table 3-5. The nominal braid angle and tube diameter corresponding to each tow was used to calculate the theoretical nominal tow width w_t assuming 100% coverage per Equation 3-15, where n_{tows} is the total number of fiber tows making up the braid and the factor of one half accounts for the overlap of fibers running in alternating $\pm \beta$ directions.

Table 3-4. Summary of individual fiber tow test results.

Nominal Braid Angle	#	Nominal Tow Width w_t (mm)	EA (kN)	E_{1t}, (kN/mm)	Unit Weight (N/mm)		$\dfrac{EA}{\Gamma_t}$ (m)
					Tow Direction Γ_t	Longitudinal Direction Γ_L	
55°	8	2.49	9.94	3.99	$2.05 \cdot 10^{-6}$	$3.57 \cdot 10^{-6}$	$4.85 \cdot 10^6$
60°	6	2.17	8.28	3.81	$1.75 \cdot 10^{-6}$	$3.49 \cdot 10^{-6}$	$4.74 \cdot 10^6$
65°	7	1.83	7.33	3.99	$1.46 \cdot 10^{-6}$	$3.46 \cdot 10^{-6}$	$5.02 \cdot 10^6$
71°	6	1.41	5.37	3.80	$1.10 \cdot 10^{-6}$	$3.37 \cdot 10^{-6}$	$4.89 \cdot 10^6$
Average	--	--	--	3.90	--	$3.47 \cdot 10^{-6}$	$4.88 \cdot 10^6$
Coefficient of Variation	--	--	--	2.8%	--	2.4%	2.4%

$$w_t = \frac{\pi d}{\frac{1}{2}n_{tows}\cos(\beta)}$$

Equation 3-15

The tow longitudinal rigidity, EA, was taken as the average slope of the linear region of the load-strain curve. The modulus per calculated nominal width, E_1, was found to be in good agreement for all braid angles with a coefficient of variation (CoV) of only 2.8%. The unit weight of the fibers in the tow direction γ_t was also measured and used to compute a normalized longitudinal rigidity of $4.88 \cdot 10^6$ m, which was about 5% less than the value of $5.14 \cdot 10^6$ m calculated using published Technora (Teijin 2016) stiffness and density values reported in Miracle and Donaldson (2001). The normalized longitudinal rigidity was also found to have low variability with a CoV of 2.4%. The unit weight of the fibers transformed to the longitudinal direction γ_L is also shown and the CoV is low indicating that the aerial weight of all braided tubes is about the same for all braid angles.

The measured individual moduli per unit width, E_1, are directly comparable to the effective tow moduli per unit width back-calculated in Clapp et al. (2016a) and Young (2017)

from the tension-torsion test results using classical lamination theory. For all braid angles, the

measured E_1 is greater than the values back-calculated for braid angles of 60° through 71°. The

ratio of back-calculated E_1 from tension-torsion testing to individual fiber tow E_1 as a function of

inflation pressure is shown with symbols in Figure 3-13. This appears to support the previously

stated hypothesis that the individual fiber tow modulus E_1 is an upper bound on the effective

modulus that can be achieved by increasing inflation pressure.
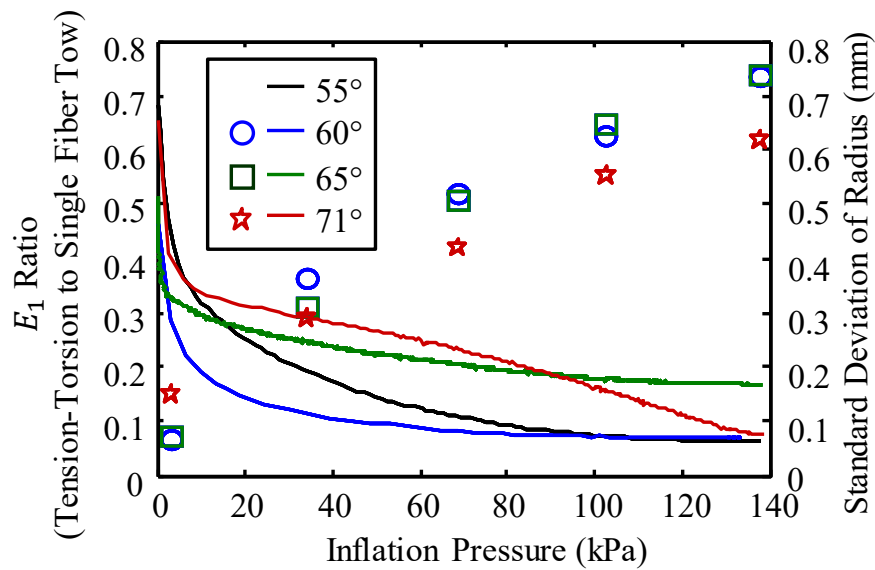
Figure 3-12. Fiber tow decrimping (lines) and stiffening (symbols) with increasing inflation pressure.

3.7 Fiber Tow De-Crimping

One explanation for the observed increase in braid stiffness with inflation pressure is

fiber tow de-crimping and inter-tow friction (Turner et al. 2008; Brayley et al. 2012; Kabche et

al. 2011). A study was performed using DIC data to experimentally investigate if the effect of

fiber tow de-crimping could be captured quantitatively, defined here as fiber tow straightening

and becoming more uniformly aligned with the tow direction, thereby increasing stiffness. The

DIC system described earlier was used with 50 mm focal length lenses to observe a relatively

small area on the tension-torsion specimens sized at about 75 by 50 mm as shown Figure 3-14.
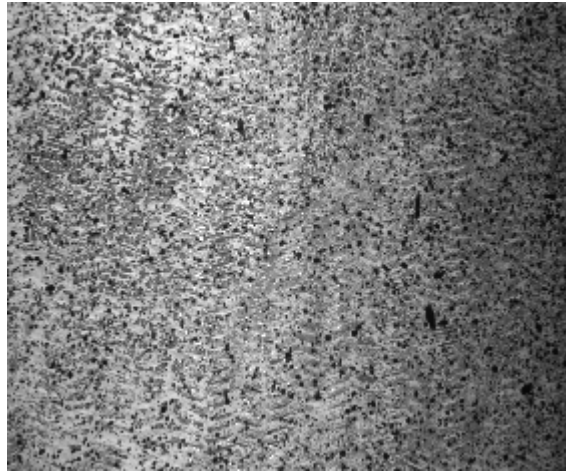
Figure 3-13. Photo of 75 mm by 50 mm field of view in surface flattening investigation.

Images were collected as the tubes were inflated. The data were transformed to align with

the cylinder axis as previously described. All data points (~20,000) would have the same radius

if it was a perfect cylinder. However, the cylinder is not perfect and one of the reasons for this is

waviness of the braid. One way to quantify the waviness of the braid using the DIC data is to

examine the standard deviation of the radius of all data points as a function of inflation pressure.

The data from one specimen of each braid angle is shown by the smooth curves in Figure 3-13,

clearly demonstrating that the standard deviation of radius decreases with increasing pressures

for all braid angles. These data support the hypothesis that fiber tow de-crimping is an important

driver of the observed increase in fabric shear modulus with increasing inflation pressure.

3.8   Summary

Several different experiments were performed in an effort to quantify the effective elastic stiffness properties of relatively large inflatable braided tubes fabricated from Technora fiber tows. Tension and torsion experiments were successfully performed on full-scale, inflated, braided fabric tubes of four different braid angles and at five different levels of inflation pressure. The fabric shear stiffness was found to be highly dependent on both braid angle and inflation pressure. The fabric longitudinal stiffness was found to be quite small relative to the shear stiffness, and it was not possible to clearly discern the effects of braid angle on longitudinal stiffness. Independent testing of the urethane gas bladder material revealed that it provides most of the longitudinal stiffness of the inflated, braided tubes, but contributes very little shear stiffness.

The digital image correlation data revealed spatial variation of shear strain that was important to consider when computing the gross engineering shear stiffness. Digital image correlation data also captured the braid surface flattening with increasing inflation pressure, which is consistent with increasing fiber de-crimping with increasing inflation pressure.

The effective modulus of the fiber tows in the inflatable tubes was seen to increase with pressure, which is attributed to de-crimping and increasing inter-tow friction with increasing inflation pressure. Independent testing of individual fiber tows extracted from uncoated braid material was also performed. The straight tow modulus observed from these tests agreed well with the published stiffness of Technora, and proved to be an upper bound on the effective tow modulus back-calculated from the tension-torsion tests.

Suggested future studies could include performing tension-torsion testing with alternate braid geometries and materials. Additional data may shed more light on the feasibility of establishing methods of estimating the stiffness of inflatable braided structures given braid angle, straight fiber tow stiffness, and inflation pressure. The response predicted by finite-element models that used the parameters reported here to define the tube shell properties were shown to agree well with the measured tension response of the inflated tubes reported in this chapter (Clapp et al. 2016a), measured beam bending response (Clapp et al. 2016b) and torus compression with combined in-plane and out-of-plane loading response (Young et al. 2017). Additional validation with alternate materials/geometries would further increase confidence that the properties are reasonable.

4   BENDING RESPONSE OF REINFORCED, INFLATED, TUBULAR, BRAIDED FABRIC STRUCTURAL MEMBERS

Reinforced, inflatable, braided tubular members are seeing increased use in structural applications where low mass and storage volume are critical such as the NASA HIAD project. However, research on the structural behavior of these members has been limited.

This Chapter focuses on the portion of the HIAD research that aims to improve the understanding of the structural behavior of these members via the experiments reported here and numerical models reported in Clapp et al. (2016b) and (Young et al. 2017). Eight tubes with braided fabric shells of varying bias angles and integral reinforcing cords were subjected to flexural tests with highly controlled loading and boundary conditions. Three-dimensional shell-based finite-element models relying on independently measured material properties reported in Chapter 3 were developed as described in Clapp et al. (2016b) and (Young et al. 2017) and were shown to agree very well with the experimental results.

Understanding the structural behavior of inflatable, reinforced, braided fabric tubular members is critical because full-scale HIAD experiments with realistic loading conditions are highly cost prohibitive. In fact, it is essentially impossible to simulate all Mars entry conditions without going to Mars. Instead, reliable predictive tools are needed that can be validated with a limited set of very reliable experimental data. Extensive ground based experimental efforts led by NASA have been conducted to characterize the structural behavior of the 6m diameter HIAD. These experiments have included a wide range of structural configurations and loading scenarios including full-scale complete HIAD quasi-static testing using vacuum pressure (Swanson et al. 2014; Swanson et al. 2015), full-scale complete HIAD wind tunnel testing (Cassell et al. 2013; Kazemba et al. 2013; Li, Braun, & Cassell, 2014; Swanson et al. 2013), full-scale complete

HIAD modal testing (Abraham et al. 2014), and HIAD individual torus compression and compression/torsion testing (Chen & Moholt, 2014). All of these experiments have provided useful information, but were relatively complex in terms of loading and boundary conditions, so they were not ideal to serve as simple model validation cases.

4.1 Background

A large number of studies have addressed the bending performance of inflated, woven fabric tubes (Turner et al. 2008; Leonard et al. 1960; Steeves, 1975; Steeves, 1978; Webber, 1982; Wicker, 1993; Main et al. 1994; Main et al. 1995; Wielgosz & Thomas, 2002; Cavallaro et al. 2003; Thomas & Wielgosz, 2004; Davids et al. 2007; Davids & Zhang, 2008; Zhu et al. 2008; Davids, 2009; Malm et al. 2009; Apedo et al. 2010; Luchsinger et al. 2011). Some studies have focused on the effects of fabric wrinkling, or loss of pretension due to load-induced stresses/strains and included experiments as well as models based on beam bending theory (Veldman et al. 2005a&b; Steeves, 1975; Main et al. 1994; Davids & Zhang, 2008; Apedo et al. 2010). Other researchers have examined the bending response of woven/braided tubes using 3D finite-element (FE) simulations which relied on shell or membrane elements (Malm et al. 2009; Apedo et al. 2010; Luchsinger et al. 2011; Thomas & Le van, 2013; Luchsinger & Galliot, 2013; Barsotti & Ligaro, 2014; Elsabbagh, 2015; Nguyen et al. 2015; Guo et al. 2016; Veldman, 2006). Several studies have considered the experimental determination of fabric constitutive properties accounting for the effect of internal inflation pressure (Turner et al. 2008; Steeves, 1975; Main et al. 1995; Malm et al. 2009; Kabche et al. 2011; Veldman, 2005b; Clapp et al. 2016), while others assessed the response of inflated, woven fabric arches subjected to in-plane loads (Steeves, 1978; Davids, 2009; Guo et al. 2016).

61

Relatively few researchers have explicitly studied the bending response of inflated, braided fabric tubes. Brown et al. (2001) reported limited bending test results of a deployable wing with structural capacity provided by a reinforced, braided spar inflated to three different pressures. Veldman et al. (2005a) performed bending tests on 200 mm diameter triaxial braided tubes with axial fibers inflated to pressures up to 30 kPa. Brayley et al. (2012) performed bending tests on 254 mm diameter braided tubes inflated to pressures up to 345 kPa; both straight tubes and arches were tested. Brayley et al. (2012) also reported the results of their beam-element 2D FE models, which conservatively neglected the stiffness of the braided shell and only considered the longitudinal stiffness of the reinforcing straps. The models were shown to be in reasonable agreement with experiments when the reinforcing straps were given a small compressive stiffness and capacity.

The research presented in this chapter is expected to add significantly to the body of literature on the response of braided, inflated members. The first objective of this investigation was to conduct quasi-static bend testing of straight tubes with highly controlled loading and simply supported boundary conditions. These highly controlled conditions allow direct comparisons to be made between experimental and model data with low probability of overlooking important physical phenomena. The articles tested here were straight, but otherwise identical in materials and construction to the tori in the aforementioned HIAD test articles. All test articles used in the previously mentioned NASA efforts and the work described here were constructed by Airborne Systems of Santa Ana, CA, USA. Full-scale (for a 6 m diameter HIAD) straight tubes with five different braid angles (nominally four different braid angles, but five were achieved based on as-built measurements) were tested over a range of inflation pressures. Digital Image Correlation (DIC) was used to examine the spatial variability of response

parameters throughout testing. Two pairs of cameras were used so that two cords could be monitored simultaneously: one cord subject to tension from bending and the other subject to compression from bending.

The second objective of work described in this chapter was to generate data to validate the finite-element models that used only the independently determined constitutive properties of the individual components that make up the HIAD inflatable structural members, including the braided fabric shell, internal impermeable gas bladder, and reinforcing cords.

The third objective of this work was to develop 3D shell-based FE models of the straight beam experiments, which is documented in Clapp et al. (2016b) and Young (2017). The FE models were found to agree quite well with the experiments.

4.2   Description of Test Articles

Eight straight cylindrical tube specimens were provided to the University of Maine by NASA Langley Research Center. A photograph of one specimen with a schematic image showing the tube components is given in Figure 4-1.
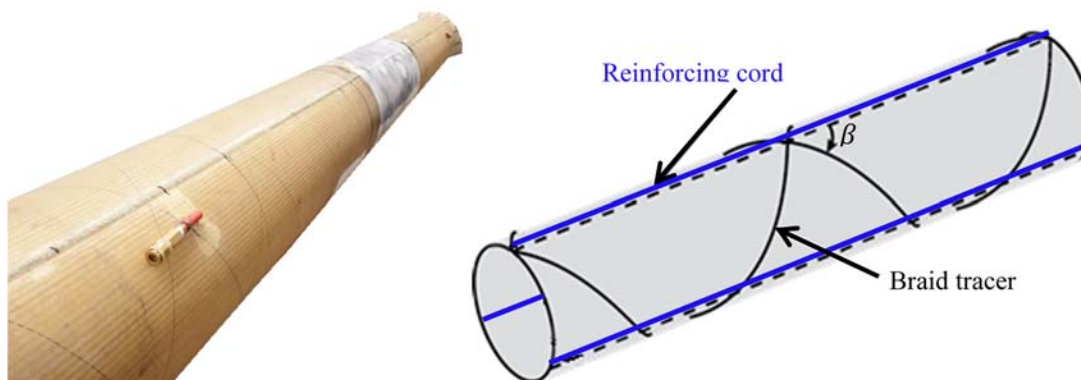
Figure 4-1. Photo of straight test tube article (left) and sketch of reinforced, braided tube components.

The overall length of each inflated tube was about 4.5 m. All tubes were constructed with an impermeable urethane gas bladder, braided sleeving, and reinforcing cords. The braided sleeving and reinforcing cords were both constructed with Technora fibers (Teijin, 2016). The sleeving was braided at four different nominal angles relative to the longitudinal direction (two specimens at each angle): 55°, 60°, 65°, and 71° at the nominal diameter of 345 mm. The as-built braid angles and diameters for each inflation pressure are summarized in Table 4-1. One nominal 55° tube had an as-built braid angle closer to 57°. Throughout this paper the test articles will be identified based on their nominal braid angles except the previously mentioned tube, which will be identified as the 57° tube. This range of braid angles allowed the effect of this important parameter on bending response to be assessed. The properties of the braided sleeving and gas bladder materials were determined via tension and torsion testing as detailed in Chapter 3.

Table 4-1. Summary of as-built test article dimensions.

Tube	Pressure (kPa)	Braid Angle (°)	Diameter (mm)
55°	34	55.79	345
	69	55.77	345
	103	55.83	346
	138	55.85	346
57°	34	57.07	351
	69	57.07	351
	103	57.09	351
	138	57.12	352
60°	34	60.00	342
	69	59.97	342
	103	59.95	342
	138	59.97	342
65°	34	64.59	338
	69	64.57	338
	103	64.57	339
	138	64.55	339
71°	34	70.61	338
	69	70.59	338
	103	70.57	339
	138	70.56	340

Each specimen was constructed with three braided Technora (Teijin, 2016) reinforcing cords. The cords were integrated within the braided shell at evenly spaced increments of 120° around the cross-section. This cord geometry allowed the specimens to be tested in two different orientations referred to as "one-cord up" (one cord at the apex of the cross-section) and "two-cords up" (one cord at bottom of the cross-section). Under downward loading of the simply supported tube, the one-cord up configuration places one cord in compression and two cords in tension and the two-cords up configuration places two cords in compression and one cord in tension. It is not possible for the cords to move relative to each other around the cross-section since they are integrated within the braid, but some specimens did exhibit a slight twist over the length of the tube (i.e. the cord axis was slightly misaligned with tube axis). In this instance, the cord was positioned so that it was at the top or bottom of the cross-section at mid-span.

The five different braid angles and two different cord configurations allowed ten different tube cross-sectional geometries to be tested. It was found that articles of the same braid angle performed very similarly, so results from only one of two nominally identical specimens are shown. An exception is that the results are shown for both nominal 55° tubes due to the aforementioned differences in as-built dimensions.

4.3 Test Setup

Figure 4-2 shows a bending specimen in the test setup. Tube end supports consisted of wood saddles lined with rubber that were constructed to match the nominal diameter of the test articles and support the ends of the tubes. The saddles were 150 mm wide in the longitudinal direction. Straps attached to the wood saddles were placed relatively loosely over the top of the tube on each end to prevent the saddles from tipping. Steel casters were attached to the bottoms

of the wood saddles to serve as roller supports with centers of rotation 350 mm below the

nominal mid-height of the tubes. Both roller end supports rested on concrete blocks that were

topped with carefully leveled smooth steel plates to minimize rolling resistance. The span from

center-to-center of rollers was 3.28 m. Loads were applied via an electric screw-jack with forces

distributed through a wood spreader beam. A pair of 50 mm wide load straps transferred forces

to the test article. The straps were centered on the tubes and were separated by a distance of 1.04

m center-to-center in the longitudinal direction. The transverse width of the spreader beam was

sized to match the tube diameter so the straps would be pulled straight down. The ends of the

load straps were fitted with grommets loosely attached to the wood spreader beam to permit free

rotation and release film was placed between the straps and the test article to minimize friction.

Figure 4-2. Photo of bending test setup.

4.3.1 Instrumentation

Applied force was monitored with an Omega LC701-2K inline load cell located just below the spreader beam. It was balanced in this configuration with no straps in contact with the tubes. Nine Celesco SP-25 string potentiometers were used to monitor vertical deflections as loads were applied. The string potentiometers were symmetrically placed at the following distances from mid-span: 0, 230, 460, 920, and 1380 mm. Digital image correlation data were also collected near mid-span using two pairs of 5 megapixel cameras. The internal inflation pressure was monitored with a Setra 206 pressure transducer with a 0 – 345 kPa range. The tubes did not leak appreciably over the relatively short time duration over which a test was performed, so the air supply line was removed and each tube was tested as a sealed pressure vessel.

4.3.2 Procedure

All specimens were loaded until the deflection at mid-span was at least 100mm, which was more than sufficient to cause loss of top cord pretension (i.e. wrinkling). Three sets of nominally identical tests were performed at four different inflation pressures in the following order: (3) cycles at 103 kPa, (3) cycles at 34 kPa, (3) cycles at 69 kPa, and (3) cycles at 138 kPa. Typically, the structure was softer on the first cycle and then stiffened with subsequent load cycling.

4.4 Tube Load-Deflection Response

Tube mid-span load-displacement response is shown in Figure 4-3 through Figure 4-7 for tube braid angles of 55°, 57, 60°, 65°, and 71°, respectively along with model results that are briefly discussed later in section 4.6. These figures clearly show the dramatic increase in capacity with increasing braid angle and inflation pressure. This result can be explained by considering

68

netting theory (Veldman, 2006; Clapp et al. 2016; Evans & Gibson, 2002). Equation 2-1 gives the longitudinal restraining force, R_{net}, predicted by netting theory that is required to prevent expansion or contraction of an inflated, braided tube as a function of inflation pressure, p, tube radius, r, and braid angle, β, (Clapp et al. 2016). In the inflated tubes of this study, the restraining force is provided by the reinforcing cords, so R_{net} is the total pretension that is carried by the three reinforcing cords (noting that the internal bladder may carry a small portion of this load as well).

The approximate angle of 54.7° corresponds to $R_{net} = 0$, and therefore at this bias angle, the tube would have little bending stiffness, since the cords would not be pre-tensioned by inflation. The observed response supports this as shown by the small capacity and nearly nonexistent initial linear range in the load-deflection response shown in Figure 4-3 for the tube with braid angle of 55°. As the braid angle increases, the initial pretension in the cords also increases and the initiation of wrinkling occurs at higher applied load.
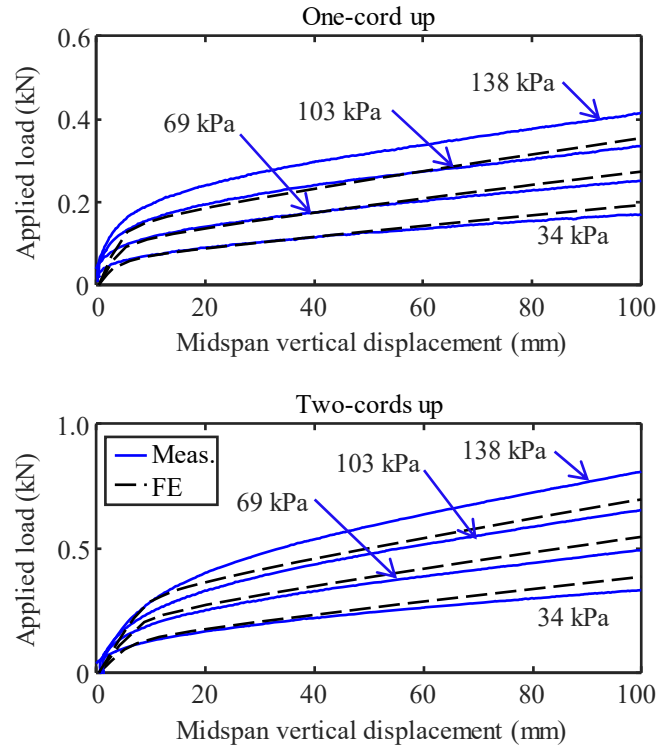
Figure 4-3. Load-displacement response of 55° tube.
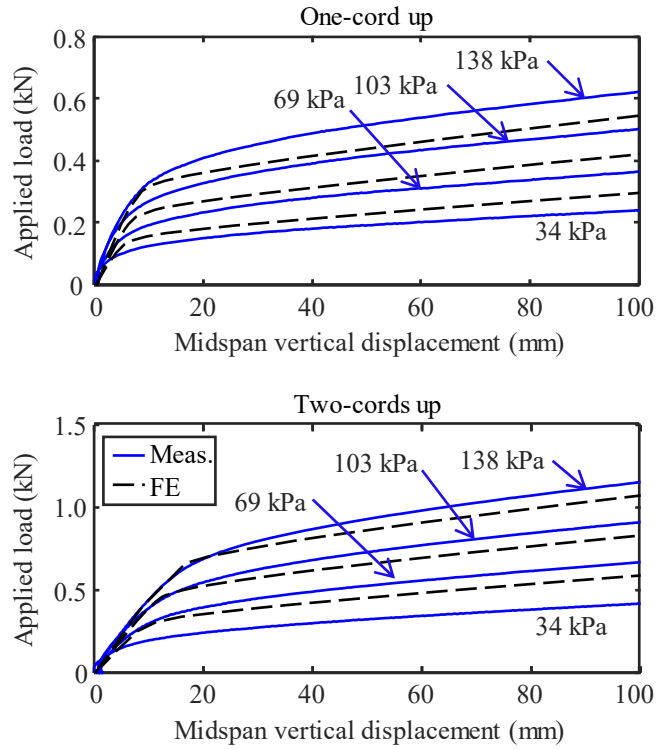
Figure 4-4. Load-displacement response of 57° tube.
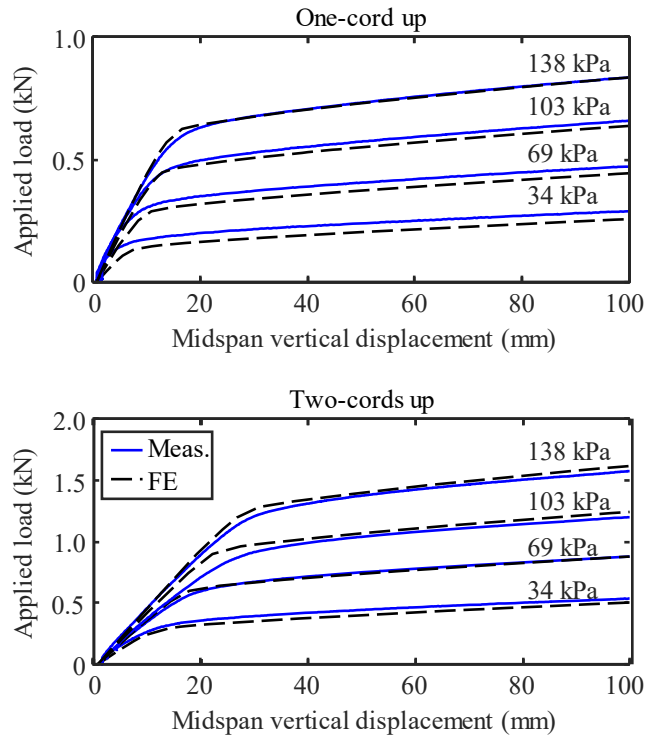
Figure 4-5. Load-displacement response of 60° tube.

71
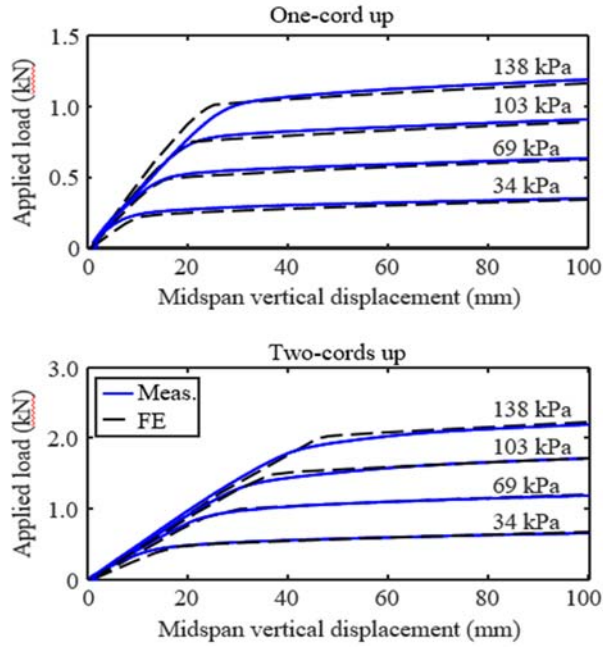
Figure 4-6. Load-displacement response of 65° tube.
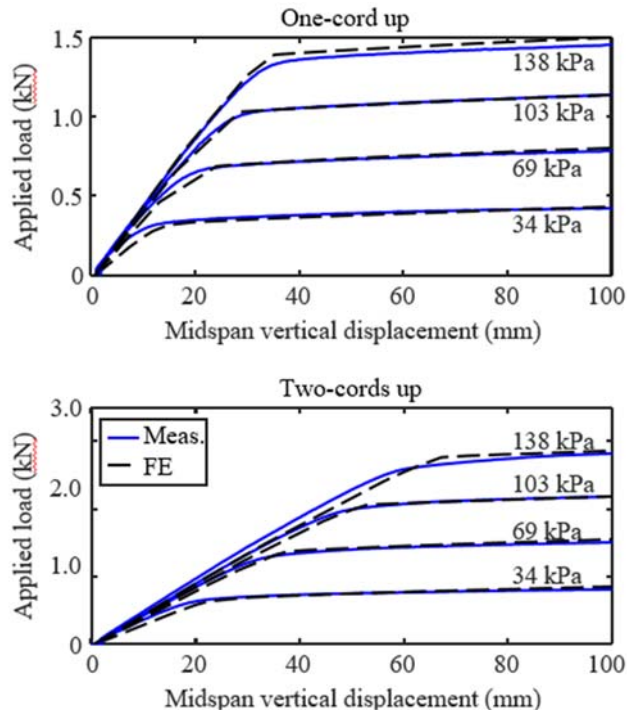
Figure 4-7. Load-displacement response of 71° tube.

The effect of pressure is also very clear in all data sets. The post-wrinkled increase in capacity at a given displacement is of a similar magnitude as the ratio of the corresponding pressure increase. For example, in all tests increasing the pressure from 69 kPa to 138 (2.0 ratio) resulted in increases of applied load at 100 mm of displacement ranging from 1.64 to 1.88 with the higher values generally occurring at the higher braid angles.

The effect of braid angle is also very pronounced as summarized in Table 4-2 where the effect of braid angle on applied load at 100mm of displacement is compared. Increasing the braid angle by less than 1.5° (57° tube vs. 55° tube) resulted in 40-50% greater applied load capacity. It is noted that the structural capacity is theoretically most sensitive to changes in braid angle at angles close to 54.7° and the data support this. However, large increases in capacity relative to the 55° tube are also noted for the 60°, 65°, and 71° tubes with increases of 60-100%, 100-190%, and 140-250%, respectively.

Table 4-2. Applied load at 100 mm mid-span displacement.

Cords Up	Pressure (kPa)	Applied Load (N) at 100 mm Displacement					Increase vs. Corresponding 55° Tube			
		Beam Nominal Braid Angle					Beam Nominal Braid Angle			
		55°	57°	60°	65°	71°	57°	60°	65°	71°
1	34	170	240	291	352	427	41%	71%	107%	151%
	69	251	363	474	633	781	44%	88%	152%	211%
	103	334	501	660	911	1137	50%	98%	173%	241%
	138	413	623	834	1191	1453	51%	102%	188%	252%
2	34	331	419	542	660	809	27%	64%	99%	144%
	69	496	668	875	1188	1497	35%	77%	140%	202%
	103	654	914	1204	1710	2186	40%	84%	161%	234%
	138	811	1151	1579	2189	2807	42%	95%	170%	246%

4.5 Digital Image Correlation Results

All digital image correlation data were processed with ARAMIS (2011) version 6.3 software. Image acquisition was initiated at an inflation pressure of 1 kPa in order to record most of the strain that occurred during inflation. A sample screenshot of the spatial variation of tube radius is shown in Figure 4-8. The regions contained within the two rectangles with dashed lines were selected for use with the "Best-Fit Cylinder" software feature to align the coordinate system with the tube axis in order to avoid including the larger radius associated with the reinforcing cord that is apparent in Figure 4-8. Spatial variation of radius for 71° tube, 103 kPa, two-cords up. An interesting observation is that the braid angle can be visualized within many of the full-field results.
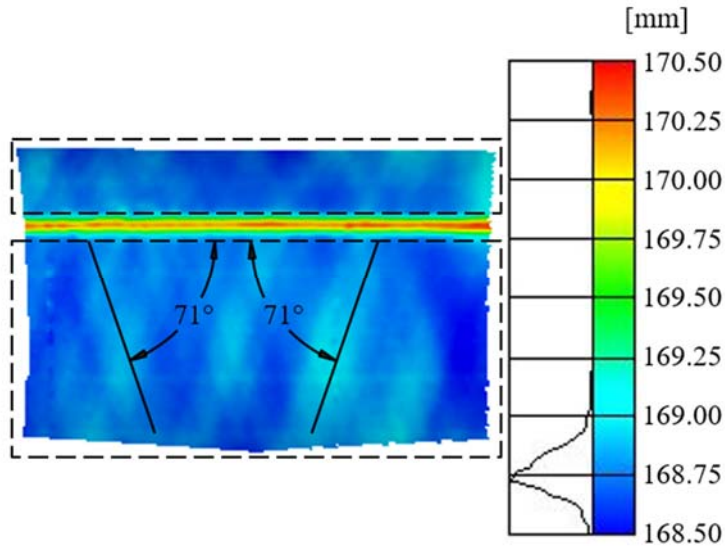
Figure 4-8. Spatial variation of radius for 71° tube, 103 kPa, two-cords up.

Sample inflation/bending strain results overlaid on the raw images for key stages of interest are shown in Figure 4-9. Figure 4-9a and Figure 4-9b show the bottom cord at 103 kPa inflation pressure and at peak bending load, respectively. Figure 4-9c and Figure 4-9d show the top cord at 103 kPa inflation pressure and at peak bending load, respectively. Both the top and bottom cords were tensioned to similar levels due to inflation as shown in the histograms next to the color-bar legends of Figure 4-9a and Figure 4-9c. Application of bending loads caused the bottom cord to be tensioned further (Figure 4-9b) and the top cord to be compressed (Figure 4-9d) as expected based on beam theory. The digital image correlation data also clearly show the development of wrinkles, regions of large localized compressive strains, at discrete locations along the cord. However, the wrinkles did not extend into the braided shell appreciably because the braid was still tensioned due to the requirement that it carry 100% of the inflation-induced hoop stress.
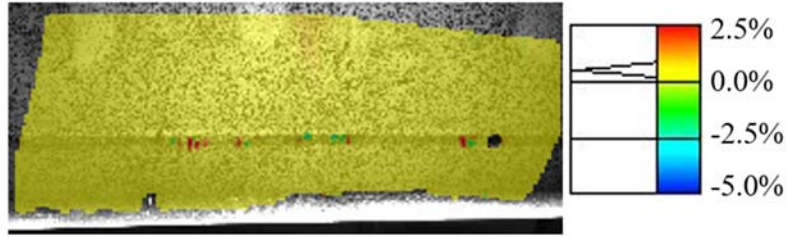
a.) Bottom cord at inflation
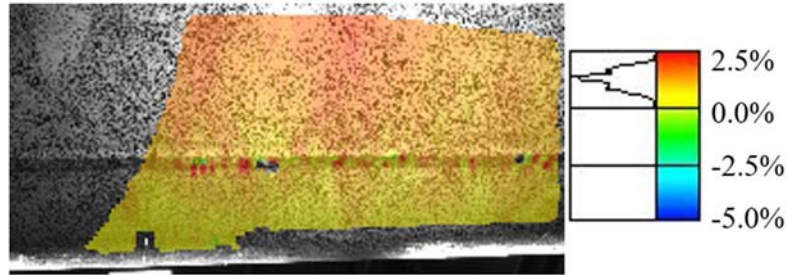
b.) Bottom cord at peak bending load
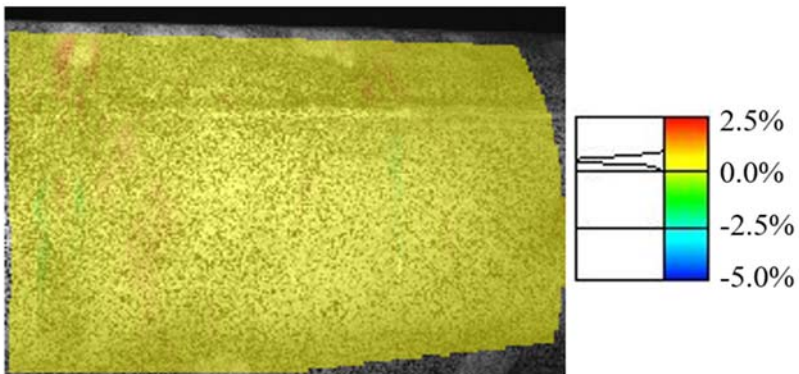
c.) Top cord at inflation
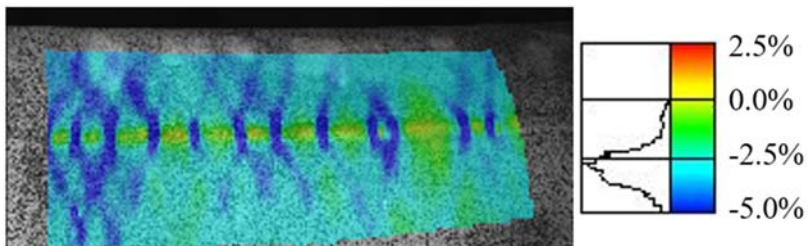
d.) Top cord at peak bending load

Figure 4-9. Representative longitudinal strain fields for 71° tube, two-cords up, 103 kPa.

The measured strains as a function of applied load are shown by the symbols in Figure 4-10, where ε_L is longitudinal strain and ε_H is hoop strain. Strain predictions from the FE model discussed later in Section 4.6 are also shown. It was noted that there was considerable variability in the longitudinal strains along the length of the cords, so the strains reported here are derived from a "Point-Point Distance Analysis" measured over the full field of view to give an average value.
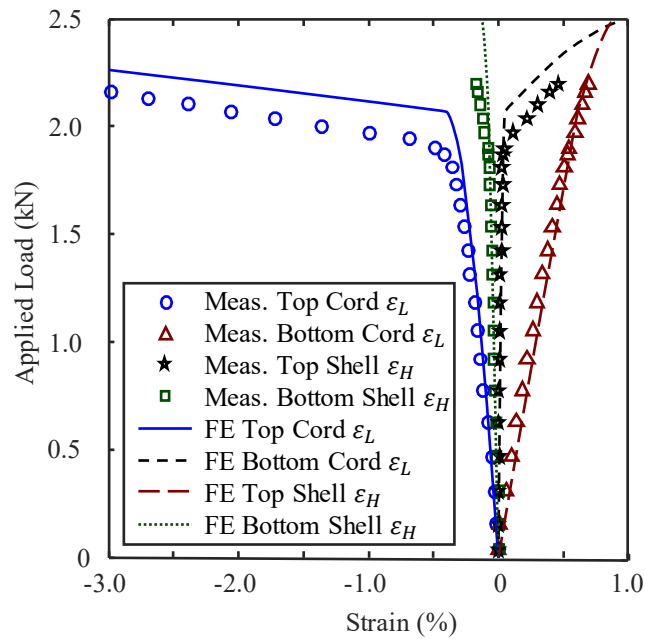
Figure 4-10. Strains due to applied loading for 71° tube, two-cords up, 103 kPa.

The reported hoop strains are based on a spatial averaging of hoop strain for regions of the shell near the cords. The number of data points shown is less than measured for clarity. The longitudinal strains were also used to calculate the bending neutral axis as a function of applied load as shown in the Figure 4-11. A few data points at low levels of applied load were omitted because the strains were of similar magnitude to the resolution of the digital image correlation

system and therefore the neutral axis location could not be accurately determined. It is shown that the neutral axis is generally near the middle of the cross-section through most of the load range, but then drops significantly after wrinkling occurs leaving the top cords with very little stiffness.
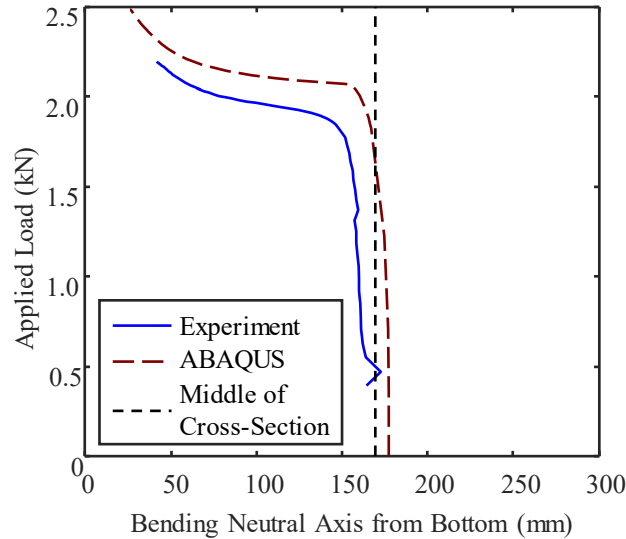
Figure 4-11. Neutral axis location during bending portion of test for 71° tube, two-cords up, 103 kPa.

4.6   Shell Finite Element Models

Three dimensional (3D) shell-based finite element (FE) models of the straight, inflatable tube tests were developed by Andrew Young as described in Clapp et al. (2016b) and Young (2017). The models rely on material properties for the braid and reinforcing cords that are described here. Therefore, the ability of the FE models to accurately capture the response of the inflatable tube 4-point bending tests can be directly assessed by comparing model predictions with the bending tests described in this paper. If the FE models prove accurate, they can serve as useful tools for predicting the effect of various material models or configurations. Further, building on the relatively straightforward straight tube bending model, the response of larger and

more complex structures such as single or multiple tori configurations or the HIAD structure can be simulated using the same approach detailed in this study with a reasonable degree of confidence.

4.6.1 Comparison of Load-Deflection Results

Figure 4-3 through Figure 4-7 present the FE 4-point bend test model results compared to test data of the inflatable tubes. In all cases, the third loading cycle of the inflatable tube is presented. The FE model predictions generally compare very well with the load-deflection test data of the inflatable tubes at all inflation pressures and cross-sectional orientations, particularly at the higher (60°, 65° and 71°) braid angles that are of most interest for structural applications. For the case of the 55° and 57° tubes, the model predictions do not compare as well to test data. However, these tubes have the lowest capacity and are not of interest for structural applications.

The FE-predicted strains as a function of applied load are shown in Figure 4-10. The load-carrying capacity is over-predicted by the FE model in this case, but all of the strains compare quite well with measured values and follow the same trends. The bending neutral axis location was also derived from these strains as was done for the experimental results and is shown in Figure 4-11. Once again, the neutral axis is shown to be near the center of the tube until the top cords lose most of their initial stiffness and the neutral axis shifts downward in the cross-section. The trends are in good agreement with the experimental data.

4.6.2 Capturing Secondary Effects

In addition to in-plane bending displacements, small out-of-plane displacements were also observed during tube testing. The magnitude of the out-of-plane displacement was much higher when specimens were tested in the two-cords up configuration than in the one-cord up

configuration. The out-of-plane displacement in the two-cords up configuration is driven by both

top cords losing tension as the tube is loaded. While the circular cross-section is still nominally

symmetric with a high torsional stiffness, and therefore should not move out-of-plane, the single

cord in tension provides minimal restraint to out-of-plane bending deformations. A small

misalignment of the bottom cord – due to twisting of the cross-section, for example – can

therefore result in lateral deflection.

The phenomenon of out-of-plane displacements was observed in the DIC data and could

also be captured using the FE models. Details are presented by Young (2017), however it is

noted that measured out-of-plane displacement is of the same order of magnitude as predicted by

the FE model as shown in Figure 4-12 for the 71° tube at 138 kPa inflation pressure.
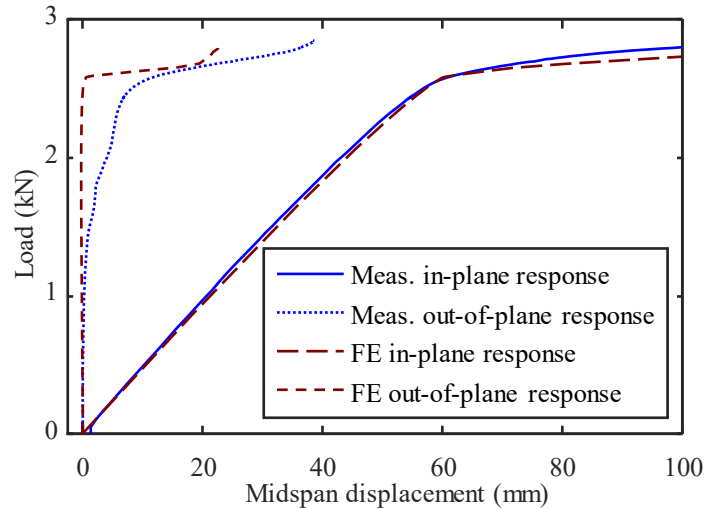
Figure 4-12. Vertical and transverse deflection comparison.

Both vertical and horizontal displacements of the test specimen were captured with the

ARAMIS (2011) digital image correlation system. As can be seen from the results, the FE model

captures the out-of-plane response reasonably well: at load levels close to those where the top cords lose pretension the out-of-plane displacements become more significant.

4.6.3   Comparison with First Loading Cycle

All load-deformation responses shown prior to this point were made to the third inflatable tube loading cycle, since it was experimentally observed that by the third loading cycle the response of the inflatable tube was consistent and repeatable. This was desirable given that each tube was tested multiple times, at multiple pressures and multiple orientations. However, during a deployment situation, where the HIAD structure may be stowed for many months prior to inflation, extensive pre-conditioning to obtain a consistent and repeatable response may not be possible. It is therefore desirable to both have a reasonable expectation of how much softer the response will be and to be able to use the FE model to predict the response on the first loading cycle. As a representative test case, the first ever loading cycle of the 71° tube specimen in the one and two cords up configuration was examined as shown in Figure 4-13. The inflation pressure was 103 kPa.
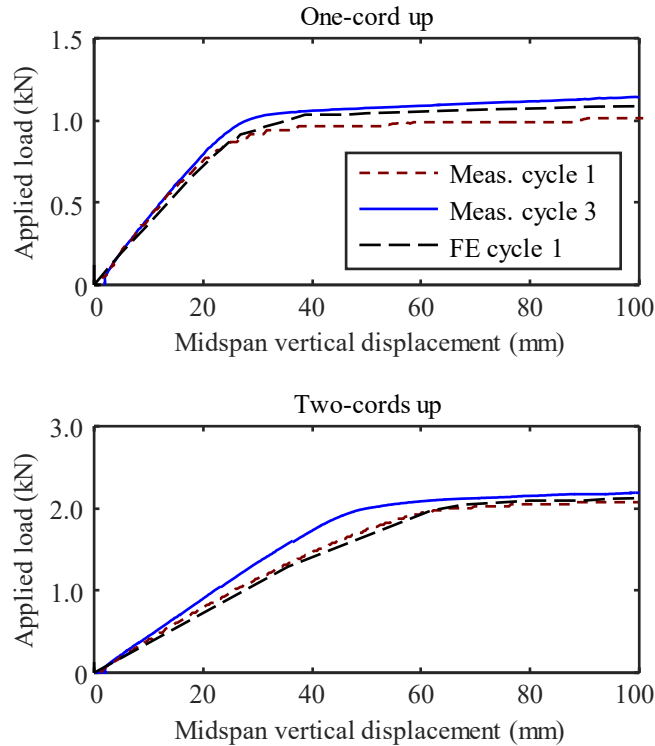
Figure 4-13. Comparison of cycle 1 response vs. cycle 3.

The response of the tube is clearly softer in the first cycle of loading as compared to the

third cycle of loading for both orientations and the capacity is also lower. The data from the third

cycle is also shown for comparison. In this case, the displacement has been zeroed based on the

state at the beginning of the cycle. The displacement at zero load would be greater than zero if

the same reference position was used for both Cycle 1 and Cycle 3. In the one-cord up

configuration, the initial stiffness is very similar for the first and third runs while, in the two-

cords up configuration, the first run's response is significantly softer than the third run.

The FE model using the measured data from the first cord tension test loading cycle is

also able to predict the same trends in behavior that were observed. In both cases, the response is

captured well by the FE model. This illustrates the sensitivity of the FE model to material

property inputs, and provides additional confidence that good capacity and stiffness predictions can be obtained when the appropriate material inputs are used in the model.

4.7 Summary

A large matrix of experiments was successfully performed to characterize the bending behavior of straight, inflatable, braided tubes with integral reinforcing cords. Several parameters were considered in the experiments: tube braid angle, tube cross-sectional orientation, level of internal inflation pressure, and the effect of cyclic loading. These data provide a solid set of baseline configurations with highly controlled loading and boundary conditions to validate FE models. The predictions in the model developed by Young (2017) agree quite well with the experimental data, particularly for the tubes with larger braid angles that of the highest interest for structural applications.

5   SINGLE TORUS RADIAL COMPRESSION TESTING AND MODELING

After completion of the straight beam bending tests described in Chapter 4, the next logical step in complexity is to move on to testing individual torus elements. However, the increase in complexity is actually quite substantial: unlike a beam, the torus and test fixture will be self-reacting under in-plane loading, and the torus can therefore experience significant in-plane rigid body motion. The load application method becomes critical because the loading mechanism has the potential to both force it inwards as well as restrain it from moving outwards.

The primary objective of the research reported in this chapter was to investigate and develop methods for testing individual tori under in-plane loads. A secondary objective was to investigate techniques for FE analysis of the torus test. The work reported here was a necessary pre-cursor to the extensive torus testing program reported by Whitney (2016), which was in turn relied upon by Young (2017) to validate beam-based finite-element models of individual tori.

This Chapter is organized as follows. The first section gives background of previous testing performed relatively recently by NASA using the same test fixture used at UMaine. Next, the modifications to the experimental setup made at UMaine are reviewed, including a description of the load frame, measurement methodology, loading strategies and descriptions of the torus test articles documented in this Chapter. Next, results of initial torus testing are presented. This is followed by a description and overview of the modeling methodology. Comparisons are made between the models and experiments. The Chapter closes with a summary, conclusions, and recommendations for future research.

5.1 Review of prior torus testing by NASA (Chen and Moholt 2014)

Young et al. (2017) provide a summary of prior work related to the structural response of inflatable tori that is primarily limited to analytical studies, but does include some limited static testing. Therefore, the recent testing by NASA is the focus of this review of prior work.

A total of 8 torus test articles with 6 meter HIAD construction ranging from T3 size to T5 size (recall T1 is the smallest torus adjacent to the rigid center body) were individually tested by NASA Armstrong Flight Research Center (Chen and Moholt 2014). The major outside diameter of these tori ranged from 3.35 m to 4.44 m and articles were constructed with 3 different braid angles: 60°, 65°, and 71°. Both uniform compression and combined compression/torsion tests were performed. A photo of the test setup is shown in Figure 5-1.
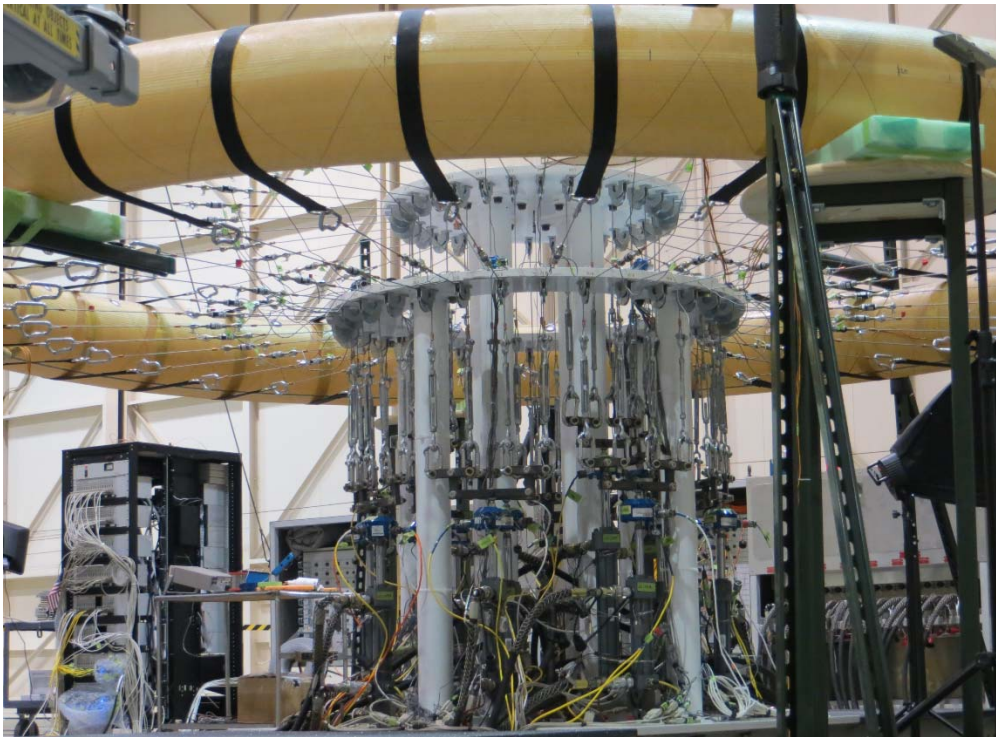
Figure 5-1. Photo of Torus Test Setup at NASA Armstrong Flight Research Center.

One of the goals in the NASA testing was to approximate a uniform load by using a large number of discrete point loads. Preliminary finite element model results by NASA led to the selection of 32 load points since the predicted response was shown to be similar to uniform compression. It was also desired to conduct tests with combined compression and torsion, therefore each of the 32 points required a top and bottom cable for a total of 64 cables as shown in Figure 5-1. The number of servo-hydraulic actuators used in the testing was equal to 16, so whiffle trees were used in an effort to uniformly distribute the load from a single actuator to 4 steel cables as shown in Figure 5-2. In-line load cells were used on each of the 64 cables near the torus. For control purposes, a 5th load cell per actuator (blue colored in Figure 5-1) was mounted directly to the actuators.
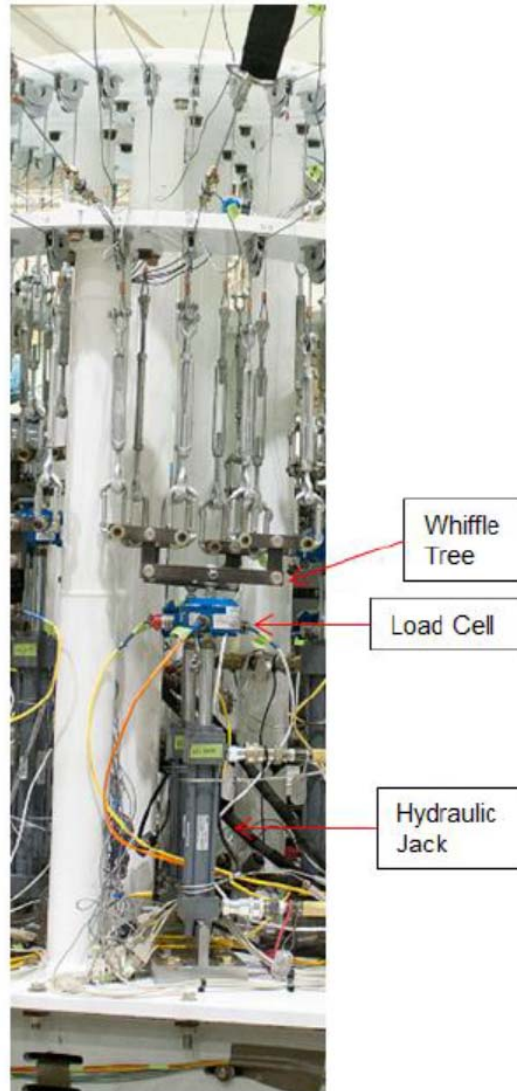
Figure 5-2. Photo of whiffle tree system and hydraulic actuator at NASA Armstrong (Chen and Moholt 2014).

The servo-hydraulic actuators respond very rapidly and the load in each of the 16 actuators was very consistent and well controlled. However, it was discovered that friction in both the whiffle tree assembly as well as the pulleys resulted in highly variable loads not only for the 4 in-line load cells for a given actuator, but also the total loads for each actuator. PONTOS (2011) software was used to track arbitrarily placed markers located on the upper side of the torus, but the data was mainly only used as a visual "movie" to look at the deflections of the

torus and judge whether or not out-of-plane movements occurred. The number of tracking points in early tests was sufficient to quantify the actual shape of the torus, but this estimation of torus shape was not done and later tests had fewer points that would have made shape-fitting inaccurate. Nonetheless, the structural testing of tori at NASA Armstrong provided very valuable data. Some interesting observations were noted:

1. The tori that carried the largest loads, which had a 71° braid angle and was inflated to 138 kPa, showed degraded performance with each subsequent cycle of loading that was applied, and the peak load achieved in the test decreased with each cycle.

2. The buckled shape for test articles with low initial load in the axial cords (either due to a small braid angle or small inflation pressure) tended to be dominated by out-of-plane deformations, whereas the buckled shape for articles with high initial cord load tended to be dominated by in-plane deformations.

3. The measured loads were much higher than theoretical elastic in-plane buckling loads (Weeks 1967). The relatively low predicted theoretical elastic buckling load is due to the low bending stiffness provided by only having two cords located very close to the neutral axis. This discrepancy is due to the fact that additional restraint that is provided to the torus by the load cables.

4. The NASA-developed FE models tended to over-predict the peak test loads assuming defect-free initial geometry, and indicate that peak load would be governed by loss of cord pretension rather than buckling. The introduction of small defects to the initial

torus shape resulted in good agreement between the total applied load predicted in the models and that measured in experiments, but the actual shapes were not quantified.

After the testing by Chen and Moholt (2014) was completed, the test fixtures and hardware were sent to the University of Maine. Several lessons were learned based on review of the NASA test data as well as detailed inspection and review of the test setup, which led to some changes and also informed the objectives of the testing performed at the University of Maine:

1. The tests at NASA Armstrong were run in load control, yet the loads in the cables were highly variable. The testing at the University of Maine conducted with 64 cables utilized improved mechanical systems to reduce variability and also used the sum of the load in the 4 applicable cable load cells as the comparison to the set point for purposes of control.

2. Mechanical systems (i.e. pulleys and whiffle tree assemblies) were upgraded to provide less frictional resistance and therefore less variability in cable loads.

3. The stiffness of the mechanical systems applying load to the torus were quantified and considered in FE models (Young et al. 2017).

4. The full 3D shape of the tori at all stages of the project were accurately quantified through the careful use of photogrammetry data and MATLAB (MathWorks 2016) code that will be discussed in more detail.

5. The effect of load-control vs. displacement-control was investigated by conducting tests both ways and comparing the response.

5.2 *Description of test articles*

All test articles described in this Chapter had a nominal minor diameter of 345 mm and a nominal braid angle of and 71°. Although many tori were tested, only the results for two tori are shown: T4A-1 and T4AP-1. These tori are both nominally the same size and represent the fourth torus outwards from the rigid center body of the 6-meter HIAD. Torus T4A-1 was previously tested at NASA Armstrong. It was used by University of Maine for early experiments performed for a variety of reasons such as instrumentation verification, tuning of the control system, and investigating different ways of running the experiments (i.e. load-control vs. displacement control). A much more comprehensive suite of experimental results is described in Whitney (2016).

The geometry is representative of the fourth torus in the six-meter major diameter HIAD structure that was experimentally investigated by NASA researchers (Cassell et al. 2013). The material system consists of a braided Technora fiber shell with an impermeable urethane gas bladder and is identical to the material system investigated in Clapp et al. (2016a and 2016b), Whitney (2016), and Young et al. (2017a and 2017b). The minor radius of the as-built inflated torus is about 170 mm and the braid angle is about 70.5°. Two Technora axial reinforcing cords, identical to those detailed in Clapp et al. (2016b), were nominally located at ±60° from the inside equator of the torus, as illustrated in Figure 5-3.
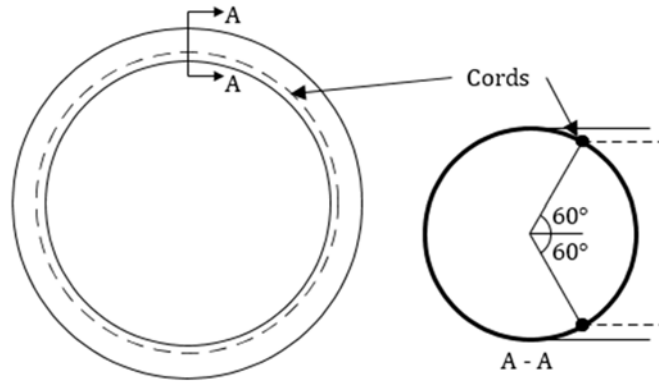
Figure 5-3. Torus and cross-section geometry (Young et al. 2017b).

5.3   Torus experimental setup

The self-reacting torus test load frame consisted of 25 mm thick horizontal top and

bottom circular plates vertically offset by 345 mm, plate support posts and a floor reaction plate,

as shown in Figure 5-4. Sixteen electric actuators were mounted vertically around the outer

perimeter of the floor reaction plate, with pairs of actuators applying load to the top and bottom

of the torus cross-section at eight different circumferential locations. The first loading point was

located at 0° or 11.25° measured counter-clock-wise from the reference axis shown in Figure 5-5

for 64 cable testing and 16 cable testing, respectively. Cables attached either to the whiffle tree

system or directly to the actuators and then passed over a pulley attached to the underside of the

circular reaction plates and radially out towards the inflatable torus member. Each cable was

connected to one end of a 50 mm wide fabric strap that was wrapped around and bonded to the

inflatable torus. Each loading cable included an inline load cell located near the torus and a string

potentiometer located near the fixture to measure radial displacement.

91
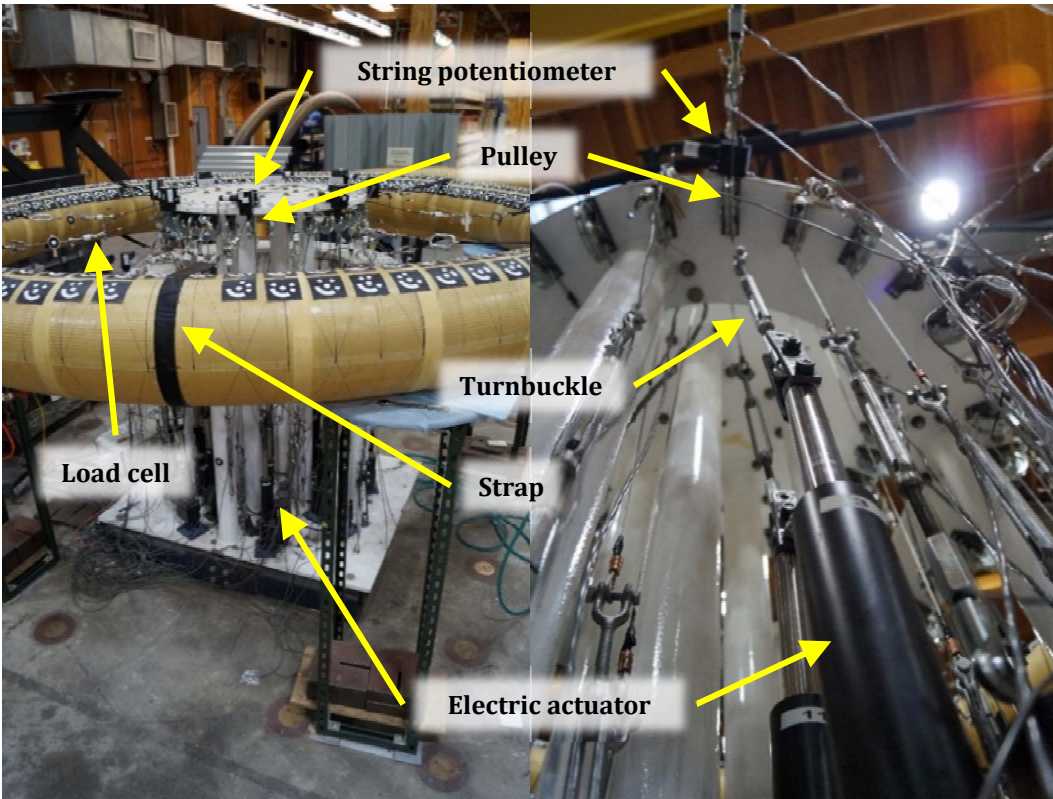
Figure 5-4. Torus test configuration for testing with 16 cables (Young et al. 2017).
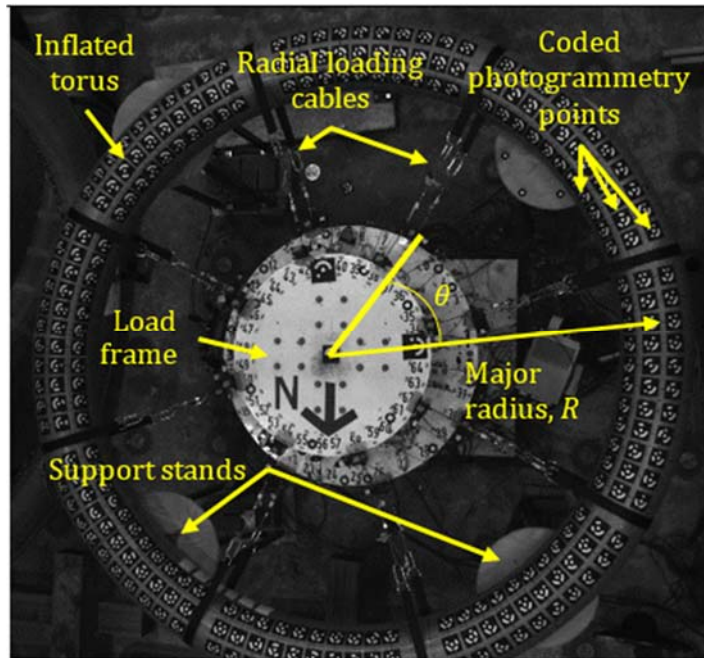
Figure 5-5. Photogrammetry view of test configuration with T3 torus shown (Young et al. 2017).

The University of Maine upgraded several of the mechanical systems required for testing tori with 64 cables as shown in Figure 5-6. The result of these changes was primarily much more variability in the load among the four cables conneted to a given whiffle tree. The effect of this change is shown in Figure 5-7 where the standard deviation of load among the four cables is plotted against the total applied load. It is apparent that the standard deviation is much less in the University of Maine setup.

Figure 5-3. Photo of mechanical improvements implemented by University of Maine: new pulleys and housings (top left), improved cable-to-whiffle tree connections (bottom left), and reduced friction whiffle trees (right).
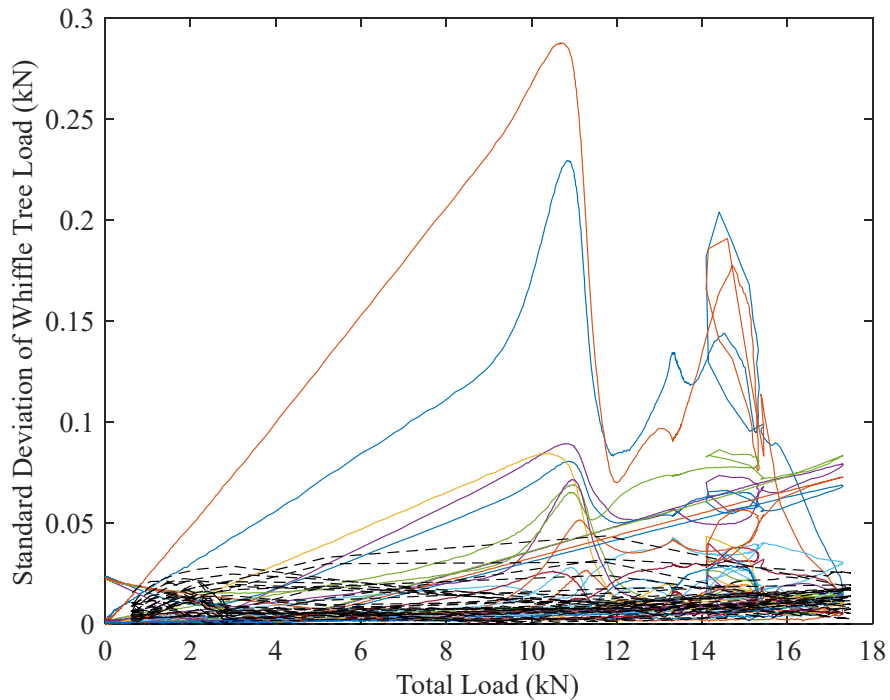
Figure 5-4. Standard deviation of load per whiffle tree (solid colored lines: NASA Armstrong, dashed black lines: University of Maine).

The inflated torus was supported vertically by four test stands evenly spaced around the test setup. The diameter of the torus supports was 570 mm and the support centers were located at 45°, 135°, 225° and 315° measured counter-clock-wise from the reference axis shown in Figure 5-5. Two layers of peel ply release fabric were placed between the supports and the torus to minimize friction.

Sixteen, Celesco PT1A-10 string potentiometers were wired to two, eight channel NI TB4339 data acquisition cards to measure the cable displacements produced by each actuator as the torus was loaded. These strings pots accurately measured the cable movements in real time, which enabled the system to operate in displacement control (Whitney, 2016).

5.3.1 Photogrammetry measurements and torus shape fitting

While cable load and cable end displacements were obtained from instrumentation which interfaced directly with the loading cables, the initial and displaced shape of the torus were measured using non-contact photogrammetry techniques. PONTOS (2011) version 6.3 software was used to process the photogrammetry data. Two overhead cameras with 5-megapixel resolution were mounted on scaffolding above the test frame. A photograph of the torus test setup is shown in Figure 5-8. The cameras are mounted to the aluminum camera bar shown near the top of the photo. Lenses with 8 mm focal length were used to provide a large enough field of view without needing to located at a height that would interfere with overhead cranes.
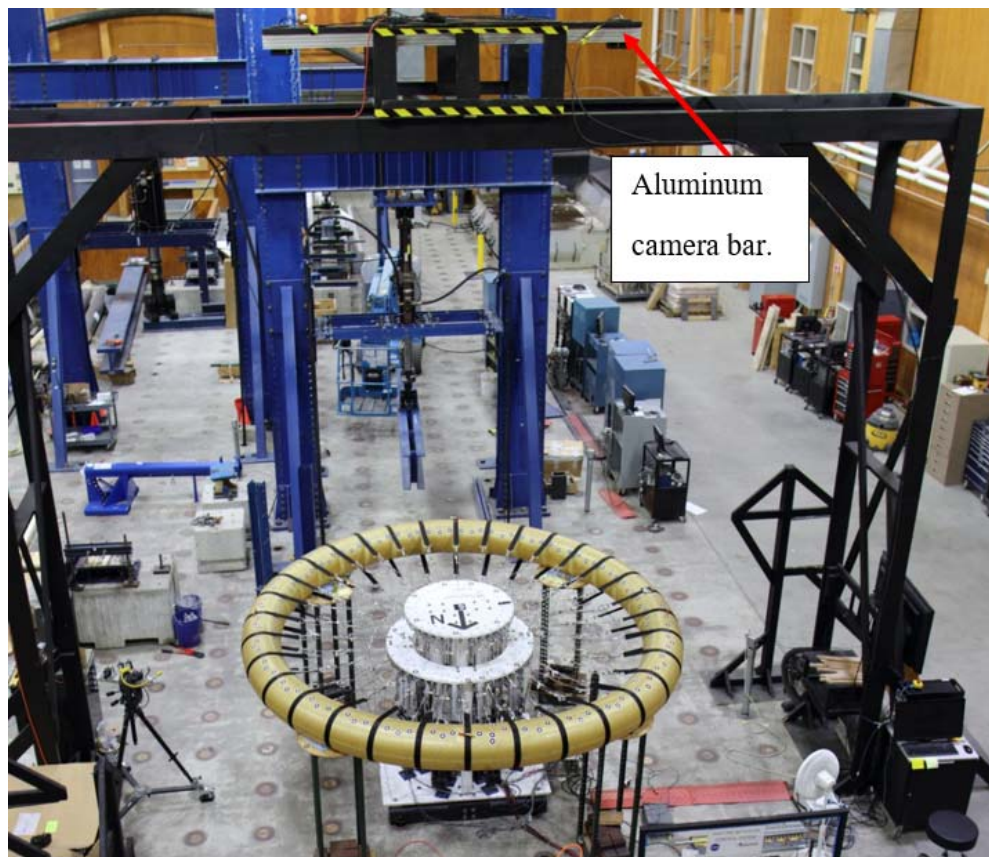
Figure 5-5. Photo of torus test setup at University of Maine.

The calibrated volume was large enough to accommodate up to a T5 torus and is the largest volume calibrated to-date at the University of Maine. The theoretical in-plane and out-of-plane accuracy of the test setup used in this study is about 0.016 mm and 0.053 mm, respectively (Schmidt et al. 2003). The observed noise in total displacement magnitude with no loads applied was typically less than 0.5 mm. A photo from one of the cameras is annotated in Figure 5-5. The top of the load frame is visible along with radial loading cables and straps, the inflated torus, coded photogrammetry points and the four torus support stands. The cylindrical coordinate reference axes R and θ are also shown (Z is out of the page).

The location and movement of the individual photogrammetry points in three-dimensional space were tracked throughout the duration of an individual test. The photogrammetry system took pictures of the experimental setup at a rate of 2 Hz. An algorithm was developed to determine the location of the center of the torus cross-section at locations around the circumference of the torus based on the location of arbitrarily placed photogrammetry points located on the surface of the torus. Although the points can be arbitrarily placed, Whitney (2016) used rational methods and took great care in point placement to align the points with the braid tracer intersections so even more information could be obtained such as braid angle and curvature.

The coordinate system was defined by placing three coded points on the test fixture itself. Coded point 0 was placed in the center of the fixture top plate to define the center of the cylindrical coordinate system. Point 1 was placed in alignment with pulley 1, which along with point 0 defines the axis for which $\theta = 0°$ (see Figure 5-5). Coded point 2 was also placed on the fixture to serve as the 3rd point for defining a plane. It is not guaranteed that these coded points

will be correctly captured and identified by the software. Sometimes the points were captured, but the identification number was not able to be determined. In this case, the points were identified in MATLAB (MathWorks 2016) based on the proximity to the known locations of the coded points. As an additional backup, several additional non-coded points were placed on the fixture. These points were ignored unless one or more of the coded points 0-2 were completely lost (this very rarely occurred), then as many of them as possible would be used to do a best-fit to known coordinates to create a virtual point for the one or more coded points that were missing.

Another technique utilized in this research was to modify the raw images prior to loading them into the photogrammetry software. The vast majority of the information captured in all images, regardless of torus size, was not relevant to the experiment. Therefore, "masking" routines were developed by high school intern Spencer Campbell and later modified by Whitney (2016) to turn pixels that were not of interest into a single gray-scale value as shown in Figure 5-9. This has many advantages:

1. File size is reduced by over 90% for T3 tori.

2. Computational processing time within PONTOS is reduced by about 60%.

3. Data quality is improved both because false points are far less likely to be identified and also because PONTOS (2011) apparently adjusts the sharpness of the images to maximize contrast between the white points and the black background based on the pixels captured.
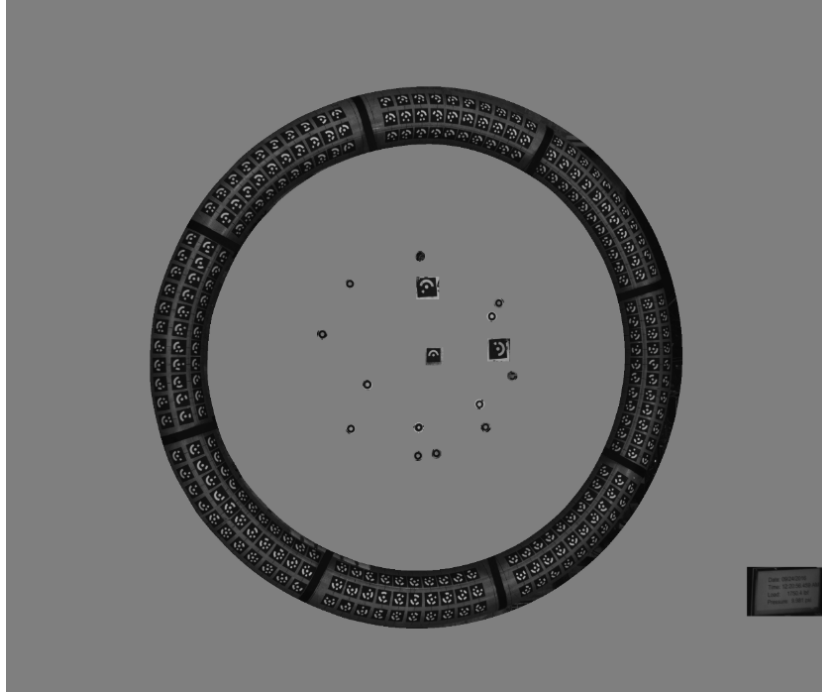
Figure 5-6. Edited photograph for the photogrammetry software.

It should be noted that the masking process is not static, but rather is adjusted based on deflections of the torus to ensure the full torus is always captured while at the same time maximizing the portion that is masked. The items that remain in Figure 5-9 are the torus, the three coded points on the fixture that define the coordinate system, the additional non-coded points on the fixture used as backup, and a view of a computer monitor in the bottom right that contains live information about the experiment as shown in Figure 5-10. The entire test matrix for a given torus was pre-programmed and then testing occurred for 24 hours per day for about 4 days.
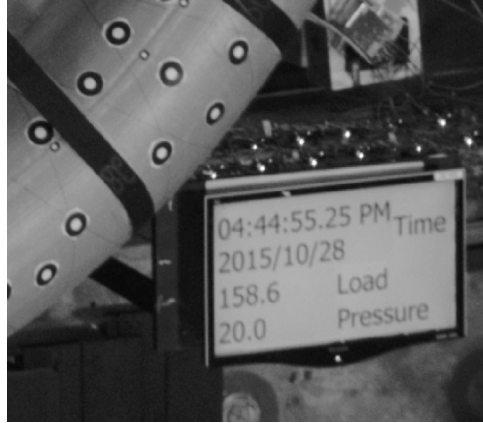
Figure 5-7. Photograph of example live information displayed during a torus test: time, date, total load (lbf), and pressure (psi).

The raw coordinates were transformed to the coordinate system previously mentioned with an additional Z offset to shift the coordinate system to $Z = 0$ at the vertical center of the torus. This was done for all stages in the project to eliminate effects from rigid body motion that could occur, for example, if someone leaned on the scaffolding to which the cameras were mounted.

The strategy employed to determine the center point of the torus cross-section was to locally fit a torus to a subset of the data for each of the markers on the torus. This was done by subjecting the raw coordinates (x, y, and z) to 5 fitting parameters: a translation (x_t, y_t, and z_t) and rotations (α_x and α_y about the axes indicated) as shown in Equation 5-1.

$$\begin{bmatrix} x' \\ y' \\ z' \end{bmatrix} = \begin{bmatrix} x_t \\ y_t \\ z_t \end{bmatrix} + \begin{bmatrix} \cos(\alpha_y) & 0 & \sin(\alpha_y) \\ \sin(\alpha_x)\sin(\alpha_y) & \cos(\alpha_x) & -\cos(\alpha_y)\sin(\alpha_x) \\ -\cos(\alpha_x)\sin(\alpha_y) & \sin(\alpha_x) & \cos(\alpha_x)\cos(\alpha_y) \end{bmatrix} \begin{bmatrix} x \\ y \\ z \end{bmatrix} \qquad \text{Equation 5-1}$$

The major radius R was taken as the 6th fitting parameter and the minor radius r was taken as being constant at 170 mm. The calculated minor radius r_{calc} for each point based on the

fitting parameters was then calculated as shown in Equation 5-2. The error function shown in Equation 5-3 using the 2-norm (square root of sum of squares) was then minimized by using the built-in MATLAB (MathWorks 2016) function *fminsearch*. Many other methods were investigated for minimizing this error function, but none were quicker for this particular problem.

$$r_{calc} = \sqrt{z'^2 + \left(\sqrt{x'^2 + y'^2} - R\right)^2}$$ Equation 5-2

$$\emptyset = \|r - r\_calc\|_2$$ Equation 5-3

The center of the torus minor cross-section was determined at the same angular location as the coded points on the torus. It was found that using 21 points (i.e. the point itself plus the nearest 10 clockwise and 10 counter-clockwise) for the local torus fit provided an excellent balance of speed and accuracy. Using fewer points should yield more accurate results if there were highly localized effects, but it actually increased solution time and it was observed that there was very little difference in the fitted shape using fewer points for the torus tests described in this Chapter where only fairly small string pot displacements of up to 38 mm were applied. The same claim cannot be made for some of the tests described in Whitney (2016) and Young et al. (2017b) where much larger displacements were applied.

After the local torus fit was performed, a second back-calculation was performed to determine where the coordinates of the fitted torus centerline intersected the original θ so that the final result was coordinates at the center of the torus cross-section in the original coordinate system. Many scripts were developed in MATLAB (MathWorks 2016) to visualize the shapes of the tori for different purposes, an example of which his shown in Figure 5-11.
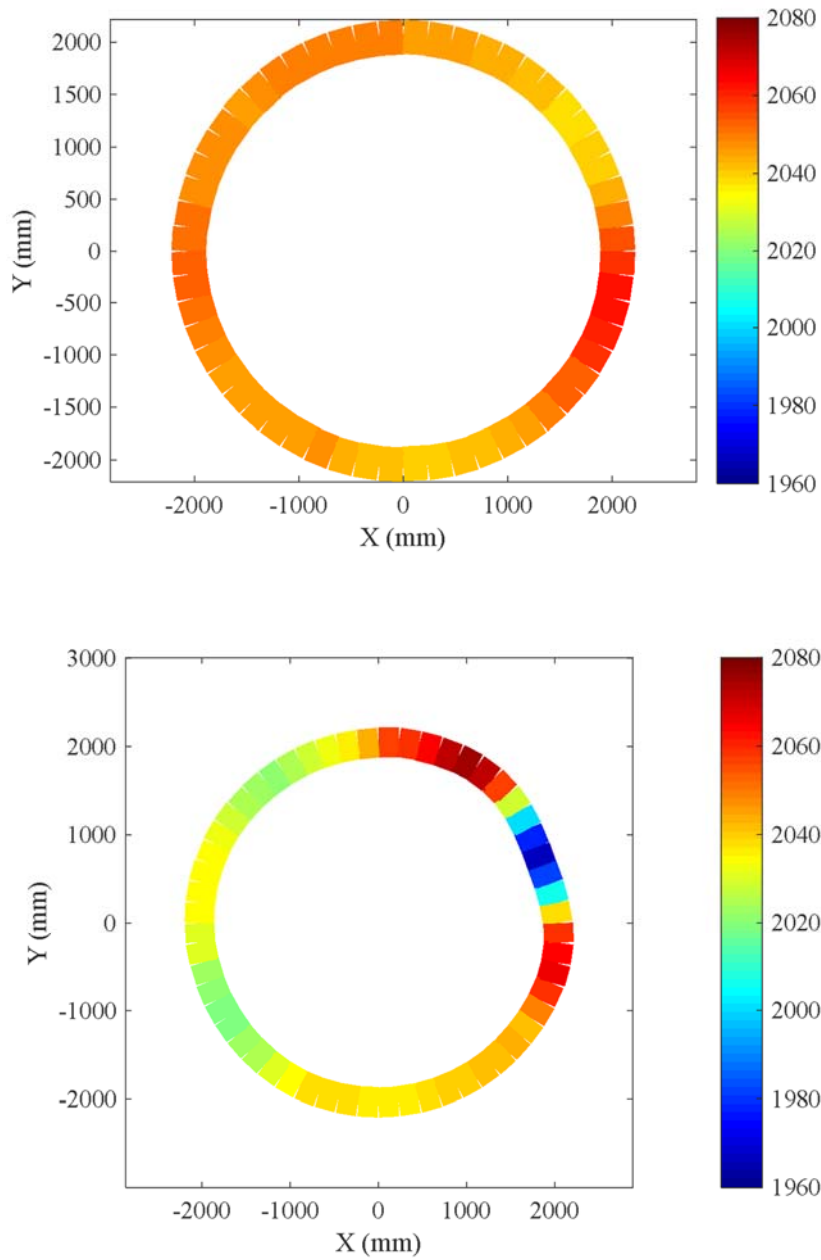
Figure 5-8. Example color visualization of local radial distance of torus minor diameter centroid (top: at 45 N per cable pre-load, bottom: at peak applied load) using photogrammetry data from NASA Armstrong.

5.3.2   Experimental control strategy

As detailed in Whitney (2016), the internal inflation pressure was regulated prior to all loading tests, and then the air supply line was closed during each loading test. A control system was developed in-house to synchronize the 16 electric actuators that relied on a load corrected proportional, integral, derivative (PID) controller (e.g. see Dorf and Bishop, 1998). An important consideration in the testing of an inflatable torus structure is the control strategy used to apply the in-plane loading. Two major control schemes were considered: load control of individual cables and displacement control of cable ends. Details of the control system are provided in Whitney (2016).

Initial testing was conducted using a load-controlled strategy with a linear ramp, and although the individual actuators did a reasonably good job of matching the target load set-point, variability in loads for all 16 actuators was unavoidable due to the response time being much slower than hydraulic actuators. The coefficient of variation of load was up to about 10% maximum. Further, when developing the modeling strategy to capture the response of the inflatable members (as discussed in Young et al. 2017b), geometric imperfections were found to drive the fundamental ovalization buckling mode rather than the experimentally observed buckling mode and resulting displaced shape. This was attributed to constraints on the experimental configuration caused by the control system's inability to apply perfect load control across all 16 actuators. This was exacerbated by the use of electric actuators that could not rapidly react to changes in loading, and the concern that the actuators might exhibit run-away response when trying to compensate for poor load control.

As a result, a radial, cable-end displacement control strategy was adopted by Whitney

(2016) to load the torus. The displacement of string potentiometers attached to the radial cables

was used to control the translation of the actuators. This experimental control strategy gave more

repeatable results than controlling the load level in individual actuators, and actuator run-away

was no longer a concern.

5.3.3   Results

Several data sets for testing conducted on torus T4A-1 in load-control with 64 cables are

shown in Figure 5-12. In these experiments, several cycles of loading and unloading are shown

at each pressure with increasing displacement in each cycle. Instead of deflection on the x-axis,

as is commonly the case, the average distance from center of torus to center of the minor cross-

section is used instead to more clearly show how the initial conditions vary as a function of

inflation pressure. It is noted that the load-carrying capacity appears to be a function of inflation

pressure, though the apparent capacity indicated by the softening shown in Figure 5-12 does not

appear to scale linearly with pressure since a four times increase in pressure from 34 kPa to 138

kPa seems to yield less than a factor of two increase in capacity. It is also noted that there is

hysteresis and accumulating deformations in the response. These accumulated deformations are

likely a result of fiber tow de-crimping, and likely do not reflect permanent damage due to the

low levels of deformation. There is some grouping of data as the preload routine is wrapping up

at a load of 2.8 kN on the loading cycles prior to switching to a linear load rate (force per time)

for all 16 actuators. It is noted that the average inward displacements are of relatively small

magnitude, however the maximum (inward) and minimum (outward) displacements are both an

order of magnitude greater as can be seen by comparing 4-5 mm displacements shown in Figure

5-13 to the displacements shown in Figure 5-15 approaching positive 30 mm and negative 40 mm.
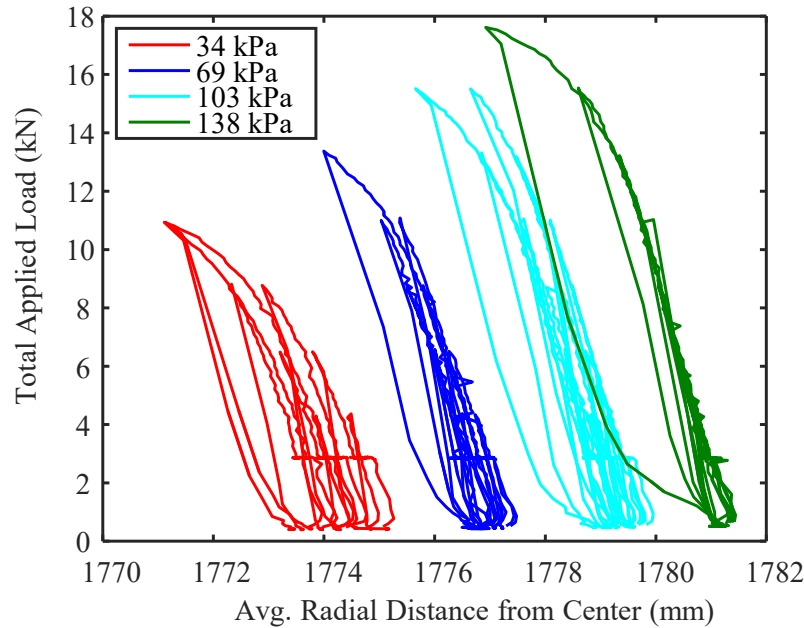
Figure 5-9. Average torus major radius based on applied load and inflation pressure.

5.3.3.1 Load-Control vs. Displacement Control

Direct comparisons between load-control and displacement control tests are difficult because only one torus was subjected to both types of loading. Load-control tests were performed first. The average radial distance from center for both tests is shown in Figure 5-13, where it appears that the response is quite similar. However, the average radius value can be misleading. The in-plane shapes of torus T4A-1 are shown in Figure 5-14 and corresponding displacements are shown in Figure 5-15. It is apparent that the shape of the torus at preload is not the same and this is likely due to a variety of factors such as other tests that were performed between those shown as well as the time that passed between tests. The shapes at a total applied load of 16 kN are also shown. The displacements shown in Figure 5-15 clearly indicate that the

torus is more restrained in displacement control testing since the magnitude of outward

displacement is much less. It is also noted that the shape of the torus in displacement-control is

square-like, whereas the shape in load-control is more triangle-like.
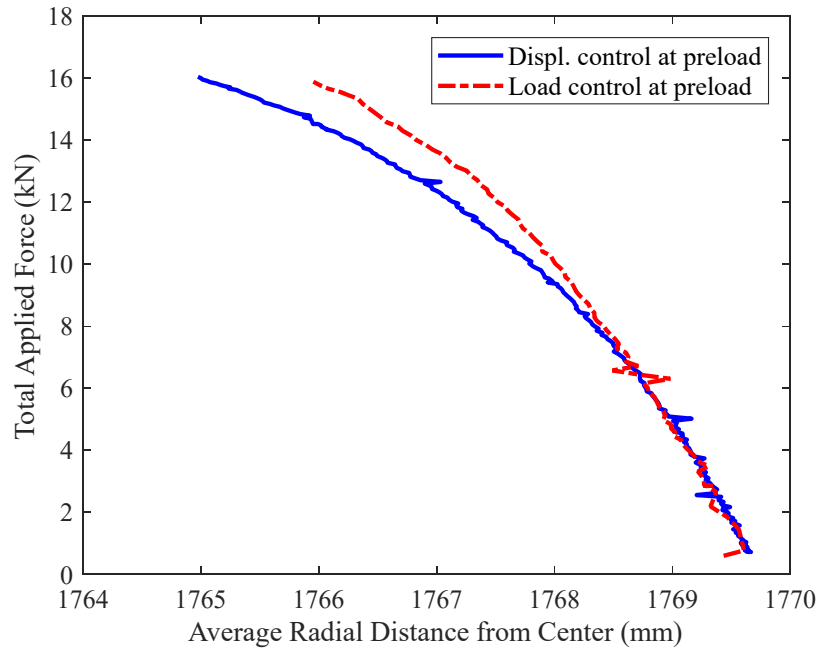
Figure 5-10. Average major radius of T4A-1 at 138 kPa inflation pressure for both displacement-control and load-control tests.
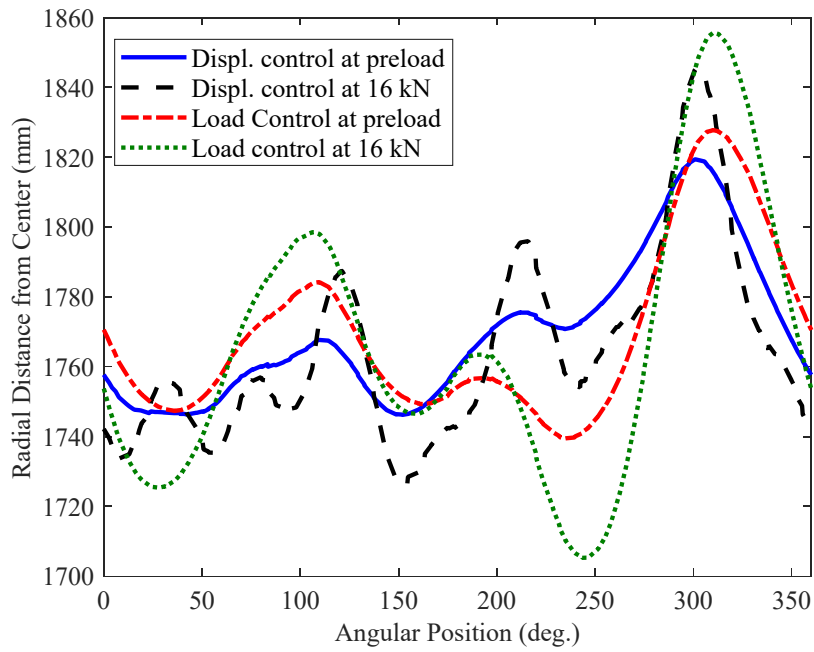
Figure 5-11. In-plane torus shapes for T4A-1 at 138 kPa inflation pressure for both displacement-control and load-control at preload and 16 kN total applied load.
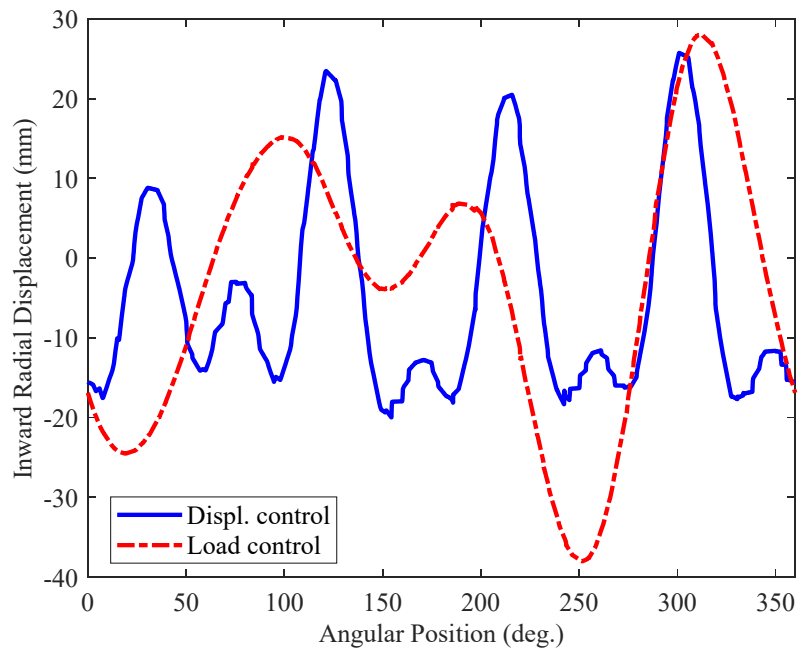
Figure 5-12. In-plane displacements for T4A-1 at 138 kPa inflation pressure for both displacement-control and load-control from preload to 16 kN total applied load.

106

5.4　Torus modeling

Being able to predict the response of the single torus test articles is a key step in working towards being able to predict the response of a full HIAD device. Shell-based 3D FE models of straight beam tests developed by Andrew Young and described in Clapp et al. (2016b) were found to agree quite well with experimental data from the straight beam bending tests reported in Chapter 4. The modeling strategy employed by Young varies in some ways from that employed in NASA modeling efforts, though it should be noted that both rely on the data reported in Chapter 3 to characterize the constitutive relationships of the structural components and both are in good agreement with beam bending test data.

The primary purpose for the high-fidelity shell-element NASA models is predicting the response of the complete HIAD structural system as accurately as possible at the expense of computation time. One of the simulation methods employed by Lyle (2015) required three days on four CPUs to generate a solution, for example. On the other hand, an objective of Young et al. (2017a) was to develop a complementary, highly efficient, beam-element-based model that captures most of the physics with greatly reduced solution times. The objective of the efforts described here was to extend the 3D shell-element modeling strategies by Young described in Clapp et al. (2016b) to be able to model the torus test and to incorporate the real geometry of the torus test articles instead of assuming perfect geometry. Andrew Young did preliminary work defining shell-based models relatively early in his time as a PhD student prior to shifting focus to the development of beam-based modeling strategies. Initial efforts of this study focused on extending these shell-based models to simulation of the torus experiments by updating the reinforcing cord constitutive relationship to be consistent with Clapp et al. 2016b for 71° braid

107

angle and 138 kPa inflation pressure and updating the geometry of the torus to be consistent with the measured geometry. However, after making these revisions, it was found that the model would no longer converge. Thus, it became necessary to revise the general modeling strategy as described next.

5.4.1 *Meshing and Modeling Strategy*

The torus designated T4AP-1 was modeled in Abaqus (2014). A typical mesh is shown in Figure 5-16 with loading straps in green and the analytical rigid supports shown in blue. This torus had an in-plane radius R that differed from the average by more than ±25mm, whereas the out-of-plane deviation Z was relatively minor and virtually all deformation occurred in-plane. The in-plane radius R is shown in Figure 5-17 with values from fitting shown with symbols. As a check, the torus fitting routine was used to fit a torus to FE model nodes, which were confirmed to be consistent.
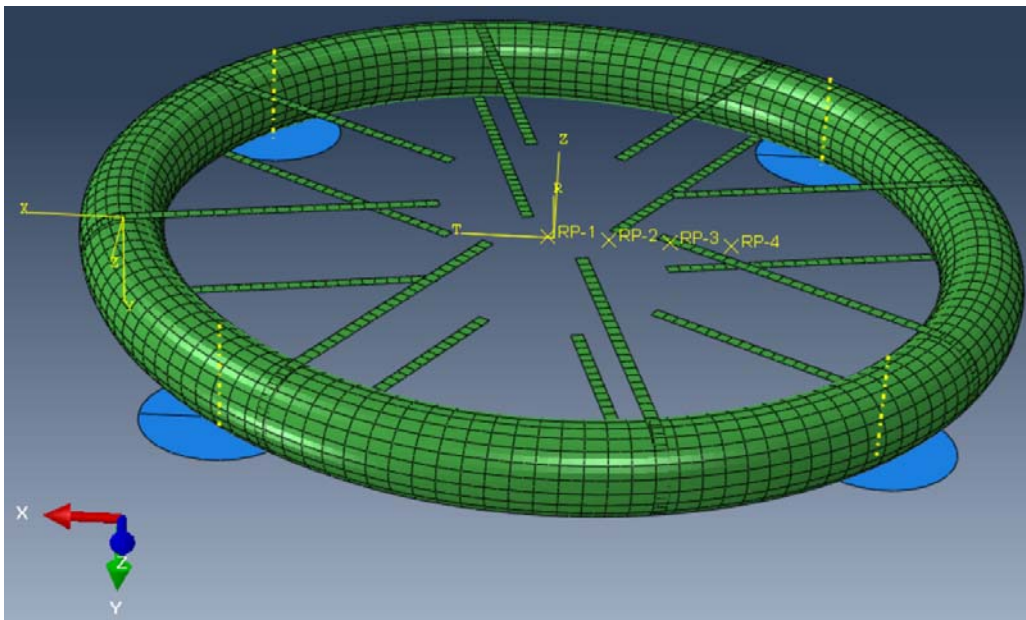
Figure 5-13. Finite element model with mesh (green) and rigid support (blue).

All meshing strategies were consistent with that described in Clapp et al. 2016b in terms of element types and element edge lengths. Element type S8R was used for the torus and straps. Element type B32 was used for the reinforcing cords. The seed size for meshing was 51 mm. It should be noted that both coarser meshing and more refined meshing were investigated and problems with solution convergence were noted in both cases. The support surfaces were modeled at actual size as analytical rigid surfaces. The real geometry of the torus was obtained by creating a 3D spline through the coordinates of the centerline of the torus cross-section and then using the sweep feature.
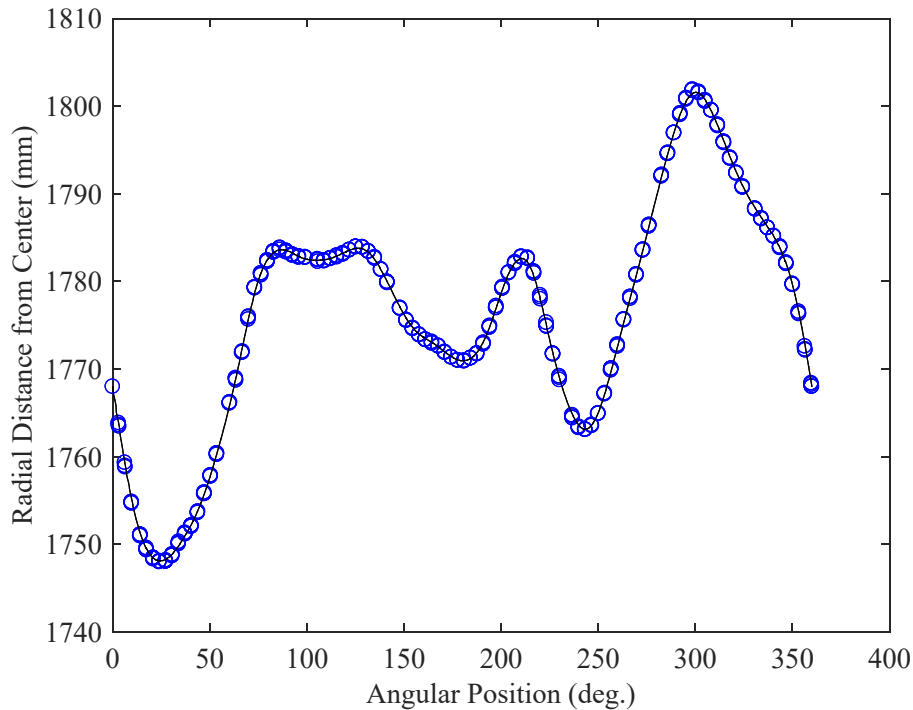
Figure 5-14. In-plane geometry of torus: measured (symbols) and FE mesh centerline (line).

Surface-to-surface contact was included between the torus and the four supports. Finite sliding with surface to surface discretization was utilized. The tangential behavior was defined with a penalty friction formulation with isotropic directionality. The friction coefficient was set

equal to two. Normal behavior was defined as "Hard" Contact. The Augmented Lagrange constraint enforcement method was used and separation was permitted. The default stiffness value was used with stiffness scale factor of 10. The straps and the torus were constrained to be tied together.

5.4.2   Analysis Steps

1. Apply pressure to the inside of the torus using follower forces. This causes load to be developed in the straps. Convergence was not able to be achieved without the straps restraining the torus.

2. Move all of the strap ends outward radially by a value that is constant for a given configuration, but varies by configuration, to get the strap forces back closer to the preload value of 45 N. The load in each strap is variable in the FE model when considering the real geometry.

3. Apply gravitational acceleration.

4. Repeatedly displace the strap ends inward incrementally by 1.27 mm per step and continue until the total displacement is similar to that applied in the experiment.

5.4.3   Results

Four models were created for purposes of examining the results. The most realistic model included the nonlinear cord load-strain behavior as well as the real geometry of the torus. The next two models were the same, except one used a linearly elastic relationship for the cords and the other used perfect torus geometry with major radius R equal to the average radius. The final

model used both a linearly elastic relationship for the cords and perfect torus geometry. It was found that the response predicted by all models were very similar, thus only the results of the most realistic model are presented.

The radial displacement of the torus varies among the nodes around the cross-section at a given point. Thus, the displacements were determined using the same fitting routines that were used in the experiments with the deformed mesh taken as measurement points. The experimental measurements are only collected on the top surface of the torus, but should give a reasonable approximation for the average cross-sectional displacement since it varies mainly from inside to outside.

The in-plane shapes and displacements are shown in Figure 5-18 and Figure 5-19 for the most realistic FE models vs. the experiment, respectively for both the initial conditions and at a total applied load of 16 kN. Several general conclusions were drawn:

1.   The initial load in the straps is not exactly equal to the applied preload of 45 N per strap. Since a converged solution could not be obtained with the model run in load control, a time-consuming iterative process would need to be incorporated to precisely determine the set of strap displacements that yields the correct forces in all 16 straps.

2.   The variability in load among the straps is significantly less than observed in experiments. This is primarily because the stiffness of the mechanical systems used to transfer load between the actuators and the torus were measured to be highly variable, whereas an equal stiffness is used for all straps in the model.

3. The effects of real versus perfect geometry as well as nonlinear cord stiffness versus linearly elastic cord stiffness did not appear to be particularly significant as hypothesized based on the response observed in the NASA 3D shell element models that showed a much lower predicted capacity with imperfect geometry compared to real geometry.

4. The initial shape of the torus must be smaller than the shape of the torus measured at a particular inflation pressure in order to end up at the correct shape after the inflation step in the model.

5. The FE model predicted a displaced shape with 8 outward deflecting points (between all loading points), whereas there were only 4 outward deflecting points observed in the experiment.
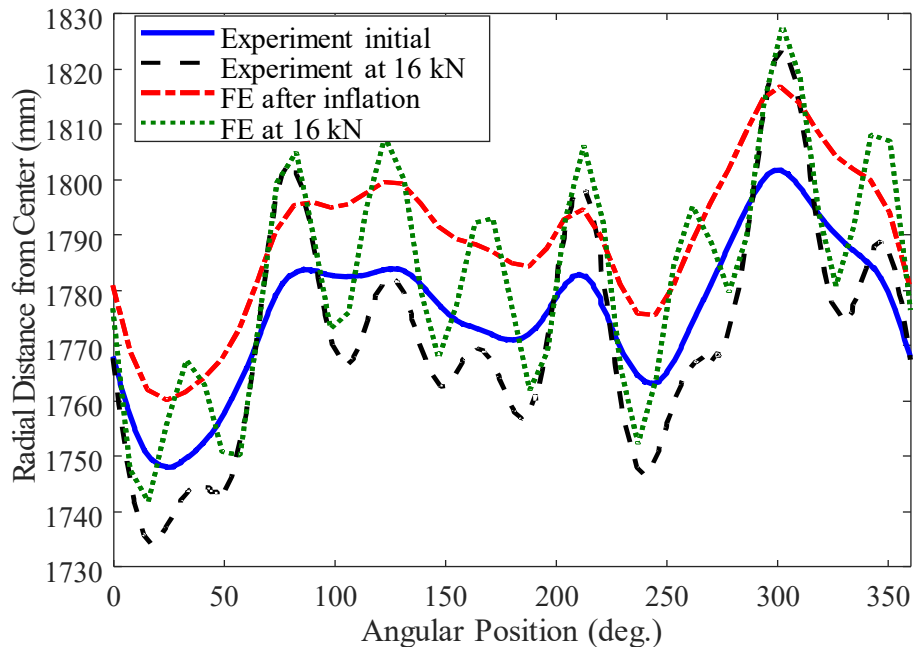
Figure 5-15. In-plane shapes of T4AP-1 at initial conditions and at 16 kN of total applied load for both experiment and FE model.
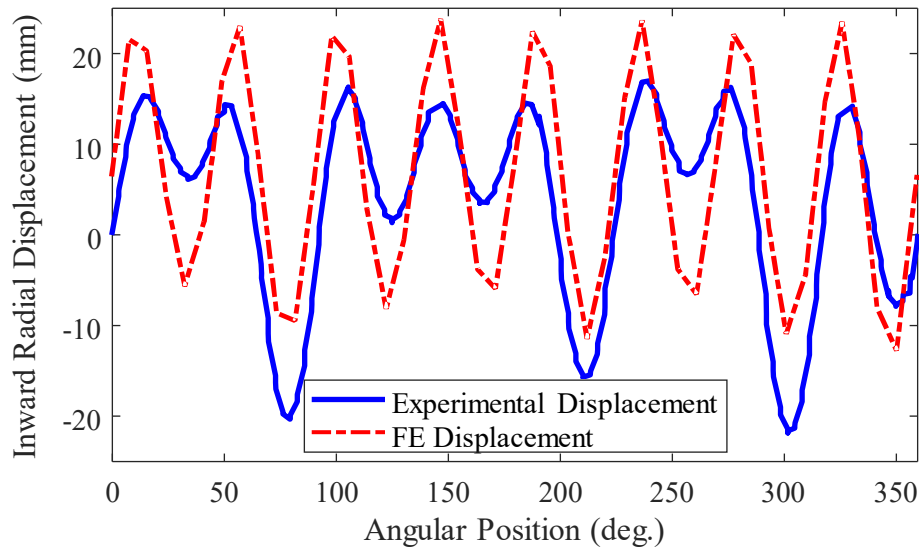
Figure 5-16. In-plane displacement of T4AP-1 from initial conditions to 16 kN of total applied load for both experiment and FE model.

5.5   Conclusions and next steps

Prior torus testing efforts by NASA Armstrong Flight Research Center were briefly described and lessons learned were described. The lessons learned help to form the initial objectives of this research:

1. Mechanical systems were improved by using better hardware with significantly less friction. This resulted in much lower variability among cables for a given group of four on a single whiffle tree.

2. Both load-control and displacement-control experiments were performed with notably different response observed. Ultimately the displacement-control experiments were elected to be used for FE model validation work described in Young et al. (2017a and 2017b).

3. Methods were developed for accurately quantifying the shape of the torus both before and during testing. Techniques were developed to reduce the file size of the images, reduce photogrammetry software processing time, and improve the quality of the data all by simply modifying the raw images. Robust and efficient code was developed to take raw 3D coordinates from the photogrammetry software and output accurate 3D geometry of the torus minor diameter centroid. These methods were used in the far more extensive experimental efforts described by Whitney (2016).

4. Developing 3D shell-element FE models of the torus test to examine the effect of real vs. nominal torus geometry proved to be a major challenge. The model seemed to be very sensitive to minor changes and would fail to achieve a converged solution. The model was not able to solve to loads as high as those applied in the experiments when the model was run in load-control. Ultimately some inconvenient and difficult to justify features had to be added to the model in order to get it to solve. The effect of including real geometry in the model did not appear to significantly affect the solution, however it has not been established that the model is correctly capturing all of the key physics.

Recommended next steps in terms of experimentation would be to expand the text matrix to examine additional torus configurations both in terms of major diameter as well as reinforcing schemes as described in Whitney (2016). Further, the experimental efforts should be expanded to include testing two tori paired together with straps as conceptually shown in Figure 5-20. This adds the complexities of torus-to-torus interaction and strap-to-torus interaction that exist in the full HIAD. This is the logical next step to capture the next level of complexity building towards

the full HIAD stack, but at the same time keeping costs relatively low, which may yield a more cost-effective way to validate FE models.
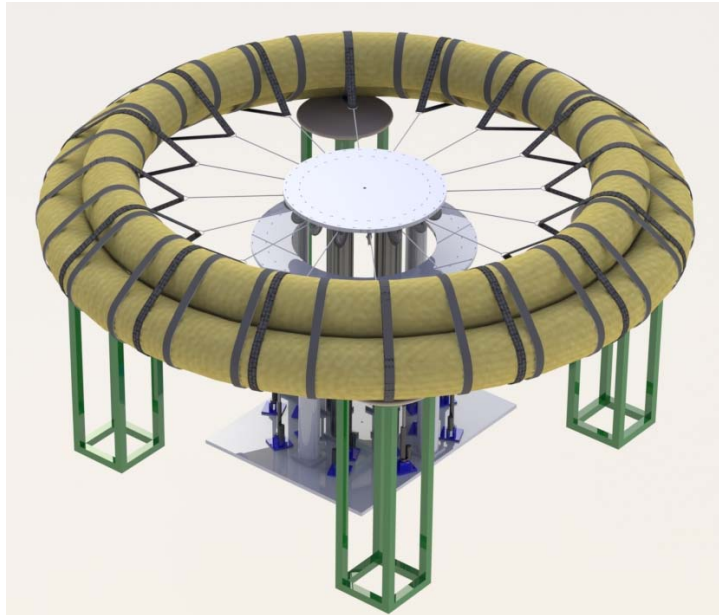
Figure 5-17. Conceptual rendering of proposed pair tori test.

Recommended next steps for modeling at the University of Maine are to abandon the higher fidelity 3D shell-element models and instead continue the approach started in Young et al. (2017a) and extended in Young et al. (2017b) and Young (2017) that uses 3D beam elements to more efficiently model the HIAD structure. These more efficient models are better suited to exploring the HIAD design space and learning more about how the design parameters affect the response of the system. The more efficient modeling strategy also lends itself to optimization studies that can be used to minimize the mass of the structure while meeting structural performance requirements.

The higher-fidelity 3D shell-element models developed by NASA can then be used to more closely examine predicted response for the configuration determined in the optimization study. Each modeling approach has its advantages and together they are complementary in nature.

6 SUMMARY, CONCLUSIONS, AND RECOMMENDATIONS

In this chapter, the research is summarized and conclusions are drawn. Recommendations for future research related to inflatable, reinforced, braided structural members are suggested.

6.1 Summary

The HIAD system being developed by NASA is an inflatable structure composed of multiple, concentric, pressurized tori, load straps, and a thermal protection system. The HIAD overcomes limitations inherent with the use of rigid decelerators since the deployed diameter is much larger than the packed size, which makes it an enabling technology for new opportunities in space exploration. The HIAD is designed to decelerate and protect spacecraft during atmospheric re-entry. The goal of this study was to improve understanding of structural behavior of HIAD components through material testing, structural testing of components, and analysis.

The mechanics of braided, inflatable cylinders were reviewed both in terms of the traditional stress transformation method (netting theory) as well as a geometric approach. The validity of the approximation used in estimating Poisson's ratio in Clapp et al. (2016b) was examined based on its effect on pressure-volume work.

Uni-axial tension tests were performed to quantify the load-strain relationship of the integral, tube reinforcing cords. Benchtop inflation tests were also performed to assess the stiffness of straight tubes relative to the stiffness of individual reinforcing cords. The load in the cords was estimated based on netting theory for the benchtop inflation tests. Methods for measuring cord strains other than digital image correlation were also investigated as part of the benchtop inflation testing.

Several experiments were performed in an effort to quantify the effective elastic stiffness properties of relatively large, and full-scale for a 6 meter HIAD, inflatable, braided tubes fabricated from Technora fiber tows and a urethane gas bladder. Tension and torsion experiments were successfully performed on full-scale, inflated, braided fabric tubes of four different braid angles and at five different levels of inflation pressure. Independent testing of the bladder material and extracted fiber tow bundles were also performed to more fully characterize the entire tube assembly.

A large matrix of experiments was successfully performed to characterize the bending behavior of straight, inflatable, braided tubes with integral reinforcing cords with highly controlled loading and boundary conditions. Several parameters were considered in the experiments: tube braid angle, tube cross-sectional orientation, level of internal inflation pressure, and the effect of cyclic loading.

Prior individual torus testing efforts by NASA Armstrong Flight Research Center were reviewed and lessons learned were described, which helped to form the initial objectives of the individual torus testing efforts at the University of Maine. Mechanical systems were improved by using better hardware with significantly less friction. This resulted in much lower variability among cables for a given group of four load cells attached to a single whiffle tree.

Both load-control and displacement-control experiments were performed. Methods were developed for accurately quantifying the shape of the torus both before and during testing. Techniques were developed to reduce the file size of the images, reduce photogrammetry software processing time, and improve the quality of the data by modifying the raw images.

Robust and efficient code was developed to take raw 3D coordinates from the photogrammetry software and determine accurate 3D geometry of the torus minor diameter centroid.

Exploratory finite-element models using 3D shell-elements were developed to assess the use of 3D shell-based FE analysis for simulating torus response. These modeling efforts proved to be challenging and further justified the alternate modeling approach taken by Young et al. (2017a and 2017b), which uses 3D beam-elements instead of shell-elements.

6.2 Conclusions

It was shown that there is geometric stiffening for braided tubes due to pressure-volume work if the inflation pressure is constant. It was also shown that it is reasonable to use an approximate value for Poisson's ratio with an orthotropic elasticity model to accurately capture the pressure-volume work that occurs due to the braid acting as a mechanism. A simple finite-element model using this approximate value of Poisson's ratio was shown to be in good agreement with the predicted geometric stiffening term using exact solutions for a fiber that is infinitely stiff in the fiber direction, but otherwise free to rotate. Numerical models must capture this geometric stiffening effect either directly (Clapp et al. 2016b) or indirectly (Young et al. 2016a; Young et al. 2016b).

The response of independently tested reinforcing cords on the first cycle of loading is highly variable because the previous state of the cords is unknown and not controlled. However, after a complete load-unload cycle, the behavior is very similar for all cords tested including both pristine independent cords as well as cords extracted from straight tubes after the bending tests were performed as described in Chapter 4. Cord load-strain response is generally nonlinear, and

the load-strain data gathered from these cord tests is vitally important for predicting the load-deformation and load-strain response of inflated, braided tubular structural members. The response of the cords is highly nonlinear at low levels of load and becomes more linear at higher loads, therefore it is critical to accurately capture the nonlinear cord response if the inflation pressure is relatively low or if the cord pretension will be significantly reduced due to axial loading or bending deformations.

It was found in benchtop inflation testing that the axial stiffness per cord of the straight tubes is very similar to the stiffness of independently tested cords, which confirms that the cord stiffness dominates the overall response. Relatively long foil strain gages were found to work very well for accurately capturing the average strain in the cords. It was confirmed via comparison with DIC strain data that foil strain gages with a 51 mm gage length accurately captured the average strain in the cords. Based on the benchtop testing documented here, NASA has adopted foil strain gages as their method for measuring cord strains in their large-scale full HIAD tests (Swanson et al. 2015) where it is impossible or impractical to use DIC systems.

The state-of-the-art in testing inflatable, braided tubes was significantly advanced through testing of full-scale braided tubes with several different braid angles. Non-contact DIC methods were used extensively to collect measurements that were not recorded in prior studies. All information required to consider netting theory was directly measured throughout testing. The braided tube fabric shear stiffness was found to be highly dependent on both braid angle and inflation pressure. The shear stiffness was found to increase as the braid angle becomes closer to the optimal value of 45 degrees as expected. The shear stiffness was also found to increase with increasing inflation pressure due to inter-tow friction and fiber tow de-crimping. Independent

testing of extracted straight fiber tows revealed that the ratio of the back-calculated fiber tow stiffness to straight tow stiffness increases with inflation pressure and appears to be converging towards a value of 1. The fabric longitudinal stiffness was found to be quite small relative to the shear stiffness, and it was not possible to clearly discern the effects of braid angle on longitudinal stiffness due to the small values of stiffness. Independent testing of the urethane gas bladder material revealed that it provides a large portion of the longitudinal stiffness of the inflated, braided tubes, but contributes very little to shear stiffness.

The DIC data revealed spatial variation of shear strain, which would have been very difficult to measure with traditional strain gages. Consideration of this spatial variation led to the conclusion that using an average surface shear strain would lead to an incorrect calculation of gross engineering shear stiffness. This illustrated the importance of using appropriate methods for calculating the gross engineering shear stiffness as done in this study instead of relying on the average surface shear strain. DIC data also captured the braid surface flattening with increasing inflation pressure, which quantitatively supports the fiber de-crimping theory.

The effective modulus of the fiber tows in the inflatable tubes was seen to increase with pressure, which is attributed to increasing de-crimping and inter-tow friction with increasing inflation pressure. Independent testing of individual fiber tows extracted from uncoated braid material was also performed. The straight tow modulus observed from these tests agreed well with the published stiffness of Technora, and was an upper bound on the effective tow modulus back-calculated from the tension-torsion tests.

The straight beam bending test data provide a solid set of baseline configurations with highly controlled loading and boundary conditions to validate FE models. The predictions in the models developed by Young (Clapp et al. 2016b; Young et al. 2017a) agree quite well with the

experimental data, particularly for the tubes with larger braid angles that of the highest interest for structural applications. The DIC systems also captured secondary data such as out-of-plane deflections driven by lateral buckling. This proved to be valuable data for the validation of geometrically nonlinear 3D FE models (Clapp et al. 2016b).

The single torus structural load tests revealed that while the structural capacity of the tori was dependent on inflation pressure, capacity increased at a rate that was less than proportional to the increase in pressure. The response of the torus in tests run in load-control versus displacement-control were found to be different with more outward movement observed in load-controlled testing. The shape of the torus in load-controlled testing was also observed to be triangle-like, whereas in displacement controlled testing the shape was square-like. Ultimately the displacement-control experiments were chosen for the FE model validation studies described in Young et al. (2017b).

The methods developed to determine the 3D shape and displacements of the torus test articles based on arbitrarily placed photogrammetry markers were found to work well and give accurate shape determination. These methods were extensively used in the testing of many additional torus articles, including those with alternate reinforcing strategies as described by Whitney (2016). These shape-determination methods also provided essential information for the beam-based torus modeling conducted by Young (2017) and Young et al. (2017b).

The 3D shell-element FE models of the torus test designed to examine the effect of real vs. nominal torus geometry proved challenging. The model was very sensitive to seemingly minor changes that would cause it to fail to converge. The model was not able to solve for loads as high as those applied in the experiments when the model was run in load-control. Ultimately

some inconvenient and difficult-to-justify features were incorporated in the model in order to achieve a solution. The model was not able to be validated based on comparisons to experiments, and the objective of examining the effect of including real geometry in the model was not achieved.

6.3. Recommendations for Future Work

Efforts to quantify the constitutive behavior of new elements (i.e. different braid angle or material) that make up a HIAD structure should be performed early in the experimental program so that these key finite-element model inputs can be established before models are developed.

Suggested future studies related to tension-torsion testing could include performing testing with alternate braid geometries (particularly braid angles greater than 71°) and materials. Additional testing with combined tension and torsion loading similar to the methods used by Turner et al. (2008) could also be performed to examine fabric response under combined loading. Additional data may shed more light on the feasibility of establishing methods of estimating the stiffness of inflatable braided structures given braid angle, straight fiber tow stiffness, and inflation pressure. Additional validation of finite-element models that rely on the methods described for determining effective elastic properties, but for alternate materials/geometries, would further increase confidence that the methods are reasonable.

Recommended next steps in terms of torus experimentation are to expand the text matrix to examine additional torus configurations both in terms of major and minor diameter as well as alternate reinforcing schemes such as described in Whitney (2016). Further, the experimental efforts should be expanded to include testing two tori paired together with straps as conceptually shown in Figure 5-20. This is the logical next step to capture increasing complexity building

towards the full HIAD stack, but at the same time keeping costs relatively low, which may economically yield additional data for FE model validation.

Many additional experiments were performed on single tori test articles beyond those described in this dissertation (Whitney 2016 and Young et al. 2017b). These data sets can potentially be useful to other researchers who may wish to take a closer look at certain aspects of torus structural response such as hysteresis.

Recommended next steps for modeling at the University of Maine are to discontinue use of higher fidelity 3D shell-element models and advance the approach developed by Young et al. (2017a) and extended in Young et al. (2017b) and Young (2017) that relies on beam elements to model the HIAD structure. These more computationally efficient models are better suited to exploring the HIAD design space and investigating how the design parameters affect the response of the system. The more efficient modeling strategy also lends itself to optimization studies that can be used to minimize the mass of the structure while meeting structural performance requirements, and complement the higher-fidelity shell-element models developed by NASA.

REFERENCES

Abaqus, Abaqus Standard, User's Manual, ver. 6.11, Dassault Systems Inc., Paris, France, 2014.

Abraham, N., Buehrle, R. Templeton, J., Lindell, M., & Hancock, S. (2014) Modal Test of Six-Meter Hypersonic Inflatable Aerodynamic Decelerator. *Proc of the Society for Experimental Mechanics Series Conference* 2014, 401-413.

Apedo, K.L., Ronel, S., Jacquelin, E., Bennani, A., and Massenzio, M. (2010). "Nonlinear finite element analysis of inflatable beams made from orthotropic woven fabric." *International Journal of Solids and Structures*, 47(16), 2017-2033.

ARAMIS software (2011) GOM Optimal measuring techniques, http://www.gom.com

Avitabile, P., Niezrecki, C., Helfrick, M., Warren, C. and Pingle, P., 2010. Noncontact measurement. Techniques for model correlation. *Sound and Vibration*, *44*(1), p.8.

Barsotti, R., & Ligarò, S.S. (2014). "Numerical analysis of partly wrinkled cylindrical inflated beams under bending and shear." *Thin-Walled Structures*, 84, 204-213.

Braun, R.D. and Manning, R.M. (2007) Mars exploration entry, descent and landing challenges. *Journal of Spacecraft and Rockets*. 44, 310-323.

Brayley, K., Davids, W.G., and Clapp, J.D. (2012) "Bending response of externally reinforced, inflated, braided fabric arches and beams." *Construction and Building Materials* 30, 50-58.

Brown, G., Haggard, R., and Norton, B. (2001) "Inflatable Structures for Deployable Wings." In: *AIAA conference paper, AIAA-2001-2068*.

Cassell, A.M., Swanson, G.T., Quach,, W., Kushner, L.K., Brown, J.D., Kazemba, C.D., Kruger, C., Johnson, R.K., Hughes, S.J., Littell, J., Calomino, A.M., and Cheatwood, F.M. (2013). "Design and execution of the hypersonic inflatable aerodynamic decelerator large-article wind tunnel experiment." *Proc AIAA Aerodynamic Decelerator Systems Technology Conference* XXII.

Cavallaro P.V, Johnson M.E, and Sadegh A.M., "Mechanics of Plain-Woven Fabrics for Inflated Structures," *Composite Structures*, 6, No. 4, 2003, pp. 375-393.

Chen, T. and Moholt, M., (2014) HIAD Torus Mechanical Testing Test Report. 08/23/2014, NASA Armstrong Flight Research Center, Edwards, California.

Clapp, J.D., Young, A.C., Davids, W.G., and Goupee, A.J., (2015) "Structural Response of Hypersonic Inflatable Aerodynamic Decelerator Braided Tube Components and Elements." In: *AIAA Aerodynamic Decelerator Systems Technology Conference* XXIII.

Clapp, J.D., Davids, W.G., Goupee, A.J. and Young, A.C. (2016a). "Experimental Determination of Inflatable, Braided Tube Constitutive Properties." *Strain*, 52, 148-161.

Clapp, J. D., Young, A. C., Davids, W. G., and Goupee, A. J. (2016b). "Bending response of reinforced, inflated, tubular braided fabric structural members." *Thin-Walled* Structures, 107, 415-426.

Clark, I.G., Cruz, J.R., Hughes, M.F., Ware, J.S., Madlangbayan, A. and Braun, R.D. (2009). Aerodynamic and aeroelastic characteristics of a tension cone inflatable aerodynamic decelerator. *Proc AIAA Aerodynamic Decelerator Systems Technology Conference* XX.

Colman, A.G., Bridgens, B.N., Gosling, P.D., Jou, G.T., & Hsu, X.Y. (2014) "Shear behaviour of architectural fabrics subjected to biaxial tensile loads." *Composites Part A: Applied Science and Manufacturing 66*, 163-174.

Davids, W.G., Zhang, H., Turner, A.W., & Peterson, M. (2007). "Beam finite-element analysis of pressurized fabric tubes." *Journal of Structural Engineering*, 133(7), 990-998.

Davids, W.G., & Zhang, H. (2008). "Beam finite element for nonlinear analysis of pressurized fabric beam–columns." *Engineering Structures*, 30(7), 1969-1980.

Davids, W.G. (2009). "In-plane load-deflection behavior and buckling of pressurized fabric arches." *Journal of structural engineering*, 135(11), 1320-1329.

D. B. Miracle, S. L. Donaldson (2001) *ASM Handbook Vol. 21: Compos*. ASM International, 2001.

Dorf, R. C., and Bishop, R. H. (1998). Modern control systems.

Elsabbagh, A. (2015). "Nonlinear finite element model for the analysis of axisymmetric inflatable beams." *Thin-Walled Structures*, 96, 307-313.

Evans, J.T., & Gibson, A.G. (2002) "Composite angle ply laminates and netting analysis." In *Proceedings of the Royal Society of London A: Mathematical, Physical and Engineering Sciences*, 458 (2028), 3079-3088.

Ghosh, S. Lee, K., Moorthy S. (1996). "Two scale analysis of heterogeneous elastic–plastic materials with asymptotic homogenization and Voronoi cell finite element model." *Comput Method Appl Mech Eng*, 132, 63-116.

González, C. Segurado, J., Llorca, J. (2004). "Numerical simulation of elasto-plastic deformation of composites: evolution of stress microfields and implications for homogenization models" J Mech Phys Solids, 52, 1573-1593.

Guo, X., Li, Q., Zhang, D., & Gong, J. (2016). "Structural Behavior of an Air-Inflated Fabric Arch Frame." *Journal of Structural Engineering*, 04015108.

Hughes, S.J., Dillman, R.A., Starr, B.R., Stephan, R.A., Lindell, M.C., Player, C.J. and Cheatwood, F.M. (2005). Inflatable re-entry vehicle experiment (IRVE) design overview. *Proc AIAA Aerodynamic Decelerator Systems Technology Conference* XVIII.

Hutchings, A.L., Braun, R.D. (2009) *Experimental Determination of Material Properties for Inflatable Aeroshell Structures*. In: *AIAA Aerodynamic Decelerator Systems Technology Conference* XX.

Jurewicz, D., Brown, G., Gilles, B., Lichodziejewski, L., Kelly, C., Tutt, B., & Hughes, S. (2011, May 23-26). Design and Development of Inflatable Aeroshell Structure for IRVE-3. *Proc AIAA Aerodynamic Decelerator Systems Technology Conference* XXI.

Kabche, J.P., Peterson, M.L. and Davids, W.G. (2011) "Effect of Inflation Pressure on the Constitutive Response of Coated Woven Fabrics Used in Airbeams." *Composites Part B: Engineering*. 42, 526-537.

Kahn-Jetter, Z. L., and Chu, T. C., 'Three-Dimensional Displacement Measurements Using Digital Image Correlation and Photogrammic Analysis, Experimental Mechanics, Vol. 30, No. 1, pp. 10-16, 1990.

Kazemba, C.D., Cassell, A.M., Kushner, L.K., Tran, K., Quach, B.T., Li, L., Van Norman, J.W., Littell, J.D., Johnson, R.K., Hughes, S.J., Calomino, A.M., and Cheatwood, F.M. (2013) "Determination of the Deformed Structural Shape of HIADs from Photogrammetric Wind Tunnel Data." In: *AIAA Aerodynamic Decelerator Systems Technology Conference* XXII.

Leonard, R.W., Brooks, G.W., and McComb, H.G. (1960). "Structural considerations of inflatable reentry vehicles." NASA Tech. Note D-457, Langley Research Center, Langley Field, VA.

Li L., Braun R.D. and Cassell A.M. (2014) "Photogrammetry Analysis of a Hypersonic Inflatable Aerodynamic Decelerator Structural Test Article." In: *AIAA Aerodynamic Decelerator Systems Technology Conference* XXII.

Litton, D.K., Bose, D.M., Cheatwood, F.M., Hughes, S., Wright, H.S., Lindell, M.C. and Derry, S.D. (2011) *Inflatable re-entry vehicle experiment (IRVE) – 4 Overview*. NASA Technical Report NF1676L-11478, June 6.

Luchsinger, R.H., Sydow, A., & Crettol, R. (2011). "Structural behavior of asymmetric spindle-shaped Tensairity girders under bending loads." *Thin-walled structures*, 49(9), 1045-1053.

Luchsinger, R.H., & Galliot, C. (2013). „Structural behavior of symmetric spindle-shaped tensairity girders." *Journal of Structural Engineering*, 139(2), 169-179.

Luo, P. F., Chao, Y. J., Sutton M. A., and Peters, W. H., Accurate Measurement of Three-Dimensional Deformations in Deformable and Rigid Bodies Using Computer Vision, Experimental Mechanics, Vol. 33, No. 2, June 1993.

Lyle, K.H. (2015) "Comparison of Analysis with Test for Static Loading of Two Hypersonic Inflatable Aerodynamic Decelerator Concepts." NASA Technical Memorandum TM-2015-218778, July 2015.

Main, J.A., Peterson, S.W., & Strauss, A.M. (1994). "Load-deflection behavior of space-based inflatable fabric beams." *Journal of Aerospace Engineering*, 7(2), 225-238.

Main, J.A., Peterson, S.W., & Strauss, A.M. (1995). "Beam-type bending of space-based inflated membrane structures." *Journal of Aerospace Engineering*, 8(2), 120-125.

Malm, C.G., Davids,W.G., Peterson, M.L., & Turner, A.W. (2009). "Experimental characterization and finite element analysis of inflated fabric beams." *Construction and Building Materials*, 23(5), 2027-2034.

MathWorks (2012) Using MATLAB v. 2012b, MathWorks, Inc., Natick, MA.

Mikhail, E., Bethel, J., and McGlone, J., Introduction to Modern Photogrammetry, John Wiley and Sons, 2001.

Nguyen, Q.T., Thomas, J.C., and Le van, A. (2015). "Inflation and bending of an orthotropic inflatable beam." *Thin-Walled Structures*, 88, 129-144.

O'Keefe, S.A. and Bose, D.M. (2010) *IRVE-II post-flight trajectory reconstruction.* NASA Technical Report NF1676L-10183, September 2.

PONTOS Software, GOM Optimal Measuring Techniques, ⟨http://www.gom. com⟩, 2011.

Steeves, E.C. (1975) "A linear analysis of the deformation of pressure stabilized beams." AD/A-006 493, Army Natick Laboratories, Natick, MA.

Steeves, E.C. (1978) "Pressure stabilized beam finite element." TR-79/002, *Aero-Mechanical Engineering Laboratory,* Natick, MA.

Sutton, M. A., Orteu, J. J., Schreier, H., Image Correlation for Shape, Motion and Deformation Measurements: Basic Concepts, Theory and Applications, Springer Science+Business Media, LLC, ISBN#: 978-0-387-78746-6, 2009.

Swanson G.T., Cassell A.M., Johnson K., Hughes S.J., Calamino A. and Cheatwood M. (2013) "Structural strap tension measurements of a 6 meter hypersonic inflatable aerodynamic decelerator under static and dynamic loading." In: *AIAA Aerodynamic Decelerator Systems Technology Conference* XXII.

Swanson, G. T., Kazemba, C.D., Johnson, R. K., Hughes, S.J., Calomino, A.C., Cheatwood, F.M., and Cassell, A.M. (2014) "Overview of the 6 Meter HIAD Inflatable Structure and Flexible TPS Static Load Test Series." In: *11th International Planetary Probe Workshop*.

Swanson G., Kazemba C., Johnson R., Hughes S. and Calomino A. (2015) "Structural Testing of a 6m Hypersonic Inflatable Aerodynamic Decelerator System." *Proc. 2015 IEEE Aerospace Conference.*

Teijin (2016). Retrieved 03/15/2016: http://www.teijinaramid.com/aramids/technora/

Terada, K. Horib, M., Kyoyac, T. Kikuchid, N. (2000). "Simulation of the multi-scale convergence in computational homogenization approaches." *Int J Solids Struct*, 37, 2285-2311.

Thomas, J.C. and Le van, A. (2013). "An exact solution for inflated orthotropic membrane tubes." *Thin-Walled Structures*, 67, 116-120.

Thomas, J.C., & Wielgosz, C. (2004). "Deflections of highly inflated fabric tubes." *Thin-Walled Structures*, 42(7), 1049-1066.

Turner, A. W., Kabche, J. P., Peterson, M. L., & Davids, W. G. (2008). "Tension/torsion testing of inflatable fabric tubes." *Experimental Techniques*. 32(2), 47-52.

Veldman, S.L., Bergsma, O.K., Beukers, A. and Drechsler, K. (2005a) "Bending and optimization of an inflated braided beam." *Thin-walled Structures*. 43, 1338-1354.

Veldman, S.L. (2005b). "Design and Analysis Methodologies for Inflated Beams." PhD Dissertation, Delft University of Technology, retrieved: http://repository.tudelft.nl/assets/uuid:3e141764-5f47-419d-91cc-2493556e6ba5/ae_veldman_20050617.pdf

Veldman, S.L. (2006). "Wrinkling prediction of cylindrical and conical inflated cantilever beams under torsion and bending." *Thin-walled structures*, 44(2), 211-215.

Webber J.P.H. (1982) "Deflections of inflated cylindrical cantilever beams subjected to bending and torsion." Aeronaut J 1020, 306–12.

Weeks, G. E. (1967). *Buckling of a pressurized toroidal ring under uniform external loading.* National Aeronautics and Space Administration.

Whitney, D. J. (2016) "Experimental methods and practices for the study of toroidal inflated, braided fabric members (Unpublished master's thesis)." University of Maine, Orono, Maine.

Wicker, W.J. (1993) "The structural characteristics of inflatable beams." *Acta Astronautica* 30, 443-454.

Wielgosz, C., & Thomas, J.C. (2002). "Deflections of inflatable fabric panels at high pressure." *Thin-walled structures,* 40(6), 523-536.

Wright, H., Cutright, A., Corliss, J., Bruce, W., Trombetta, D., Mazaheri, A.R., Coleman, M., Olds, A. and Hancock, S. (2012, June 16-22). HEART flight test overview. *Proc International Planetary Probe Worksho*p IX.

Young. A.C., Davids, W.G., Goupee, A.J., Clapp, J.D. (2017a), Computationally efficient finite-element modeling of braided, inflatable structural members with axial reinforcing, *Journal of Engineering Mechanics* 143(6).

Young. A.C., Davids, W.G., Whitney, D.J., Clapp, J.D., and Goupee A.J. (2017b), Structural testing and analysis of a braided, inflatable fabric torus structure, Acta Astronautica, (in review).

Young, A.C. (2017) "Large Payload HIAD Systems: Development of Computationally Efficient Modeling Strategies and Structural Investigations (unpublished doctoral dissertation)" University of Maine, Orono, Maine.

Zhu, Z.H., Seth, R.K., & Quine, B.M. (2008). "Experimental investigation of inflatable cylindrical cantilevered beams." *JP Journal of Solids and Structures*, 2(2), 95-110.

BIOGRAPHY OF THE AUTHOR

Joshua Clapp was born in Bangor, Maine on December 24, 1982 to Eric and Dawna Clapp. He was raised in Eddington, Maine and graduated from John Bapst Memorial High School, Bangor, Maine, in 2001. He attended the University of Maine and graduated summa cum laude in 2005 with a Bachelor of Science degree in Civil and Environmental Engineering. He completed his Master of Science degree in Civil and Environmental Engineering, with a focus on structural engineering, in May, 2007.

Joshua likes to spend time with his wife, Meaghan, son, Tucker, and other family at camp on Bottle Lake or otherwise outdoors in the state of Maine.

Joshua enjoys having the opportunity to work with so many talented graduate students, undergraduate students, and high school interns at the University of Maine that will form the next generation of engineers.

After receiving his degree, Joshua will continue working as a research engineer/project manager at the Advanced Structures and Composites Center at the University of Maine. He is a candidate for the Doctor of Philosophy degree in Civil Engineering from the University of Maine in August, 2017.